Technische Universität München

Fakultät für Chemie

NMR Studies to Characterize Amyloid Inhibitors and Aβ-PET Tracer Complexes

Zheng Niu

Vollständiger Abdruck der von der Fakultät für Chemie der Technischen Universität München zur Erlangung des akademischen Grades eines Doktors der Naturwissenschaften (Dr. rer. nat.) genehmigten Dissertation.

Vorsitzender:

Prof. Dr. Steffen J. Glaser

Prüfer der Dissertation:

1. Prof. Dr. Bernd Reif

2. Prof. Dr. Aphrodite Kapurniotu

Die Dissertation wurde am 26.11.2018 bei der Technischen Universität München eingereicht und durch die Fakultät für Chemie am 22.01.2019 angenommen.

Acknowledgement

Table of Contents

Abstract

The amyloid-β peptide (Aβ) contains 36-43 amino acids and is involved in Alzheimer's disease (AD). One of the pathological hallmarks of AD is the deposition of amyloid plaques, which are composed of Aβ fibrils. The development of amyloid imaging markers and inhibitors has considerable significance since the early intervention and effective treatment are important to slow down or prevent the disease progression. Nuclear magnetic resonance (NMR) is one of the most powerful tools for the characterization of protein structure and protein-ligand interactions. In combination with biophysical and biochemical techniques, the structural characterization of the interaction surface mimics (ISMs) peptide inhibitors was achieved, and the bio-macromolecular complexes formed from positron emission tomography (PET) tracer molecules and Aβ fibrils were investigated as well.

Cross-amyloid ISMs are potent inhibitors for Aβ amyloidogenesis and cytotoxicity. In this dissertation, the structural preferences for the disordered peptide inhibitors were characterized by using solution-state NMR and ensemble averaged dynamics simulations. ISM inhibitor R3-GI undergoes chemical exchange between a monomeric state and an aggregated state. The monomeric state R3-GI contains with the random-coil like conformation and yields high-resolution solution-state NMR spectrum. In contrast, the oligomeric state R3-GI is too large to be detected from solution-state NMR. Apart from NMR, high molecular weight oligomers with liquid droplet-like structures were observed in differential interference contrast microscopy. Based on the observation from the dynamic simulation, there is an equilibrium between two populations in the major conformer of Gly17^{trans}/Ile19^{trans} R3-GI. The first population is lack of the secondary structure, whereas the second population is characterized by a β-like structure from residue Asn7 to residue Ser21. Although there is no indication of β structure in the minor conformer of Gly17^{cis}/Ile19^{trans} R3-GI, the structure is more compact in comparison to the major conformer. Furthermore, the monomer-monomer interface of R3-GI peptide inhibitor is well defined and characterized by several inter-molecular interactions and solvent-exposed side chains of arginine.

PET tracer molecules are imaging markers developed for AD diagnosis. The research described in this dissertation was designed to find out the structural information of Aβ-PET tracer complexes at the atomic level by using magic angle spinning solid-state NMR. In particular, the bithiazole-like organic small molecule and the standard amyloid PET tracer Pittsburgh compound B were

investigated. Considering the hydrophobic nature of the PET tracer molecules, bovine serum albumin was employed as a carrier to transfer the small molecule to $A\beta_{40}$ fibrils. The C–C and N–C correlation spectra of $A\beta_{40}$ fibrils in the absence and presence of PET tracer molecules are quite overlaid, indicating that PET tracer molecules don't induce drastic structural changes of $A\beta_{40}$ fibrils. Clear chemical shift perturbations (CSPs) were observed in the presence of PET tracer molecules, including the flexible loop region and the rigid hydrophobic C-terminal region. However, a polar cavity formed by the residues in the loop region is very unlikely to present a location for a hydrophobic small molecule. The CSPs of the loop region could be induced by the structural conformational rearrangement due to the direct binding interactions of the PET tracer molecules. In contrast, the hydrophobic cavities formed in the rigid core region are able to bury a small molecule. With the defined CSPs in the hydrophobic core, the groove structure at residue Gly33 and the hydrophobic region at residues Gly37-Gly38 could be suitable locations for the Aβ-PET tracer binding interactions.

Key words: Alzheimer's disease, amyloid-β fibrils, cross-amyloid interaction surface mimics, PET imaging tracer, solid-state NMR

Structure of the Dissertation

This dissertation is written in a monographic format. Utilizing nuclear magnetic resonance (NMR) to characterize the structure of peptide mimic inhibitor and protein-ligand interactions are the main parts of this dissertation. The project of NMR structural characterization of the peptide mimic inhibitor discussed in this dissertation has been ready for submission to the peer-reviewed journal. While the other project on the study of the interactions between amyloid-β (Aβ) fibrils and positron emission tomography tracer molecules has not yet reached the point for publication. The overall analysis of this research is ongoing, and the manuscript is going to be finalized.

The first Chapter describes the background of my doctoral research projects. From a brief introduction of Alzheimer's disease diagnosis and treatment, to the solid-state NMR structural characterization of protein/peptide at the atomic level. In the background of Alzheimer's disease subsection, the generation and aggregation of Aβ, amyloid imaging markers and the potent inhibitors are included and discussed. In solid-state NMR subsection, the reported solid-state NMR structure of Aβ fibrillar aggregates with atomic resolution are listed and compared. The recent research result on the cryo-EM structure of $A\beta_{42}$ fibrils is discussed as well. In Chapter 2, all the methods and materials applied in my doctoral research are described in detail.

The result and discussion of the two projects are presented in Chapter 3 and Chapter 4, respectively. In Chapter 3, the structure of cross-amyloid interaction surface mimic inhibitor R3-GI peptide is characterized by solution-state NMR and dynamic simulation. The aim of this research topic follows as a connecting link between a short introduction and experimental results. In Chapter 4, the topic of Aβ-PET tracer complexes interactions begins by the aim of this project, follows by the results and discussions. Each chapter ends with an overall discussion and a brief summary, in which the ongoing work is also presented.

Appendix section includes the list of abbreviation, lists of NMR chemical shifts assignment and references.

Chapter 1

Introduction

1. Introduction

1.1 Alzheimer's Disease

Alzheimer's disease (AD), as a neurodegenerative brain disease, has affected 44 million people all around the world.[1] The common symptoms of AD include the memory loss, language abilities decline, orientation and cognitive skills destruction. Moreover, these symptoms of AD would be getting much worse over time. Based on the symptoms and the progression of the disease, AD is generally divided into three stages, mild, moderate and severe AD.

Neurofibrillary tangles (NFT) and neuritic plaques (NP) are the major pathological hallmarks involved in AD.[2–7] Neurofibrillary tangles are insoluble abnormal fibers inside the brain nerve cells, which caused by the association of microtubule-associated protein tau. Neuritic plaques are amyloid deposits in the spaces between neurons and formed by amyloid-β peptide (Aβ) aggregation. In addition, the loss of neurons and synapses is also diagnosed in AD patient brain due to the low level of neurotransmitter acetylcholine (Ach).[8] Ach mainly distributes in the central nervous system, and is related to memory, recognition, learning and movement.
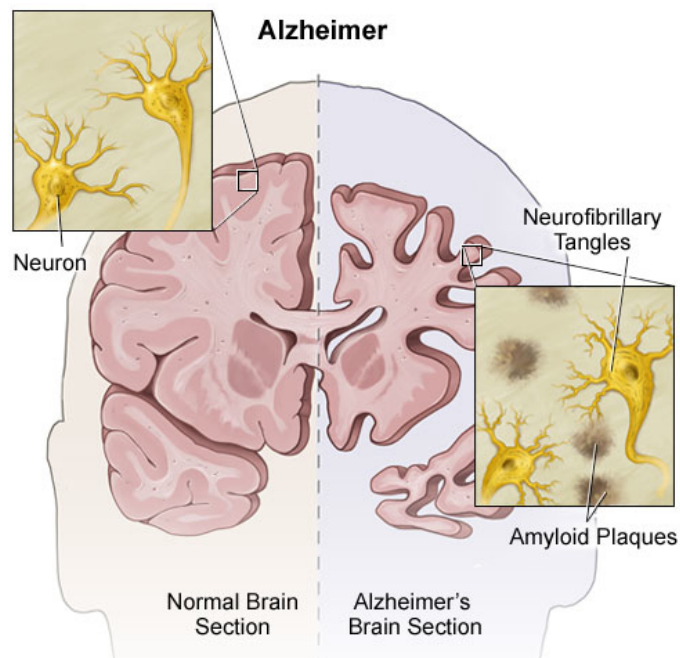
Figure 1: A comparison of AD patient brain with the normal brain.[9]

Based on the pathological features, several theories have been proposed to explain the pathological causes of AD, including genetics,[10,11] cholinergic hypothesis,[12] amyloid cascade hypothesis[13,14] and tau hypothesis.[14] However, a generally accepted hypothesis has not been settled on. Cholinergic hypothesis proposes the neurochemical changes in AD patients. Because of the reduced synthesis of Ach, tau shifts to the hyperphosphoryalted state, which is the precursor of neurofibrillary tangles. In addition, it also has influences on the secretion of soluble amyloid precursor protein (APP) leading to the increased production of Aβ. It is worth noting that additional factors, such as a loss of perikarya and synapses, are also involved in the cognitive impairment of AD in spite of dysfunction of cholinergic.[12] Unfortunately, drugs for increasing the level of Ach did not achieve great success in AD treatment, which is the main reason that this hypothesis is not supported by most scientists. Amyloid cascade hypothesis provides biochemical understanding of the pathological process, which speculates that the deposition of Aβ resulting in tau hyperphosphorylation, axonal disruption, synapse loss and ultimately neurons death. The deposition of amyloid plaques does not relate to neuron loss. In contrast, the tangles accumulate and extend in the neuron result in neuronal death supports the tau hypothesis.

Lacking early diagnosis and proper treatment are significant barriers to improving lives of AD patients. Medical treatments and early intervention are only available for those that have received a diagnosis. Additionally, the timely detection and definitive classification for the stage of AD are big challenges in the living subjects since the pathological hallmarks are mainly determined by autopsy. Until now, there is no effective medical treatment can be used to slow down or stop the progression of AD.[15] However, the symptomatic treatment is accessible on the basis of the cholinergic hypothesis. Cholinesterase inhibitors as chemical messengers increase the level of Ach to compensate the dysfunction of brain cells and are available treatment for memory loss, thinking problems and movement disorders. Until 2017, three cholinesterase inhibitors[16] are approved by the *U.S. Food and Drug Administration* (FDA) to treat AD symptoms, including donepezil, galantamine and rivastigmine (shown in **Table 1**). The proposed working mechanism is to increase the concentration of the chemical messenger at cholinergic synapses by preventing the hydrolysis of Ach. The fourth approved drug memantine is a *N*-methyl-D-aspartate (NMDA) receptor antagonist that enables to block the activity of another neurotransmitter glutamate by binding to NMDA receptors on the surface of brain cells.[16] All these drugs are approved only for the symptom treatment rather than the cure for AD.

Table 1: FDA approved prescription drugs for AD symptoms treatment.

S1
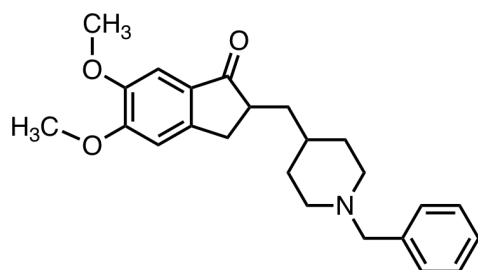
S2
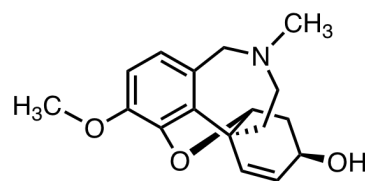
S3
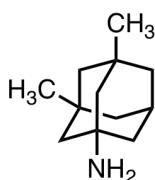
S4
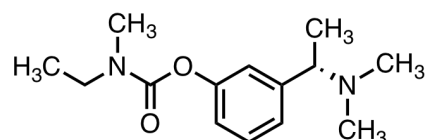
Brand Name	Generic Name	Stage Approved	Structure
Aricept	Donepezil	all stages	S1
Razadyne	Galantamine	mild to moderate	S2
Namenda	Memantine	moderate to severe	S3
Exelon	Rivastigmine	mild to moderate	S4
Namzaric	Memantine + Donepezil	moderate to severe	-

The majority of the potential AD medications development is going after the amyloid cascade hypothesis. In order to decline Aβ production and further to clear Aβ deposition, a number of β, γ-secretase inhibitors, Aβ inhibitors and anti-Aβ monoclonal antibodies (mAbs) are developed based on the amyloid hypothesis. For example, Verubecestat[17] is an inhibitor of β-secretase 1 (BACE 1) to lower the Aβ level in the cerebrospinal fluid of patients in mild to moderate stages, which is designed and synthesized by *Merck & Co.* However, the Phase III clinical trials are discontinued owing to no difference between treatment and placebo groups. Similarly, NGP555,[18,19] as a γ-secretase modulator, is proposed to reduce the production of $A\beta_{42}$ by

promoting the formation of shorter and non-aggregation isoform of amyloid peptide like $A\beta_{37}$ and $A\beta_{38}$, which is developed by *NeuroGenetic Pharmaceuticals, Inc.*

Concerning anti-Aβ approaches,[20–22] active immunotherapy is a hotspot by *long-term antibody production from short-term antibody administration at limited cost*.[23] The most antibodies being studied are listed in **Table 2**. The mAbs targeting with different segments on Aβ show different effectiveness in clearing the aggregates species. Based on the solid-state NMR structural characterization on the $A\beta_{40}$ fibrils derived from the brain tissue of one AD patient,[24] C-termini are formed hydrophobic core that is buried inside the fibrils, whereas N-termini are exposed to the solvent environment which could bind with antibodies. This explains why the N-terminus target mAbs are more effective. However, the poor penetration of anti-Aβ mAbs into central nervous system is a major barrier and limits the efficacy of antibody in AD treatment. Several anti-Aβ antibodies have already failed for the primary efficacy endpoints.

Table 2: Monoclonal antibodies of Aβ and Tau protein.

Antibody	Epitope	Conformation Recognition			Origin	Manufacturer	Status
		Monomer	Oligomer	Fibril			
Bapineuzumab[25]	AA 1-5	√	√	√	Humanized anti-Aβ	*Janssen, Pfizer*	Discontinued
Solanezumab[26]	AA 16-26	√	×	×	Humanized anti-Aβ	*Eli Lilly & Co.*	Phase III
Gantenerumab[27]	AA 3-12, 18-27	weak	√	√	Human anti-Aβ	*Hoffmann-La Roche*	Phase III
Crenezumab[28]	AA 13-24	√	√	√	Humanized anti-Aβ	*AC Immune SA, Genentech, Hoffmann-La Roche*	Phase III
Ponezumab[29]	AA 30-40	√	×	×	Humanized anti-Aβ	*Pfizer*	Discontinued
BAN2401[30]	Protofibrils	-	-	-	Humanized anti-Aβ	*Biogen, Eisai Co., Ltd.*	Phase II
Aducanumab[31]	AA 3-6	×	√	√	Human anti-Aβ	*Biogen, Inc.*	Phase III
C2N 8E12[32]	-	×	-	√	Humanized anti-Tau	*AbbVie, C2N Diagnostics*	Phase II
BIIB076[33]	-	√	-	√	Humanized anti-Tau	*Biogen, Inc.*	Phase I

The failure of anti-Aβ immunotherapy partly attributed to the late intervention in the disease process.[23,34] Early intervention in disease-modifying treatment might have great advantage. Therefore, the AD definitive diagnosis is much more important. To determine AD, physical and neurological examinations are necessary, especially brain imaging of amyloid pathology and tau pathology.[35–39] Biological markers are used to identify the condition and to monitor the changes along the disease progression. There are several criteria for amyloid pathology diagnosis *in vivo*, including high binding affinity and strong binding specificity to amyloid deposits, chemical modification on the biomarkers to cross the blood brain barrier and fast clearance from normal brain tissues. Currently, three FDA approved radiopharmaceuticals are employed to diagnose amyloid plaques in the brain of living patient with positron emission tomography (PET) scan, including Amyvid[40] (florbetapir ^{18}F), Vizamyl[41] (flutemetamol ^{18}F) and NeuraCeq[42] (florbetaben ^{18}F). Fluorine-18 decays to yield stable oxygen-18 with a half-life $t_{1/2}$ of 109.7 minutes, which allows enough time for radiopharmaceutical preparation, proper distribution and delivery to the imaging suite. Positive PET scans display the presence of uptake in the grey matter cortex, whereas negative scans indicate white matter retention increasing. All the three PET biomarkers have similar sensitivity and binding specificity. However, Vizamyl makes the PET scan much easier to read and interpret since it is approved to evaluate the signal intensity of binding to amyloid plaques in a color-calibrated scale.

1.1.1 Amyloid-β Peptide

As a small peptide, Aβ contains 36-43 amino acids and is produced from the cleavage of APP by β- and γ-secretase (**Figure 2**). The imprecise cleavage by γ-secretase in the latter step leads to several isoforms of Aβ peptide with different C-terminuses.[3,43–45] The two major isoforms are Aβ$_{40}$ and Aβ$_{42}$ with an abundance of ~80-90% and ~5-10%, respectively.[46] The ratio of Aβ$_{42}$ to Aβ$_{40}$ is around ~1:9 under normal physiological condition. In familial AD patients, the ratio shifts and results in higher synaptic toxicity as the percentage of Aβ$_{42}$ increases. In terms of the cross-amyloid interactions, Aβ$_{42}$ is able to function as the template to accelerate Aβ$_{40}$ aggregation by minimizing the kinetic energy barriers. On the contrary, the existence of Aβ$_{40}$ cannot facilitate the aggregation of Aβ$_{42}$.[46] Furthermore, the ratio of Aβ$_{42}$ to Aβ$_{40}$ in plasma and cerebrospinal fluid can be used as an indicator to diagnose AD pathology. The lower ratio in plasma, the higher risk of the dementia.[47,48]

D A E F R H D S G Y E V H H Q K L V F F A E D V G S N K G A I I G L M V G G V V I A
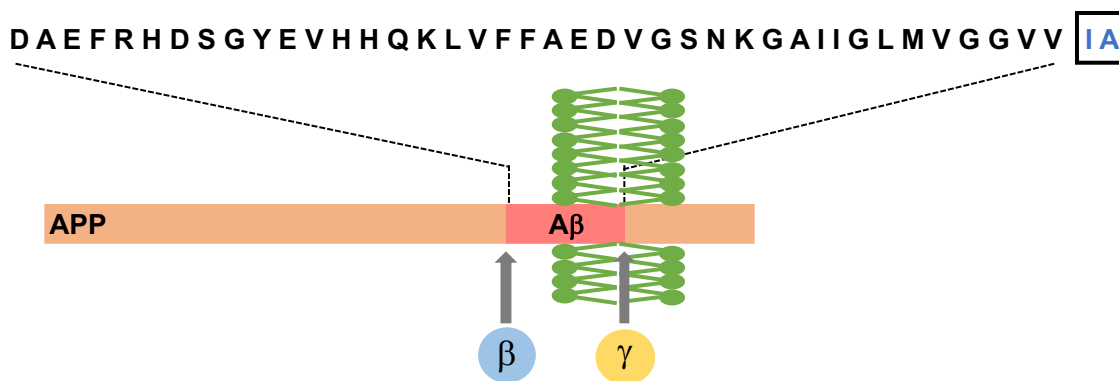
Figure 2: The process of amyloid-β production with the peptide sequence of Aβ40 and Aβ42.

Although there are only two additional hydrophobic amino acids, isoleucine (Ile) and alanine (Ala) in the C-terminal of Aβ42 in comparison with Aβ40, the oligomers formed by Aβ40 and Aβ42 show critical morphological and conformational distinction.[49] The length of the C-terminus in Aβ peptide enables to influence the size distribution of oligomers. Residue Ile41 can modulate the paranucleus formation and residue Ala42 is essential for the further association of paranuclei on the basis of the oligomerize pathway. From the cross-linking results, the bands of Aβ40 monomer, dimer, trimer and tetramer have similar intensities, suggesting that they are in a rapid equilibrium. Similarly, the rapid equilibrium is also present in the oligomerization process of Aβ42. However, a dramatically different oligomer size distribution of Aβ42 was observed. The oligomers of Aβ42 is mainly consisted of pentamer/hexamer as the basic unit to assemble into large intermediates. According to the scattering results, particles with the hydrodynamic radius of 1-2 nm can be detected in low molecular weight Aβ40 oligomers. In contrast, the hydrodynamic radius of low molecular weight Aβ42 oligomers were around 6-7 nm.[49]

The formation of amyloid aggregates proceeds through a primary nucleation pathway and the kinetics process corresponds to a sigmoid growth curve (**Figure 3**).[5,44,50,51] The fibrillation process is characterized by three different phases: lag phase, growth phase and saturation phase. In the initial lag phase, unstructured soluble monomeric Aβ peptide accumulates to form nucleus. A rapid growth phase follows, in which the monomer assembles into oligomers, protofibrils and mature fibrils with distinct morphologies until the final saturation plateau phase. Researchers find that the critical concentration for the aggregation of Aβ peptide is ~17.5 μM *in vitro*.[52] Although the physiological concentration of Aβ in brain is significantly lower than this micromolar level,

the fibrillation can still be triggered *in vivo* owing to the template action of cell membranes. In this case, the function of the membrane environment could lower the energy barrier of the nucleation.
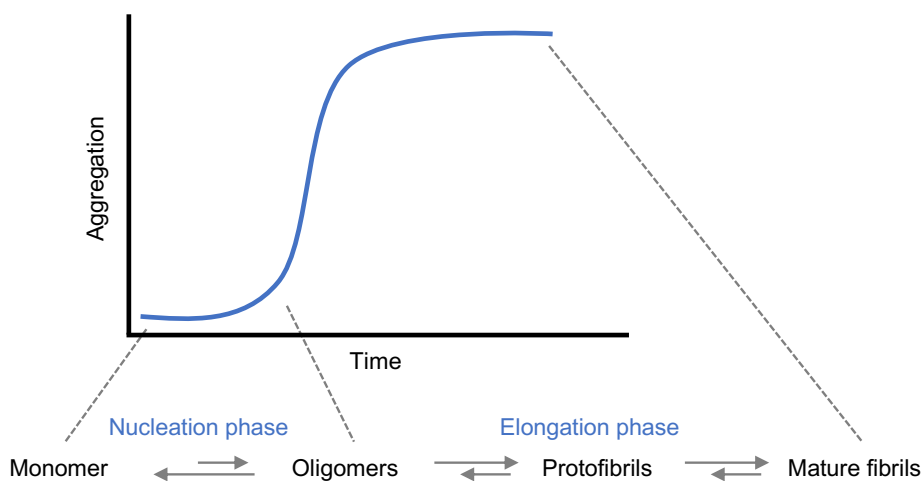
Figure 3: The aggregation kinetics of Aβ peptide in a sigmoid growth curve.

The mechanism of amyloid aggregation process is highly complex and contains with multistep aggregation kinetics. Other than the homogenous primary nucleation pathway discussed above, the secondary nucleation pathway has also been reported in several amyloid systems.[53–55] The difference between these two nucleation pathways is the rate of new aggregates generation. Specifically, the rate of new aggregates generation in the primary nucleation pathway is dependent on the monomer concentration only and uncorrelated to the fibrils concentration. On the contrary, the rate of new aggregates generation in the secondary nucleation pathway has direct relation to the existing fibrils concentration. At a low concentration of monomeric Aβ peptide, the aggregation process follows the primary nucleation pathway to form aggregates. When it reaches the critical concentration for amyloid fibrils formation, enough surface for monomer attachment is presented inside the system. Then the secondary nucleation pathway occurs through a fibril catalyzed reaction leading to the formation of toxic oligomeric species, and these toxic oligomers are related to AD. It should be noted that the secondary nucleation pathway is divided into monomer-dependent and monomer-independent processes. Taken together, the aggregation pathway of new aggregates formation includes three classes of mechanism, namely the primary pathway aggregation, the secondary pathway aggregation dependent on the existing fibrils and the secondary pathway aggregation dependent on both monomer and the existing fibrils.

Nowadays, retinoid A receptor (RAR) and retinoid X receptor (RXR) ligands were demonstrated to be functioned as the inhibitor for $A\beta_{42}$ aggregation at different extents in both the primary and the secondary nucleation pathway. The quantitative analysis of the inhibitory effects on the aggregation kinetics indicated that the above ligands induced the similar $A\beta_{42}$ fibrillar species formation in a concentration-dependent. RAR and RXR ligands can bind to monomers, primary oligomers, secondary oligomers and fibrils.[56] This research provides us remarkably effective approach for drug discovery against AD. The small molecules which are able to bind with the common species during the aggregation process and inhibit the aggregation accordingly might be potential therapeutic strategy for AD.

1.1.2 Amyloid Biomarker for Research

1.1.2.1 Thioflavin-T

Thioflavin-T (ThT), as a fluorescent marker for amyloid deposits, is applied to monitor and quantify the presence of misfolded aggregates and amyloid fibrils *in vitro*, and also can be employed to detect the potency and kinetics of amyloid inhibitors.[57–61] Upon binding to amyloid aggregates, the maximum excitation and emission wavelengths of ThT are redshifted to 445 nm and 480 nm, respectively. ThT is found to form micelles above 4 μM concentration in aqueous solution. The micelles formation of ThT is able to enhance the fluorescence emission by forming the hydrogen bond between charged nitrogen and fibrils. However, the ThT micelles disrupted at very low pH conditions.[62] The hydrophobic property of the molecule arises from the *N, N*-dimethyl group on the phenyl ring (**Figure 4**, left) in combination with the polar benzothiazole group.

In the photophysical view, *the fluorescence properties of ThT are determined by the extent of quenching of the locally excited (LE) state to a dark twisted intra-molecular charge-transfer (TICT) state*.[60] The fluorescence intensity of ThT is simultaneously increasing due to the block of rotation along the shared C–C bond. When the binding sites are all occupied with amyloid fibrils, the fluorescence intensity reaches a plateau.[62–66] The intensive use of ThT *in vitro* to probe amyloid proteins is on the basis of the structural similarity of diverse amyloid fibrils regardless of protein sequences. Amyloid fibrils share the cross-β pattern structures, and each β-strand is perpendicular to the cross-β architecture, i.e. the long fibrils axis. The similar nature of amyloid fibrils structure

is attributed to the common hydrogen bonds in the main chain to all peptides which is functioned as the main force to stabilize the structure.

Concerning the binding sites and binding mechanism of ThT with amyloid aggregates, the molecular dynamics simulation results suggest that the binding sites for ThT in the amyloid aggregates are possible to locate at the exposed β-sheet edges, the surface of β-sheet, and the β-sheet interface. The simulation also demonstrates that ThT binds parallel to the fibrils axis and locates on the surface of the cross-β structures. As a result of the large hydrophobic surfaces, ThT especially bind with the side-chain of aromatic and hydrophobic residues. The minimal binding motif is 3-4 β strands in the cross-strand ladder formed by residue sidechain (with inter-strand spacing 4.8 Å), since the length is closer to the head to tail of ThT (~15 Å).[67,68] Moreover, ThT cannot bind with highly charged amyloid fibrils because of the electrostatic repulsion.[64]

1.1.2.2 Pittsburgh Compound B

Klunk and Mathis designed a neutral molecule named Pittsburgh compound B (PiB, **Figure 4**, right) based on the chemical modification on the structure of ThT. Recently, PiB is generally used as a standard PET imaging radiotracer for amyloid plaques detection and further for the diagnosis of AD.[69–73] As a ThT derivative, ^{11}C-labeled PiB has a high binding affinity to Aβ fibrils with the dissociation constant K_d of 1 to 2 nM, and high initial uptake and a rapid clearance. The regional retention rates allow for the detection and quantitative measurement of Aβ deposition. The increased retention of PiB in the brain is because of a large amount of amyloid deposits.[71] Furthermore, PiB-positive subjects with mild cognitive impairment (MCI) are more likely to convert to AD than PiB-negative subjects.[74] As such, PiB tracer can be employed as a prospective candidate for the disease progression prediction.

According to a recent research, PiB shows different binding capacities to different states of Aβ aggregates. The stronger binding interactions of PiB to both Aβ fibrils and protofibrils were determined. Meanwhile, the binding interaction between PiB and Aβ oligomers was displayed a lower binding affinity compared with mature fibrils. In addition, the binding affinity of PiB to Aβ$_{40}$ oligomers and protofibrils is lower than Aβ$_{42}$ oligomers and protofibrils.[75] From the simulation data, PiB is able to selectively bind with the hydrophobic grooves on the β-sheet surface

of Aβ protofibrils. Due to the high hydrophobicity of PiB, the insertion into the surface groove is much deeper than ThT.[76]

PiB cannot only specifically bind with amyloid plaques, but also binds with a range of amyloid plaques including diffuse plaques and cerebrovascular amyloid angiopathy.[77] Therefore, PiB is a standard imaging marker for research. However, the short half-time $t_{1/2}$ of ^{11}C isotopic agent limits the widely usage of PiB compared to ^{18}F-labeled radiotracers. It is worth noting that amyloid PET imaging cannot provide the accuracy diagnosis of a specific disease state. Moreover, it cannot provide any evidence to differentiate AD from other amyloidosis as well.
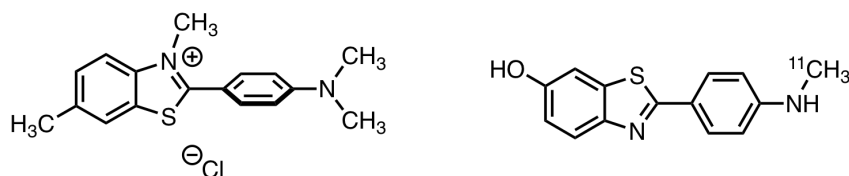
Figure 4: Structures of ThT (left) and ^{11}C-PiB (right).

1.1.3 Amyloid Inhibitor

1.1.3.1 EGCG

Polyphenols are a large group of natural and synthetic small molecules that are composed of one or more aromatic phenolic rings. Several small polyphenols have been demonstrated to remarkably prevent the formation of fibrillary assemblies *in vitro* and reduce their associated cytotoxicity. Green tea extract epigallocatechin-3-gallate (EGCG, **Figure 5**) is used as an anti-oxidative and anti-inflammatory agent for numerous human diseases. EGCG was demonstrated to control metal-induced Aβ aggregation, thus attenuated reactive oxygen species (ROS) formation by metal-Aβ or regulated metal-Aβ toxicity *in vitro* and living cells.

In the ThT binding assay, the prolonged lag phase and decreasing of the fluorescence intensity after EGCG treatment suggests that EGCG enables to inhibit the fibrillation of Aβ peptide. The intensity decline can be explained in two different aspects. On one hand, EGCG is probably capable to compete the hydrophobic binding sites with ThT, thus induces the intensity decline. On the other hand, the structure remodeling of fibrils after EGCG treatment causes the fluorescence intensity decreasing, further to initialize the occurrence of fluorescence quench. EGCG is prone to

bind with unfolded amyloid peptide and prevents on-pathway fibrillation process by forming the off-pathway oligomers. This structural distinct oligomer is unstructured, non-toxic and not recognized by A11 antibody.[78] EGCG could also bind with $A\beta_{42}$ oligomers and thus alters their morphology to prevent the on-pathway fibrils formation. In addition, EGCG remodels the large, mature fibrils (Aβ fibrils and α-synuclein fibrils) into smaller, nontoxic amorphous protein aggregates by adjusting the equilibrium among monomer and different states of amyloid aggregates.[79] After EGCG treatment, Aβ peptide precipitates fast out of solution. Chemical shifts changes from solution-state NMR HSQC spectra suggests the presence of the interactions between EGCG and Aβ. Broad linewidth in side chain of histidine and the assignment of C–C correlation spectrum in solid-state NMR indicates that EGCG interacts with the aromatic hydrophobic core of Aβ.[80]
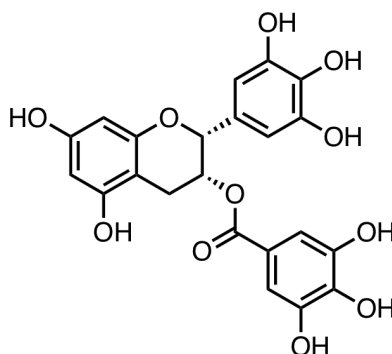
Figure 5: Structure of EGCG.

1.1.3.2 Cross-amyloid Interaction Surface Mimics

Protein misfolding[50] is involved in several fatal diseases, such as Alzheimer's disease, type II diabetes, Huntington disease and Parkinson disease. Designing peptide mimics to suppress amyloid fibrils formation and to reduce the toxicity of amyloid aggregates is helpful to drug discovery.[81–84] Cross-amyloid interaction surface mimics (ISMs) have been presented as the potential inhibitors for Aβ and hIAPP amyloidogenesis and cytotoxicity.[85] Chemical design approach[82,86,87] of peptide mimic is based on the protein-protein interactions, especially on the key segment for self-association and cross-interaction. Amino acid substitution, backbone and side chain modifications, peptide cyclization and termini alternation are applied to design and synthesize peptide-based drugs as amyloid inhibitors. Although peptide-based drugs (fewer than

50 aa) have low oral bioavailability, low metabolic stability and poor membrane permeability in comparison to small molecule drugs. The potential advantages of peptide-based drugs have high potency, high specificity, and broad range of targets with lower toxicity induced by side-effects.[88,89]

The first generation of the amyloidogenic sequence-based inhibitors are highly effective to prevent the fibrillation process and reduce the corresponding toxicity. For example, after determination of the shortest sequence (LVFFA) of Aβ which enables to aggregate into fibrils, several rationally designed peptides are proposed as inhibitors for Aβ fibrillation. However, the disadvantage of this kind of inhibitor is the self-assembly issue. In order to corrupt the hydrophobic patches and avoid the mimics self-aggregation, the modification of *N*-methylation is introduced to produce a non-amyloidogenic mimetic inhibitor. Apart from the self-aggregation issue, the solubility of peptide mimics is another complicated problem. Such problem is solved by changing the charge distribution of the mimics. Taken together, the design strategy of peptide mimic drug requires the comprehensive and careful estimation of different drug candidates according to the design aim.

Yan and coworkers demonstrated that *N*-methylated modification at residue Gly24 and Ile26 on full length islet amyloid polypeptide (IAPP) mimic termed IAPP-GI is functioned to inhibit itself fibrillation at nanomolar range concentration. IAPP-GI binds with monomeric IAPP, furthermore to block the assembly process.[90] According to the cross-amyloid interactions, Andreetto and coworkers identified two segments as the interaction interface for both self-association and cross-interaction of Aβ and IAPP.[85,91] IAPP (8-18) and IAPP (22-28) are defined as the two hot segments.[85,92] In order to yield a non-amyloidogenic ISM peptide inhibitor, the hydrogen bonds formation in inter-molecular backbone NH to CO need to be terminated, further to prevent peptide itself extension to protofilament and amyloid fibrils. *N*-methylation modification is applied at residue Gly24 and Ile26, which are located at the same side of β-strand in the amyloid core to eliminate the hydrogen bond formation.[93] A hot-segment-linking approach based on the IAPP sequence is used to yield a highly soluble, non-amyloidogenic and non-toxic amyloid inhibitor, which prohibits the fibrillation and reduces the cytotoxicity for both Aβ and IAPP. The linker not only connects the two segments, but also determines the property and structure of ISMs.
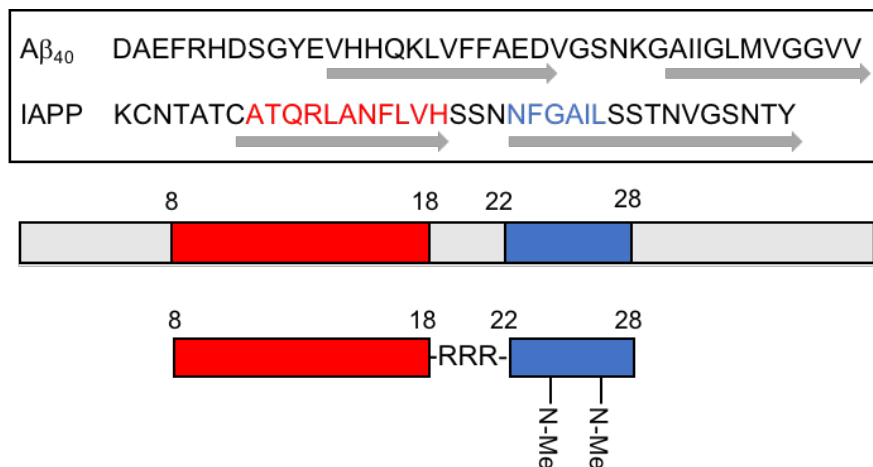
Figure 6: Design strategy of ISMs inhibitors with the hot-segment-linking approach. Figure was adapted from reference 85.

Other than the IAPP mimics inhibitors, transthyretin (TTR) derived mimics are also designed as peptide mimetic inhibitors. TTR prefers to bind with Aβ oligomers and fibrils rather than Aβ monomer. The binding sites are located at the central cavity of TTR tetramer. Meanwhile, the segment contains residue 106-117 (TIAALLSPYSYS) of TTR is detected to has strong binding affinity to Aβ.[94] Taking the binding interaction into consideration, TTR-derived cyclic peptide mimic[87] is designed by preserving the residues for TTR-Aβ interaction, inserting ^Dproline to introduce the β-turn structure and cyclization. Subsequently, tyrosine and lysine are inserted to stabilize the β-sheet structure, insertion of valine and isoleucine is aimed to increase the β-sheet propensity. Gln-Ser-Lys segment is used to facilitate the cyclization. In combination with all the chemical modifications described above, the structural mimic is extremely effective as an inhibitor for Aβ to suppress Aβ aggregation and protect the neurons from Aβ toxicity.

1.2 Solid-state Nuclear Magnetic Resonance

Solid-state NMR is a powerful and specific technique for amyloid aggregates structure elucidation, as the insoluble and non-crystallizing property of amyloid misfolding proteins.[95–97] The atomic resolution structure of amyloid misfolding protein is determined on the basis of the secondary chemical shifts and the spatial contacts. However, the restriction of molecular motion in solid phase leads to a broaden solid-state NMR spectrum. Dipolar coupling, chemical shift anisotropy (CSA) interaction and quadrupolar interaction cause the linewidth broadening in solid-state NMR. CSA interaction is the main reason of spectra broadening. In order to obtain high-resolution solid-state NMR spectra, magic angle spinning (MAS) and cross polarization (CP) techniques are used to eliminate or reduce the effects of the dipolar coupling and CSA interaction. In combination of MAS and CP, the resolution is significantly improved for peak identification and data analysis.

1.2.1 Chemical Shift

In NMR spectroscopy, the chemical shift (CS) is the resonant frequency of an atomic nucleus relative to a standard in a magnetic field.[98] Chemical shift δ is dependent on the electron density and formulated in parts per million (ppm) by frequency as follows:

$$\delta = \frac{\nu - \nu_{ref}}{\nu_{ref}}$$

The induced magnetic field is defined as shielding effect, which is generated by the electrons around the nucleus offsetting the effect of the external magnetic field. The main reason that causes chemical shift is because of the shielding effect. The higher electron density, the higher of the shielding effect. Due to the sensitivity of CS to the electronic environment, CS mapping is suitable to identify the interaction interface of direct interactions from a binding partner and structural conformational rearrangement of a protein through the indirect interactions with a ligand.

1.2.2 Magic Angle Spinning

In solids, dipolar coupling interaction, CSA interaction and quadrupolar interaction are dependent on orientation, and all these interactions contain the $(3cos\theta^2 - 1)$ term. When magic angle $\theta = 54.74°$, where $3cos\theta^2 - 1 = 0$, the above three interactions are averaged, and a high-resolution spectrum is yielded.[99–101] When the spinning speed is sufficiently fast and beyond the anisotropy

interactions, the isotropic interaction is retained in the spectrum. It turns out that the isotropic chemical shift and a series of rotational sidebands signals with the frequency interval of the spinning speed can be detected. The rotor is spinning at the magic angle with the respect to the magnetic field in the z-direction by gas flow in MAS technique. The limitation of the spinning speed is dependent on the outer and inner diameter (O.D. and I.D.) of the rotors. The smaller the rotor diameter is, the higher spinning speed can be achieved. Nowadays, a 0.7 mm MAS solid-state NMR rotor enables the spinning rates up to 111 kHz. The detailed information of the MAS solid-state NMR rotor size is listed in **Table 3**.
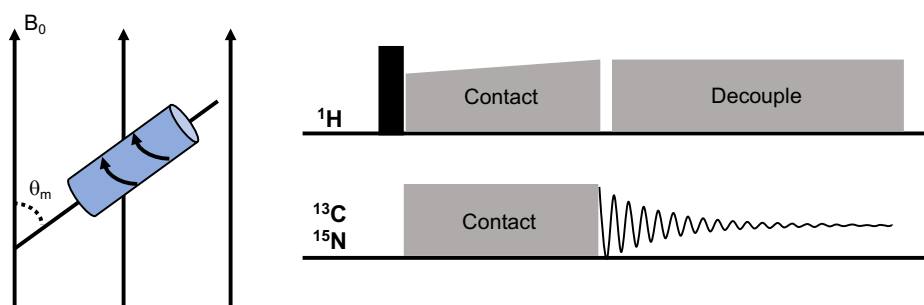
Figure 7: A schematic diagram of magic angle (left) and pulse sequence of CP (right).

Table 3: List of description for MAS solid-state NMR rotors.

Comparison	0.7 mm	1.3 mm	1.9 mm	2.5 mm thin wall	3.2 mm thick wall	3.2 mm thin wall	4 mm
Material	Zirconia [ZrO_2]	Zirconia [ZrO_2]	Zirconia [ZrO_2]	Zirconia [ZrO_2]	Zirconia [ZrO_2]	Zirconia [ZrO_2]	Zirconia [ZrO_2]
O. D.	0.7 mm	1.3 mm	1.9 mm	2.5 mm	3.2 mm	3.2 mm	4.0 mm
I. D.	0.5 mm	0.9 mm	1.5 mm	1.7 mm	2.2 mm	2.6 mm	3.0 mm
Active volume	0.59 μL	2.5 μL	13.1 μL	12 μL	32.1 μL	46.7 μL	80 μL
Max speed	111 kHz	67 kHz	42 kHz	35 kHz	24 kHz	24 kHz	15 kHz

1.2.3   Cross Polarization

Cross polarization technique[102,103] is applied to improve the sensitivity of heteronuclear NMR experiments by transferring the polarization from the abundant nucleus I (^{1}H or ^{19}F) to the dilute nucleus S (^{13}C or ^{15}N). The diagram of the pulse sequence is shown in **Figure 7**. NMR signals can

be increased by a factor γ_I/γ_S. In order to perform the polarization transfer, the magnetization of abundant nuclei and dilute nuclei need to match the Hartmann-Hahn matching condition.

$$\gamma_I B_1(\text{I}) = \gamma_S B_1(\text{S}) \text{ or } \omega_1^I = \omega_1^S$$

The matching condition under MAS is $\omega_1^I - \omega_1^S = \pm \omega_R$. The acquisition time of CP experiment is dependent on the spin-lattice relaxation time of the abundant spin I, which is shorter than the spin-lattice relaxation time of the dilute spin S. It indicates that more number of scans can be recorded at the same acquisition time. As CP method is based on the heteronuclear dipolar coupling interactions, the inter-nuclear distance information can also be obtained. However, the major challenge of CP experiment is the high irradiation power may damage either the sample or the probe.

1.2.4 Sequential Assignment for Proteins in Solid-state NMR

Resonances assignment is mandatory for protein structural determination.[104–106] In order to proceed the backbone and sidechain assignment of uniformly ^{13}C, ^{15}N-labeled proteins, it is necessary to record a series of solid-state NMR spectra, including a homo-nuclear C–C correlation spectrum (such as proton-driven spin diffusion, PDSD) with a short PDSD mixing time to assign the side chain of an amino acid in the same residue, and specific hetero-nuclear N–C magnetization transfer combined with C–C transfer spectra (such as NCACX and NCOCX experiments) to continue the sequential assignment in the adjacent residues of a protein.[107]

In NCACX experiment, the magnetization transfers from ^{1}H to ^{15}N, then selectively to the ^{13}Cα. All ^{13}C and ^{15}N resonances are detected in the same amino acid when setting up the short mixing time for the last CX mixing step. Similarly, in NCOCX experiment, the magnetization transfers from ^{1}H to ^{15}N, then selectively to the ^{13}CO. In short mixing time for the last CX step, the ^{15}N resonances are from residue *i* and all ^{13}C resonances are from residue *i-1*. With a combination of NCACX and NCOCX experiments, the backbone atoms are able to be sequentially assigned. The schematic diagram of the magnetization transfer is shown in **Figure 8**.

Generally, the assignment strategy is divided into two steps. First is the spin system assignment of ^{13}C resonances from the same residue in ^{13}C homo-nuclear correlation experiment, in which the

sidechain ^{13}C atoms are able to be identified. The second step is the sequential assignment through selectively transfer from ^{15}N backbone to [13]Cα or [13]CO, which involves one residue *i* and the previous residue *i-1*. N_iCA_i and N_iCO_{i-1} transfer experiments enable us to distinguish the intra- and inter-residue contacts. As such, it is possible to carry out the assignment theoretically. However, the low sensitivity and poor resolution of uniformly labeled proteins in non-crystalline state make the practical assignment much more difficult and time-consuming.[108] Furthermore, the secondary structure and low diversity of the amino acid composition like low-complexity regions and repetition in the protein sequence, also induce big problems for the resonances assignment.
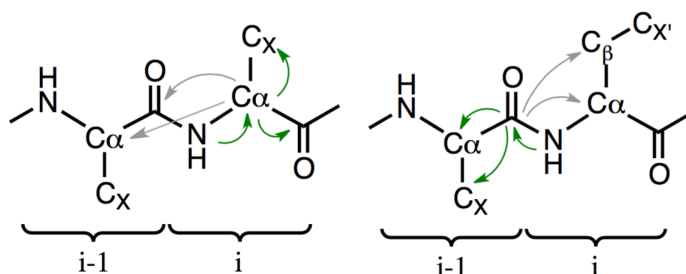
Figure 8: Magnetization transfer in 3D NCACX (left) and NCOCX (right) assignment experiments.

1.2.5   Proton Detection Solid-state NMR Spectroscopy

The high natural abundance and high gyromagnetic ratio of proton can provide higher detection sensitivity in comparison with carbon or nitrogen. Therefore, the proton detection attracts more attention in MAS solid-state NMR. However, the progress of proton-detected experiments is limited due to the linewidth broadening of ^{1}H signal which is induced by homo-nuclear proton dipolar couplings. Recently, per-deuteration sample preparation and ultra-fast MAS spinning speed technique make progress of the proton-detected solid-state NMR experiments for fibrillary and membrane proteins.[109–113]

In the sample preparation, recombinant protein is expressed in a deuterated growth medium with a defined ratio of D_2O to H_2O in order to achieve proton dilution at exchangeable sites like amine and hydroxyl group. High resolution spectra can be obtained via back-exchange of deuterons by protons. However, the proton dilution decreases the sensitivity of ^{1}H signal. Highly deuterated sample and full reprotonation under ultra-fast spinning are able to compensate for the sensitivity loss. Resonance assignment from the proton detection experiment is able to achieve with a combination of several assignment strategies and different labeling schemes.[114]

1.2.6   NMR Structural Characterization of Aβ Aggregates

1.2.6.1 Aβ Oligomers

Aβ oligomers/intermediates rather than Aβ mature fibrils are more cytotoxicity and able to cause synaptic dysfunction. To obtain deep understanding of the pathological mechanism induced by Aβ aggregates, a lot of researches were conducted to characterize the structures of different Aβ aggregates, including oligomer, protofibrils and fibrils. The structural differences of Aβ aggregates could provide an explanation for the different levels of toxicity. It should be noted that Aβ aggregates without exception show amyloid polymorphism at the atomic molecular level.

The Ishii group captured a late-stage diffusible $Aβ_{40}$ intermediate ($I_β$) and characterized the molecular structure and fibrillation kinetics by MAS solid-state NMR, transmission electron microscopy (TEM) and ThT fluorescence spectroscopy.[115,116] The kinetic model was proposed as follows. First, random coil $Aβ_{40}$ monomers self-associated into $I_{Nβ}$ species, which did not contain any β-sheet structures. Then $I_{Nβ}$ species aggregated to form a spherical species $I_β$ with the diameter of 15-35 nm. Although $I_β$ species and $Aβ_{40}$ fibrils shared the similar well-ordered parallel β-sheet structure, $I_β$ was more toxicity compared with $Aβ_{40}$ fibrils. In the final step, this on-pathway intermediate $I_β$ assembled into protofibrils and mature fibrils. However, the role of the intermediate $I_β$ in the AD pathological relevance is not yet clear. Due to the structural similarity between $I_β$ and $Aβ_{40}$ fibrils, the therapies targeting β-sheet structures is expected effective against the intermediate as well.
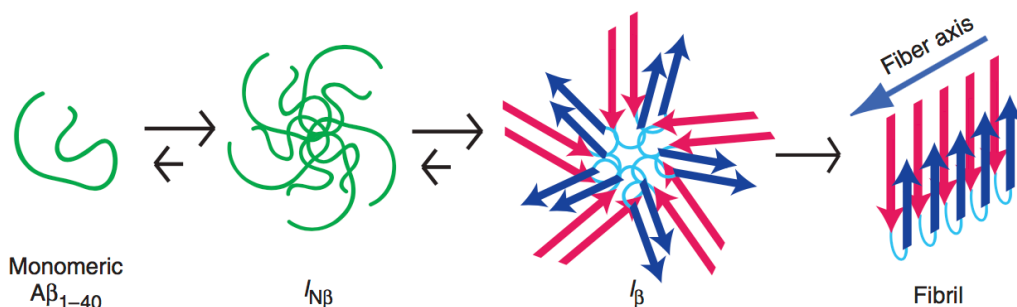
Figure 9: The kinetic model of the fibrillation process of Aβ, reprinted from reference 116.

In comparison with Aβ40 oligomers, it is difficult to prepare Aβ42 oligomers as the faster aggregation process. Under low-temperature and low-salt condition, the Smith group successfully prepared the stable Aβ42 oligomers.[117] Combining with single-touch atomic force microscope (AFM), size exclusion chromatography (SEC) and native gel electrophoresis, the Aβ42 oligomers were disc-shaped pentamers and decamers, with the average widths of 10-15 nm, and the heights of 2-4 nm. Based on NMR result, the compact fold structure of the Aβ42 oligomers were facilitated by several contacts like His13-Gln15, Gly25-Gly29, Gly37-Gly38 and Phe19-Leu34. More interestingly, the above Aβ42 oligomers exhibited loosely strands instead of β-sheet secondary structure, and with more toxicity than mature Aβ42 fibrils. After incubation, Aβ42 fibrils were formed with the parallel β-sheet and in-register arrangement.

1.2.6.2 Aβ Fibrils

Generally, amyloid polymorphism is independent on the protein sequence. Different structural morphologies are induced by different fibrils preparation conditions. Until now, there are many atomic resolution models for Aβ40 fibrils. Tycko's group has proposed two different structural models (**Figure 10**) with the distinct morphologies generated from different preparation conditions *in vitro*.[118,119] Under a brief sonication once per hour in 9 days, the fibrils were produced with a twisted morphology, containing a three-fold symmetry along the fibril axis. In contrast, under the agitation condition the fibrils exhibited in a striated ribbon morphology containing with a two-fold symmetry along the fibril axis.
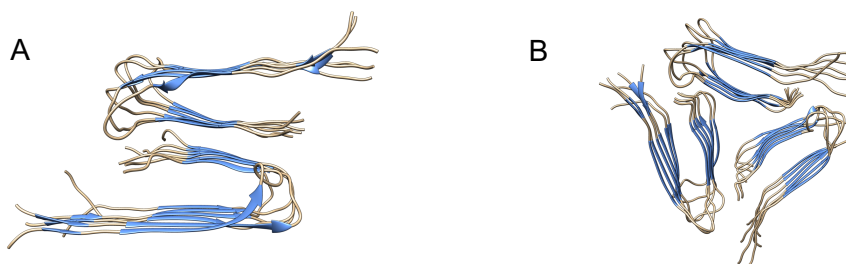
Figure 10: Structural models of Aβ40 fibrils based on the solid-state NMR restraints. A: two-fold symmetry (PDB: 2LMN). B: three-fold symmetry (PDB: 2LMP).

The above two NMR samples of Aβ40 fibrils from Tycko were prepared from the chemical synthetic monomeric Aβ40 peptide. In the meantime, a recombinant uniformly [^{13}C, ^{15}N]-labeled

Aβ40 fibrils sample was prepared from Bertini and Luchinat, which yielded high resolution and sensitivity solid-state NMR spectra.[120] The preparation induced new conformational fibrils with high homogeneity. On the basis of EM and solid-state NMR, a new structural model for Aβ40 fibrils was proposed, in which Aβ40 molecule formed mainly striated bundles (3-5 nm range) fibrils without any twisted pairs. The secondary structure of each Aβ40 molecule was determined with the U-shaped β1-turn-β2 structure. The inter-molecular interactions were detected at the side chain of Met35 with the C-terminus, and the inter-molecular interface shared β2 strand. This work provides us the atomic level structure of Aβ40 fibrils and confirms the complexity of the fibrillation process and highly conformational diversity of Aβ40 fibrils.

Apart from the fibrils formed *in vitro*, Aβ40 fibrils derived from the patient brain tissue have been studied by solid-state NMR and TEM.[24] The brain derived fibrils were not polymorphic, which was clearly distinct from Aβ fibrils prepared *in vitro*. In addition, a number of irregular secondary structures in residues of Aβ40 fibrils were identified as the most striking features, including a twist in residues 19-23, a kink at residue Gly33 and a bend in residue Gly37 and Gly38. As a supplement, mass-per-length (MPL) data demonstrated that this kind of fibrils contained a three-fold symmetry. Both solid-state NMR and TEM results revealed that the differences in AD disease progression may correlate with the different structures of Aβ fibrils. Aβ fibrils could initiate inflammation, oxidative damage or other pathogenic processes in the brain tissue as well. Several researches to develop anti-Aβ monoclonal antibodies are ongoing based on the brain tissue fibrils structure.

The molecular structure of Aβ40 fibrils formed in the phospholipid vesicles was also performed by MAS solid-state NMR.[121] In lipid environment, the fibrils were highly homogenous and only one single set of CS was observed from solid-state NMR. Compared with the solution environment, the negatively charged lipid significantly accelerated the fibrils formation kinetics of Aβ40 peptide. The lipid fibrils contained a kink at residue Gly33 and a bend at residues Gly37-38, thus leading to a distorted structure in the β2 strand and nonparallel contact pattern between the β1 and β2 strand. In contrast, the solution fibrils contained parallel β1 and β2 strand without a kink structure. The remarkable difference can be attributed to the template effect of anionic phospholipids in Aβ40 fibrils nucleation. With a combination of labeling strategies and multi-dimensional assignment experiments, many intra-molecular restraints were assigned, including Val39-Leu17 and Ile32-

Glu22, and as well as inter-molecular distance restraints containing Val39-Gly29, Val39-Ala30, Val39-Ile31, Gly38-Ile31 and Gly38-Ile32 of the lipid fibrils. Based on the results, the authors proposed that the interactions between Aβ40 and membrane were the major driving forces of Aβ40 molecules self-assembly, as the two-dimensional membrane matrix may provide a freer and more unlimited environment for Aβ40 molecules self-association.

Compared with Aβ40 fibrils, Aβ42 fibrils[122,123] are highly homogenous with only one morphology in most cases (**Figure 11**). The molecules were arranged in a parallel in-register array with a two-fold symmetry. In each monomer, an S-shape structure was formed by four β-strands with two hydrophobic cores buried inside the fibrils structure. In each fibril layer, two Aβ42 molecules were contacting by the inter-molecular interactions, including Met35-Gln15', Met35-Leu17', Leu34-Leu34' on the different molecules. In consistent with the results published by the group of Ishii,[124] a same salt bridge between Lys28 and Ala42 was detected in Aβ42 fibrils.

Figure 11: Structural models of Aβ42 fibrils based on the solid-state NMR restraints (PDB ID: A-2NAO, B-5KK3).

The structural determination for Aβ42 fibrils was also conducted by cryo-EM.[125] From the cryo-EM results, there were two inter-wined protofilaments in the Aβ42 fibrils with 4 Å resolution. The β-strand segments were organized into parallel in-register array, which was the same with the solid-state NMR structure presented above. However, the difference is that the peripheral β-sheets are tilted along with the growth axis of fibrils by ~10°. In addition, the dimer interface and the turn region of residues 20 to 25 also show much difference compared with the NMR structure.

Table 4: List of solid-state NMR structures for Aβ$_{40}$ fibrils.

Comparison	Tycko (2006, 2008)	Bertini (2011)	Reif (2012)[126]	Brain-derived (2013)
Peptide preparation	synthetic protein	recombinant protein	recombinant protein	Recombinant protein synthetic protein
Fibrils preparation	seeds, 210 μM Aβ$_{40}$ 24 °C, sonication & agitation	100 μM Aβ$_{40}$ 37 °C, shaking, 4 weeks	seeds, 30-50 μM Aβ$_{40}$ RT, agitation, 7 days	brain tissue seeds, 24 °C, 100 μM Aβ$_{40}$
Buffer condition	10 mM phosphate, pH 7.4	50 mM ammonium acetate, pH 8.5	50 mM phosphate pH 7.0 - 7.2	10 mM phosphate pH 7.4
Morphology	twisted-pair (brief sonication) striated ribbon (agitation)	striated bundles	polymorphism, twisted, two conformers	Patient I: distinct from the fibrils *in vitro* Patient II: twisted
Secondary structure	triple β-strands	β-strand-turn-β-strand U-shape	I: β-sheet-turn-β-sheet II: β-sheet only	β-strand conformation
Tertiary structure	in-register parallel β-sheet	in-register parallel β-sheet	-	in-register parallel β-sheet
Quaternary structure	three-fold symmetry (brief sonication) two-fold symmetry (agitation)	dimeric structure	asymmetric dimer	three-fold symmetry
Salt bridge	Asp23-Lys28 (only presence in two-fold symmetry fibrils)	-	Asp23-Lys28	Asp23-Lys28

Table 5: *List of solid-state NMR structures and Cryo-EM structure for Aβ42 fibrils.*

Comparison	Ishii (2015)	Griffin (2016)	Meier & Riek (2016)	Willbold & Schröder
Peptide preparation	chemically synthesis	recombinant protein	recombinant protein with N-terminal His-tag	recombinant protein
Fibrils preparation	5% seeds, ~ 50 µM Aβ42 RT, 3–4 days	10–50 µM Aβ42 RT, hydrated fibrils	seeds, 100 µM Aβ42 37 °C, shaking	RT, 8 weeks
Buffer condition	10 mM phosphate buffer pH 7.4	20 mM sodium phosphate 0.2 mM EDTA, pH 8.0	100 mM phosphate 100 mM NaCl 100 µM ZnCl2, pH 7.4	30% ACN, 0.1% TFA, pH 2
Secondary structure	triple β-strands (S-shape) in-register parallel β-sheet	four β-strands (S-shape) in-register parallel β-sheet	five β-strands (horseshoe) in-register parallel β-sheet	four β-strands (LS-shape) in-register parallel β-sheet
Tertiary structure				
Quaternary structure	-	dimeric structure	dimeric structure	~10° six subunits Asp1-Lys28
Salt bridge	Lys28-Ala42	Lys28-Ala42	Lys28-Ala42	Asp7-Arg5 Glu11-His6 Glu11-His13
Inter-molecular interactions	-	Leu17'-Met35, Gln15'-Met35	Leu17'-Met35, Gln15'-Met35	Asp1 (i) -Lys28 (i-5) Phe4 (i) - Leu34 (i-2) Phe4 (i) - Val36 (i-2)

Chapter 2

Methods and Materials

2 Methods and Materials

2.1 Interactions between Aβ_{40} Fibrils and Small Molecules

2.1.1 Expression, Purification and Fibrils Preparation

The plasmid construct of Aβ_{40} was expressed in BL21 (DE3) *Escherichia coli* strains. The expression plasmid was spread on a LB agar plate supplemented with antibiotics kanamycin with the final concentration of 50 mg/L. Single colonies were inoculated to LB medium which contains 50 mg/L of kanamycin and incubated in an orbital shaker at 37 °C overnight. Then 10 mL overnight cultures were centrifuged and resuspended into 500 mL M9 medium with glucose (2 g/L) and NH$_4$Cl (1 g/L). Aβ_{40} peptide expression was induced with 1 mM isopropyl-β-D-thiogalactoside (IPTG) until the optical density (OD) values at 600 nm reached 0.6-0.7. The cells were harvested after 4 hours incubation at 37 °C with vigorous shaking.

The cell pellets from 1 L culture were resuspended in 20 mM Tris/HCl buffer (pH 8.0), containing 1 mL of 1 mg/mL DNase and 1 tablet of protease inhibitor cocktail. After stirring 15 minutes at room temperature, the cell pellets were disrupted with cell cracker and centrifuged for 30 minutes at 20,000 rpm. Then the pellet was resuspended in 20 mM Tris/HCl buffer containing 0.4% Triton X-100. Sonicated and centrifuged as above. The second pellets were washed twice with 20 mM Tris/HCl buffer, followed by dissolving the inclusion bodies with 40 mL lysis buffer (8 M guanidinium chloride, 20 mM Tris/HCl pH 8.0).

The above dissolved inclusion bodies were centrifuged for 30 minutes at 20,000 rpm. The supernatant was treated with 0.22 μm syringe filter and loaded into the reverse phase chromatography SOURCE 30 RPC column. Aβ_{40} peptide was eluted with a gradient from 20% to 60% of buffer B in 10-15 column volume (CV), in which contained 80% acetonitrile (ACN) and 0.3% trifluoroacetic acid (TFA). The pure elution Aβ_{40} peptide was lyophilized and stored in −80 °C fridge.

The above purified and lyophilized Aβ_{40} peptide was dissolved into 10 mM NaOH solution. Subsequently, the dissolved peptide solution was centrifuged at 13,000 rpm for 10 minutes to remove any potential aggregates and diluted with 50 mM phosphate buffer (containing 50 mM NaCl, 0.1% NaN$_3$) to adjust the pH to 7.4, finally a concentration of 50 μM monomeric Aβ_{40}

peptide was yielded. The concentration of peptide was determined by ultraviolet-visible (UV-vis) absorption with the extinction coefficient of 1490 $M^{-1} \cdot cm^{-1}$ at 280 nm wavelength measured in water. Data were recorded on a NanoDrop 2000 spectrophotometer (Thermo Fisher Scientific). Fibrils were grown in 37 °C incubator with agitation for two weeks.

2.1.2 Solid-state NMR Titration

The bithiazole-like molecule is very hydrophobic and can only be solubilized in aqueous buffer in the nanomolar range. Therefore, we cannot simply titrate this small molecule to $A\beta_{40}$ fibrils directly. The problem has been solved by using bovine serum albumin (BSA) as a carrier to transfer bithiazole-like molecule from the BSA carrier to the amyloid fibrillar aggregates. First, the bithiazole-like molecule was dissolved in phosphate buffer (50 mM sodium phosphate, 50 mM NaCl, pH 7.4) which contains 25% (v/v) dimethyl sulfoxide (DMSO). Afterwards, BSA was added to the above solution. Under these conditions, the small molecule is quantitatively bound to BSA. The solution was then dialyzed to remove DMSO by using an ultra-centrifugal filter unit with 30 kDa cut-off membrane. Finally, the BSA trapped bithiazole-like molecule were added to the pre-formed $A\beta_{40}$ fibrils.
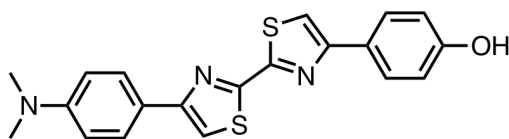
Figure 12: Structure of bithiazole-like molecule.

Bithiazole-like compound (**Figure 12**) powder has a yellow color (UV absorption at 410-420 nm wavelength). The small molecule can be easily dissolved in organic solvent such as DMSO and ACN. Based on the color change of BSA solution, we conclude that the bithiazole-like molecule is bound to BSA. After five times repetition of the washing step with phosphate buffer, the retentate in the Amicon ultra-centrifugal filter unit didn't yield an absorbance at 410-420 nm wavelength. At the same time, DMSO was also removed from the above system. The pre-formed fibrils were added to the above BSA bound molecules solution afterwards. After centrifugation, the supernatant did not yield any absorbance at 410-420 nm. After titration of bithiazole-like molecule to $A\beta_{40}$ fibrils, a color change of $A\beta_{40}$ fibrils from white to yellow was observed, suggesting that the bithiazole-like molecule was successfully titrated from BSA carrier to $A\beta_{40}$ fibrils.

2.1.3   Solid-state NMR Experiments

Uniformly labeled $A\beta_{40}$ peptide was produced by expression in *E. coli* system described above, the only difference was the minimal medium supplemented with $^{15}NH_4Cl$ and ^{13}C-glucose. [U-^{13}C, ^{15}N] labeled $A\beta_{40}$ fibrils were collected by centrifugation and packed into a 3.2 mm MAS solid-state NMR rotor. Typically, ~10 mg of $A\beta_{40}$ peptide was employed for one sample. The 2D/3D experiments were carried out on a narrow bore Bruker Avance III 750 MHz spectrometer, equipped with a triple-resonance (^1H, ^{13}C, ^{15}N) MAS probe. In all experiments, the MAS rotation frequency was adjusted to 10 kHz at 273 K. High-power proton decoupling ($\omega rf = 71$ kHz) was applied during acquisition using SPINAL-64. For ^1H, ^{13}C magnetization transfer, CP was employed. ^{13}C, ^{13}C transfers were achieved via PDSD using a mixing time of 50 ms. In the 2D/3D assignment experiments, such as NCA/NCO, NCACX and NCOCX, the selective polarization transfer between ^{13}C and ^{15}N was set up through SPECIFIC CP. All spectra were processed using TopSpin 3.5 and CCPNmr 2.3.[127]

Triple labeled $A\beta_{40}$ peptide was produced by expression in *E. coli* system, the difference was the medium using D_2O instead of H_2O and glucose-$^{13}C_6$,1,2,3,4,5,6,6-d7 instead of glucose-$^{13}C_6$. Tripled labeled $A\beta_{40}$ fibrils were collected by centrifugation and packed into a 1.3 mm MAS solid-state NMR rotor. Typically, ~2 mg of $A\beta_{40}$ peptide was employed for one sample. The 2D spectra were recorded on a wide bore Bruker Avance I 500 MHz spectrometer and a wide bore Bruker Avance III 800 MHz spectrometer, both equipped with a triple-resonance (^1H, ^{13}C, ^{15}N) MAS probe.

In all experiments for the deuterated sample, the MAS rotation frequency was adjusted to 52 kHz. The effective sample temperature was kept constant around 15 °C. In the proton detected CP-based HSQC experiment, the 90° pulses were set to 1.55 μs at 161 kHz rf-field amplitude for ^1H and 5.0 μs at 50 kHz rf-field amplitude for ^{15}N. ^1H–^{15}N CP was achieved using a contact time of 0.6 ms. WALTZ-16 was applied for ^{15}N decoupling during ^1H acquisition. For the 3D assignment experiments, the 90° pulses were set to 3.2 μs at 78 kHz rf-field amplitude for ^{13}C and 5.0 μs at 50 kHz rf-field amplitude for ^{15}N. The initial CP sequence from H to Cα/CO had a contact time of 3.5 ms and a constant-amplitude ^{13}C spin lock of 14 kHz. Both CO–N and Cα–N CP steps had a contact time of 8 ms with a constant-amplitude spin lock of about 33 kHz on ^{13}C and a tangent-

modulated amplitude spin lock of mean rf-field amplitude of about 25 kHz on ^{15}N. Data were acquired in the States-TPPI mode in the indirect dimension. The last magnification transfer step in all pulse sequences were designed with optimal control method to yield higher sensitivity.

2.2 Cross-amyloid Interaction Surface Mimics

2.2.1 Sample Preparation

The ISM peptide inhibitor was chemically synthesized by Fmoc solid-phase synthetic protocols, purified by reverse-phase HPLC and provided as a film evaporated from hexafluoroisopropanol (HFIP) in an Eppendorf tube. The R3-GI peptide was dissolved in 10 mM sodium phosphate buffer, pH 7.5 (containing 1% v/v HFIP), to a final concentration of 1.5 mM. The other peptide inhibitors were prepared in the similar way. The final concentration of R3-G, R3-I and R3 was 1 mM respectively, and the G3-GI was 0.5 mM.

2.2.2 Solution-state NMR Experiments

2.2.2.1 Nuclear Overhauser Effect Spectroscopy

Nuclear overhauser effect (NOE) is a phenomenon caused by the relaxation process of the nuclear spin system and refers the dipole-dipole interactions through space. Dipole-dipole interactions, internal molecular motion and chemical exchange are able to induce cross-relaxation between nuclear spins, further causing NOE. For protein molecules, if the distance between protons is less than or equal to 5 Å, the NOE signal can be observed in the NMR spectrum, and the intensity of NOE signal is inversely proportional to the 6th power of the proton distance. The strength of the NOE signal provides the distance information of protein molecules. In general, the NOESY spectrum is used to gather all the spatial information of protons, further to encode the three-dimensional arrangement of all the atoms and the structure of a protein.

In order to collect the distance information of nuclear spins, all 1D ^{1}H spectrum and 2D ^{1}H–^{1}H NOESY spectrum were recorded on a Bruker Avance III 900 MHz spectrometer, equipped with a triple resonance cryo-probe, setting the temperature to 277 K. In all experiments, a NOESY mixing time of 300 ms was employed. The experiments data were processed with TopSpin 3.5 and analyzed with CCPNmr 2.3.[128]

2.2.2.2 Diffusion Ordered Spectroscopy

Diffusion is the random movement of molecules and is defined by the Stokes-Einstein equation. Diffusion coefficient is dependent on parameters such as the shape and size of the molecules, temperature and dynamic viscosity.

$$D = \frac{k_B T}{6 \pi \eta R}$$

D: diffusion coefficient

k_B: Boltzmann's constant

T: absolute temperature

η: viscosity

R: hydrodynamic radius

Diffusion ordered spectroscopy (DOSY) is applied to determine the diffusion coefficient by recording a series of 1D DOSY spectra. Here, different field gradient strength ranged from 2% gradient to 90% gradient in 11 steps. The coefficient D was obtained by analyzing the intensity of the echo versus the different gradients. The DOSY experiments were performed on a Bruker Avance III 500 MHz spectrometer equipped with a cryogenic probe. A set of diffusion spectra were recorded with gradient (along z axis) strength varying from 1.07 to 48.15 G/cm at 277 K, 283 K and 293 K, respectively. The sine shaped gradient pulses each had a duration of 1600 μs. The diffusion interval was set to 0.23 s. The DOSY data were fitted using the equation[129–131] below:

$$\ln \frac{I}{I_0} = -\gamma^2 \delta^2 G^2 D \left[\Delta + \left(\frac{4\delta}{3} + \frac{3\tau}{2} \right) \right]$$

I: intensity

I_0: intensity at 2% gradient value

γ: gyromagnetic ratio for proton

δ: length of the gradient pulse

G: gradient strength

D: diffusion coefficient

Δ: diffusion delay

τ: gradient ringdown delay

2.2.2.3 Saturation Transfer Difference

Saturation transfer difference (STD) experiment is typically used to characterize the protein-ligand binding interactions in solution, on the basis of the exchangeable process between bound ligand and free ligand in the system.[132–135] Generally, protein is selectively saturated to obtain the on-resonance spectrum by irradiating at a region that only protein can be detected. The off-resonance spectrum is recorded without protein saturation. The STD signals refer to the binding ligand which could receive the signal from the saturation transfer of protein. One application of STD experiment is to monitor the monomer/oligomer equilibrium by saturated monomer signals.

STD NMR experiments of 1.25 mM R3-GI in 10 mM Na-phosphate, pH 7.4 containing 1% HFIP and 10% D_2O were carried out on a Bruker Avance III 600 MHz spectrometer equipped with a cryogenic probe at 283 K, 298 K and 308 K, respectively. 1D proton experiments were performed using a WATERGATE pulse sequence with 32 k time domain points and 128 scans. STD spectra were recorded using an interleaved pulse program with on- and off-resonance irradiation. Saturation was achieved by a chain of Gaussian-shaped pulses of 49 ms each, with on-resonance saturation at −1 ppm and off-resonance at −100 ppm with 2 seconds total saturation time, using 2048 scans and 32 k time domain points. Spectra were processed by using TopSpin 3.5.

2.3 Supporting Experiments

2.3.1 Transmission Electron Microscopy

The pre-formed $Aβ_{40}$ fibrillar aggregates sample was washed several times with distilled water before capturing the transmission electron microscopy (TEM) images. Due to the fibrillar aggregates were prepared in phosphate buffer, the residual contaminations from salt need to be removed by washing the fibrils.

1. Glow discharge the copper grid to make the carbon film generating a hydrophilic surface.

2. Place 10 μL of fibrillar aggregates sample on the discharging grid.

3. Gently dry the grid with filter paper.

4. Add 10 μL of 2% uranyl acetate solution on the dry grid. The fibrillar aggregates can be differentiated from the background by 30 seconds of staining.

5. Dry the grid as above and put it into the microscopy to capture images.

2.3.2 Differential Interference Contrast Microscopy

Differential interference contrast microscopy (DIC) is a technique used to enhance the contrast in un-stained and transparent samples. All of the images were captured from Leica Microsystems.

1. Switch on the microscope. After initialization, set up the microscope via the touch screen.

2. Sample preparation and set up basic parameters including image format, exposure time, magnification and filter cube with excitation and emission filters. Then capture the images with DIC normal mode and fluorescence filter mode, respectively.

3. Remove the sample from the plate, wash the plate surface with buffer, then add buffer on the plate surface to capture images which show the structures absorbed on the plate surface.

2.3.3 Dynamic Light Scattering

Dynamic light scattering (DLS) is a technique to determine the protein aggregation state by detecting the molecular weight and size distribution. *The basic principle is simple: the sample is illuminated by a laser beam and the fluctuations of the scattered light are detected at a known scattering angle θ by a fast photon detector*.[136]

1. Switch on the DLS instrument and set up temperature unit. Then start the software.

2. Filter or centrifuge the peptide sample to remove unwanted particles. Load 60 μL of peptide sample free of bubbles into the cuvette.

3. Set up the acquisition time and laser power, run a DLS measurement.

4. Data analysis.

Formulations for Medium

Luria Broth medium (1 L)

Tryptone	10 g
Yeast extract	5 g
NaCl	5 g

M9 medium (1x 1 L)

100 mL	10x M9
10 mL	trace elements (100x)
1 mL	1 M $MgSO_4$
0.3 mL	1M $CaCl_2$
1.5 mL	1 mg/mL thiamin-HCl
15 mL	0.1 mg/mL biotin
2 g	glucose
1 g	NH_4Cl
1 mL	antibiotic

Stock solution for M9 medium

10x M9 1 L

60 g	Na_2HPO_4
30 g	KH_2PO_4
5 g	NaCl

Trace elements 100x 1 L

5g	EDTA
0.83 g	$FeCl_3 \cdot 6H_2O$
84 mg	$ZnCl_2$
13 mg	$CuCl_2 \cdot 2H_2O$
10 mg	$CoCl_2 \cdot 6H_2O$
10 mg	H_3BO_3
1.6 mg	$MnCl_2 \cdot 4H_2O$

Table 6: List of chemicals.

Chemicals	Purity	Commercial Source
Acetonitrile, CH_3CN	HPLC grade	VWR
Acrylamide/Bis solution, 29:1	BioReagent	Crescent Chemical
Agarose	BioReagent	Sigma-Aldrich
Albumin, bovine serum	≥ 99%	Merck
Ammonium chloride, NH_4Cl	≥ 99.5%, ACS	Carl-Roth
Ammonium-^{15}N chloride, $^{15}NH_4Cl$	^{15}N, ≥ 99%, CP	Sigma-Aldrich
Ammonium persulfate, $(NH_4)_2S_2O_8$	≥ 98%	Sigma-Aldrich
Ammonia solution 30%, $NH_3 • H_2O$	ACS grade	Carl-Roth
Biotin	Research grade	Crescent Chemical
Boric acid, H_3BO_3	≥ 99.8%, ACS	Carl-Roth
Calcium chloride dihydrate, $CaCl_2 • 2H_2O$	≥ 99%, ACS	Carl-Roth
Cobalt (II) chloride hexahydrate, $CoCl_2 • 6H_2O$	≥ 99%, ACS	Carl-Roth
Coomassie blue G 250	For electrophoresis	Crescent Chemical
Copper (II) chloride dihydrate, $CuCl_2 • 2H_2O$	≥ 99%	Carl-Roth
D (+)-Glucose Monohydrate, $C_6H_{12}O_6 • H_2O$	≥ 99.5%	Carl-Roth
D-Glucose-$^{13}C_6$	^{13}C, ≥ 99%, CP	Sigma-Aldrich
D-Glucose-$^{13}C_6$, 1,2,3,4,5,6,6-d_7	97% D, 99% ^{13}C	Sigma-Aldrich
Dimethyl sulfoxide, $(CH_3)_2SO$	≥ 99.9%	Sigma-Aldrich
Disodium hydrogen phosphate, Na_2HPO_4	≥ 99.5%	Carl-Roth
EDTA	≥ 99%, ACS	Carl-Roth
Ethanol absolute ≥99.7%, CH_3CH_2OH	HPLC grade	VWR
Guanidine hydrochloride, $CH_5N_3 • HCl$	≥ 99.7%	Carl-Roth
Hydrochloric acid fuming 37%, HCl	Reagent grade	VWR
Iron (III) chloride hexahydrate, $FeCl_3 • 6H_2O$	≥ 97%, ACS	Carl-Roth
Isopropyl-β-D-thiogalactopyranoside, IPTG	Research grade	Crescent Chemical
Kanamycin sulfate	≥ 750 I.U./mg	Carl-Roth
Manganese (II) chloride tetrahydrate, $MnCl_2•4H_2O$	≥ 99%	Carl-Roth
Magnesium sulfate, $MgSO_4$	≥ 99%	Carl-Roth
Potassium dihydrogen phosphate, KH_2PO_4	≥ 99%, ACS	Carl-Roth

Continued:

Chemicals	Purity	Commercial Source
Protease inhibitor cocktail	BioReagent	Roche
Sodium azide, NaN_3	≥ 99%	Carl-Roth
Sodium chloride, NaCl	≥ 99.5%, ACS	Carl-Roth
Sodium dodecyl sulfate, $CH_3(CH_2)_{11}SO_4Na$	Research grade	Crescent Chemical
Sodium hydroxide, NaOH	≥ 99%	Carl-Roth
TEMED	≥ 99%	Carl-Roth
Thiamine hydrochloride	≥ 98.5%	Carl-Roth
Tricine, $(HOCH_2)_3CNHCH_2CO_2H$	≥ 99%	Carl-Roth
Trifluoroacetic acid, CF_3CO_2H	≥ 99.9%	Carl-Roth
Tris, $(HOCH_2)_3CNH_2$	≥ 99%, USP	Carl-Roth
Tryptone	For microbiology	Carl-Roth
Urea, $CO(NH_2)_2$	Reagent grade	VWR
Yeast extract	For microbiology	Carl-Roth
Zinc chloride, $ZnCl_2$	≥ 97%	Carl-Roth

Chapter 3

NMR Structural Characterization of

ISMs Peptide Inhibitors

3 NMR Structural Characterization of ISMs Peptide Inhibitors

3.1 *N*-methylation Modification of ISMs Peptides

One of the methods to improve the properties of peptide drug candidates is to utilize *N*-methylation modification.[137,138] *N*-methylation has effects on the *cis-trans* conformation equilibrium of *N*-methylated amide bond, favoring the *cis* configuration owing to the increasing steric hindrance. In addition, *N*-methylation modification enables to eliminate the hydrogen bond formation, thus leading to the conformational change. Apart from the prevention of hydrogen bonds formation, the steric interactions between the *N*-methyl group and the side chains of amino acids may induce the stereostructural change of the adjacent amino acids, thus introducing conformational rigidity further to influence the protein conformation.[137,138]

As mentioned in Chapter 1, the two segments from IAPP sequence including Ala8-His18 and Asn22-Ser28 are termed as the two hot segments for both IAPP self-interaction and cross-interaction with Aβ. The *N*-methylation modification at residue Gly24 and residue Ile26 which are located at the same side of β-strand in the amyloid core, is able to prevent the hydrogen bonds formation in the inter-molecular backbone NH to CO, further to avoid the self-aggregation. By using the hot-segment-linking approach, a series of highly soluble, non-amyloidogenic and non-cytotoxic inhibitors are generated to block the aggregation of both IAPP and Aβ.[85,90] Generally, the linker region consists of three amino acids and determines the structure and properties of ISMs peptide inhibitors.

3.2 Aim

In the work discussed here, several ISMs peptides[1] were included such as R3-GI, R3-G, R3-I, R3, and G3-GI. We focused on the structural characterization of the double *N*-methylated R3-GI peptide on the basis of two hot regions of IAPP linking with three charged amino acid arginine (sequence is shown in **Figure 25**). R3-GI peptide, as a selective inhibitor for Aβ$_{40}$, is able to block toxicity and induce the amorphous aggregates formation.[85] Our research target is to determine the structure of the R3-GI peptide by using solution-state NMR and molecular dynamics (MD) simulation, in combination with other biophysical and biochemical techniques. The substrate

---

[1] ISMs peptides described in Chapter 3 were provided by Prof. Dr. Aphrodite Kapurniotu.

interactions of different ISMs with $A\beta_{40}$ peptide were also conducted by solution-state NMR and fluorescence microscopy to gain insights into the potential inhibition mechanism of ISM inhibitors. In addition, the study on G3-GI peptide was carried out to investigate the inhibitory function and structural differences induced by a different linker of ISM. Meanwhile, in order to analyze the effects of *N*-methylation modification on ISMs conformational change, NOESY spectra of mono-methylated and non-methylated ISMs were recorded and compared with double *N*-methylated R3-GI peptide.

3.3 Sequential Assignment for R3-GI Peptide

For the preliminary characterization, one-dimensional NMR experiment of the R3-GI peptide was acquired at 277 K by using a Bruker Avance III 900 MHz spectrometer (**Figure 13**). High resolution solution-state NMR spectra were obtained at the concentration in the millimolar range. The relatively narrow chemical shifts dispersion suggests that R3-GI peptide is unfolded or disordered peptide with random coil secondary structure, where the well-dispersed resonances were detected, including methyl-group proton resonances, downfield-shifted α proton, β proton resonances, aromatic proton resonances and amide proton resonances.
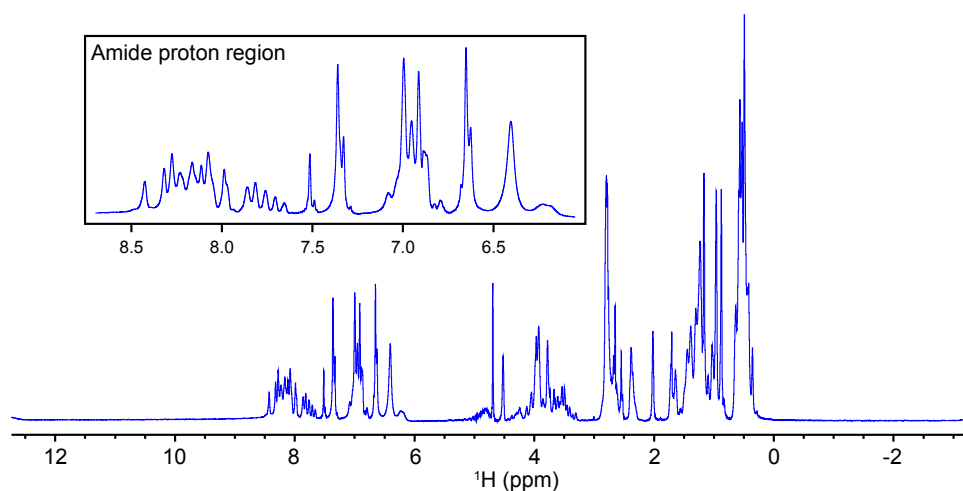
Figure 13: 1D ^{1}H spectrum of 0.5 mM R3-GI peptide with high-resolution was recorded at 277 K using a Bruker Avance III 900 MHz spectrometer. Top left: zoom of the amide proton region from the 1D spectrum.

With the cross peaks formed by the correlation between $^NH_{i+1}$ resonance and $^\alpha H_i$ resonance, the sequential resonance assignment for the R3-GI peptide from 2D NOESY spectrum is plotted in

Figure 14 bottom. Due to the *N*-methylation modification, two sets of chemical shifts were assigned for segment Phe8-His11 at N-terminus and segment Asn15-Leu20 at the C-terminus. Several intense long-range NOE contacts (**Figure 14**, top) were detected in both conformers which indicates a loop-like structure formation induced by the arginine linker segment. In addition, a *cis* peptide conformer occurs[139,140] resulting in four different sets of resonances in *N*-methyl regions of the R3-GI peptide, and they are Gly17*trans*/Ile19*trans*, Gly17*trans*/Ile19*cis*, Gly17*cis*/Ile19*trans* and Gly17*cis*/Ile19*cis*. However, the signal intensity for Gly17*cis*/Ile19*cis* conformer was too weak to be observed in solution-state NMR experiments. The population of Gly17*trans*/Ile19*trans*, Gly17*cis*/Ile19*trans* and Gly17*trans*/Ile19*cis* conformers were on the order of 64%, 32% and 4%, respectively. It's worth noting that the low pH conditions have no impact on the population distribution of the conformers (**Figure 15**).
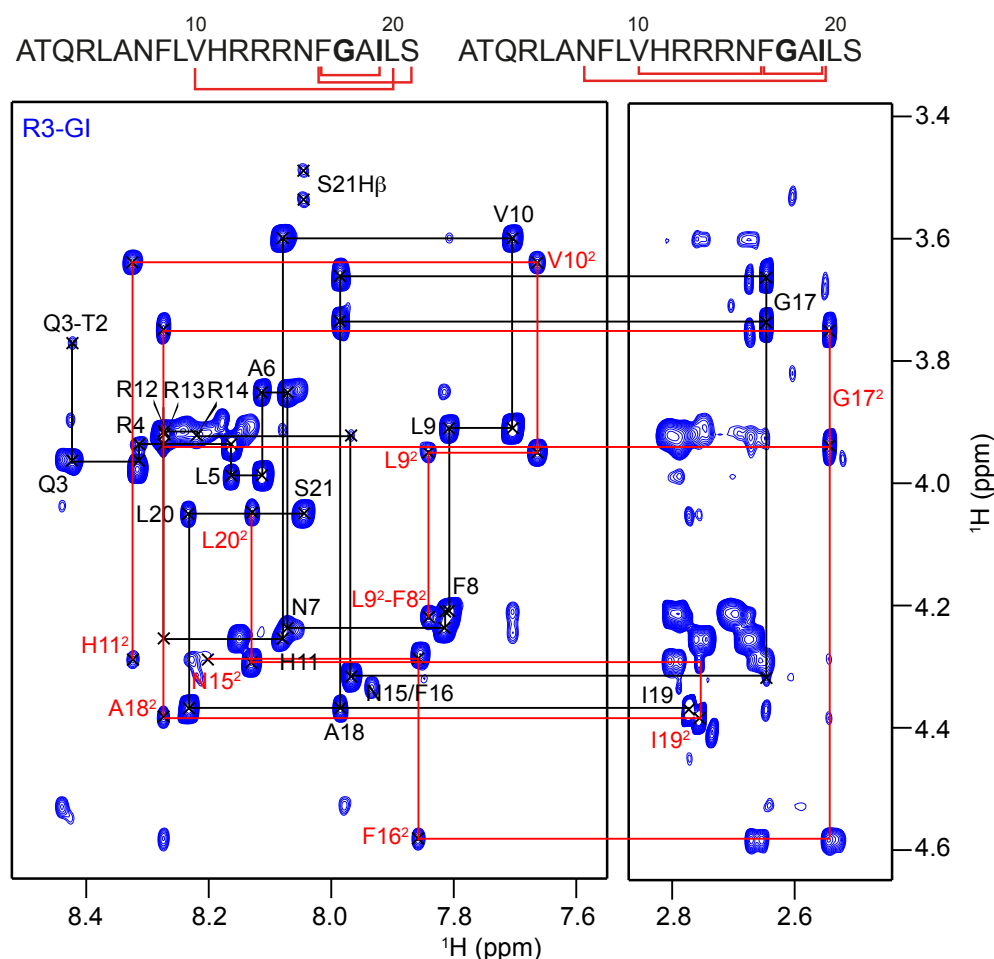
Figure 14: Top, long-distance NOE contacts are plotted onto the R3-GI peptide sequence. Bottom, sequential resonance assignment of 1.5 mM R3-GI peptide in amide proton and alpha proton region. 2D $^1H-^1H$ NOESY spectrum was recorded at 277 K using a Bruker Avance III 900 MHz spectrometer with 300 ms mixing time. The sequential walk for the second conformer is labeled in red color.
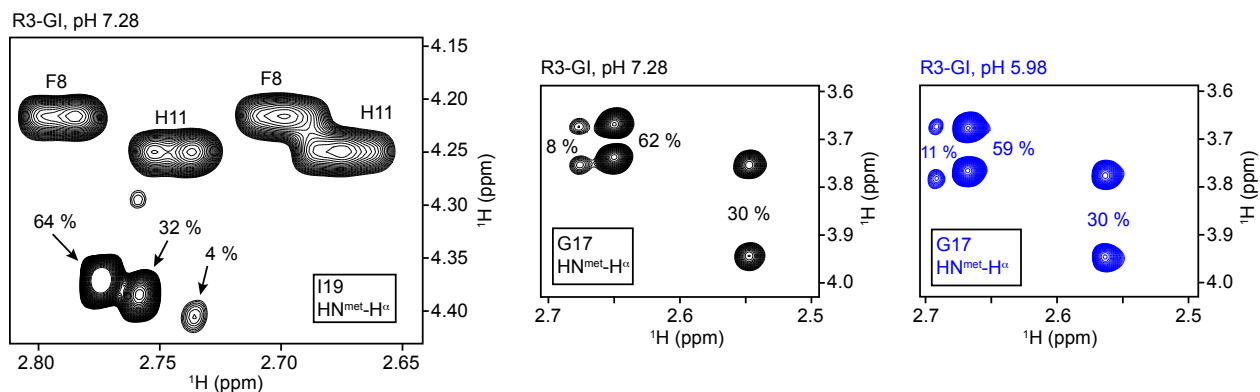
Figure 15: Cis-trans isomers induced by N-methylation at residue Gly17 and residue Ile19 of R3-GI peptide. 2D ^{1}H–^{1}H NOESY spectrum in the Gly17 region at a low pH condition is labeled in blue color.

3.4 Temperature and pH dependence of NOE Contacts

NOE is generally considered as one of the keys to disclose information between protons that are spatial close less than 5 Å. Many intense long-range NOE contacts in the R3-GI peptide were observed in 2D ^{1}H–^{1}H NOESY spectrum indicating that R3-GI peptide was not completely random coil conformation. Less and weak NOE contacts were detected in the G3-GI peptide, which implies that the loop structure in the G3-GI peptide is less stable in comparison to the R3-GI peptide. We hypothesize that the loop-like structure is crucial for the ISM peptide inhibitory property. That's the reason why G3-GI peptide is not an active inhibitor for Aβ. In contrast, no NOE contacts can be observed in the non-*N*-methylated R3 peptide, suggesting that the R3 peptide adopts the random coil structure. In addition, only one set of chemical shifts is assigned for R3 peptide which confirms there is only one conformation presence in R3 peptide.

Furthermore, the salt and pH dependence for the loop-like structure formation for R3-GI peptide were investigated by solution-state NMR. The intensity of long-distance NOE (Asn7-Ile19)[2] contact does not show much difference at different sodium chloride concentration with reference of the peak intensity of (Leu20-Ile19)[2] in conformer 2 (**Figure 16**). Whereas the low pH condition significantly increases the intensity of the long-range cross peaks (**Figure 17**). Similarly, the low temperature condition increases the fraction of peptides that adopt the turn-like structure (**Figure 18**).

Additionally, it seems that the cross peak intensity of (Asn7-Ile19)[2] correlates with the pKa of the imidazole ring of histidine. A lower pH condition and protonation of the histidine side chain is

able to facilitate the loop structure formation in the aggregated state of R3-GI peptide. In order to determine the pKa value of His11 imidazole side chain in R3-GI peptide, NMR experiments were carried out to obtain the CS of residue His11 Hδ2 at different pH conditions. The 1D spectra at different pH conditions are shown in **Figure 19**. With the chemical shift assignment of Hδ2, non-linear curve fitting with Dose Response fitting function was used to calculate the pKa value of His11. The DoseResp function is shown below:

$$y = A1 + \frac{A2 - A1}{1 + 10^{(Logx0 - x)p}}$$
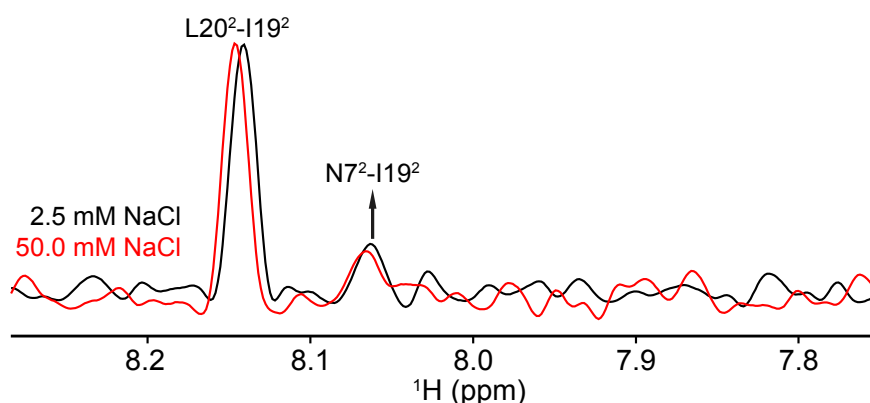
Figure 16: *Asn7-Ile19 peak intensity comparison for 0.5 mM R3-GI peptide at different salt conditions. Different 1D slices were extracted from 2D NOESY spectrum at the corresponding salt condition. 2D $^1H-^1H$ NOESY spectra were recorded at 277 K using a Bruker Avance III 900 MHz spectrometer with 300 ms mixing time.*
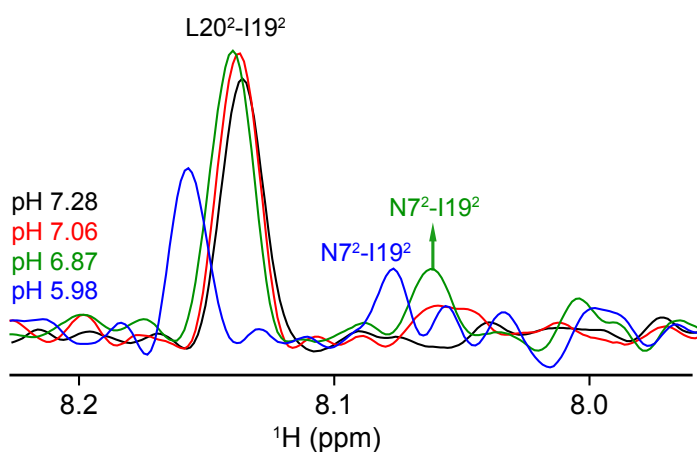
Figure 17: *Asn7-Ile19 peak intensity comparison for 0.5 mM R3-GI peptide at different pH conditions. Different 1D slices were extracted from 2D NOESY spectrum at the corresponding pH condition.*
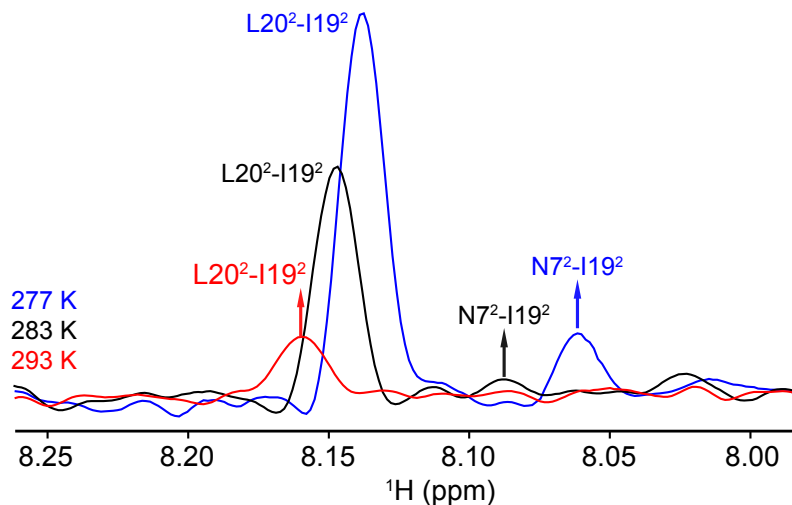
Figure 18: Asn7-Ile19 peak intensity comparison for 1.5 mM R3-GI peptide at different temperatures. Different 1D slices were extracted from 2D NOESY spectrum at the corresponding temperature condition. 2D ^1H–^1H NOESY spectra were recorded using a Bruker Avance III 900 MHz spectrometer with 300 ms mixing time.
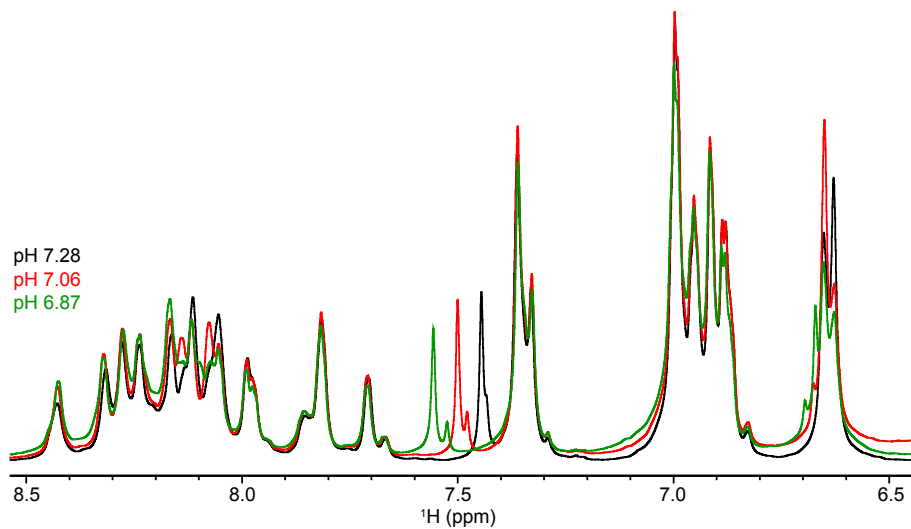
Figure 19: Superposition of 1D ^1H spectra in aromatic and amide proton region for 0.5 mM R3-GI peptide at different pH conditions. All of the experiments were recorded at 277 K using a Bruker Avance III 900 MHz spectrometer.
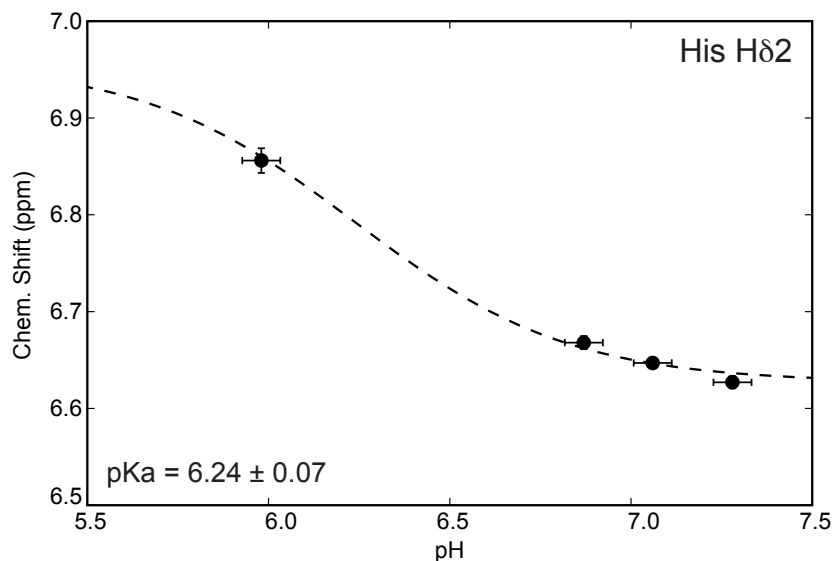
Figure 20: Non-linear fitting for pKa value calculation for His11 imidazole side chain based on the CS of Hδ2 at different pH conditions. The chemical shift difference of 0.33 ppm is obtained from histidine at acid and conjugate base forms.[141]

3.5 Exchange between Monomeric and Oligomeric State

We hypothesize that there might be higher molecular weight structures formed in the R3-GI peptide on the basis of the intense NOE contacts. Higher molecular weight species were visualized in DIC and TEM images shown in **Figure 21**. The droplet-like structures with high molecular weight were captured in both DIC mode and fluorescence mode. As a supplement, TEM images of the R3-GI peptide revealed spheroidal aggregates with diameters in the range of 100-200 nm. DLS measurement also confirmed the presence of the oligomeric state of the R3-GI peptide. According to the DLS result, two well-resolved species were observed in the R3-GI peptide, and the hydrodynamic radius of the monomeric state R3-GI peptide was around 2.7 nm. The hydrodynamic ratio from DLS is compatible with the DOSY experiment from solution-state NMR, in which the hydrodynamic ratio R_H of R3-GI peptide was calculated on the basis of the Stokes-Einstein equation with the order of around 18 Å. The diffusion coefficients at different temperatures from DOSY experiments are listed in **Table 7**. The details for the above techniques are written in Chapter 2.
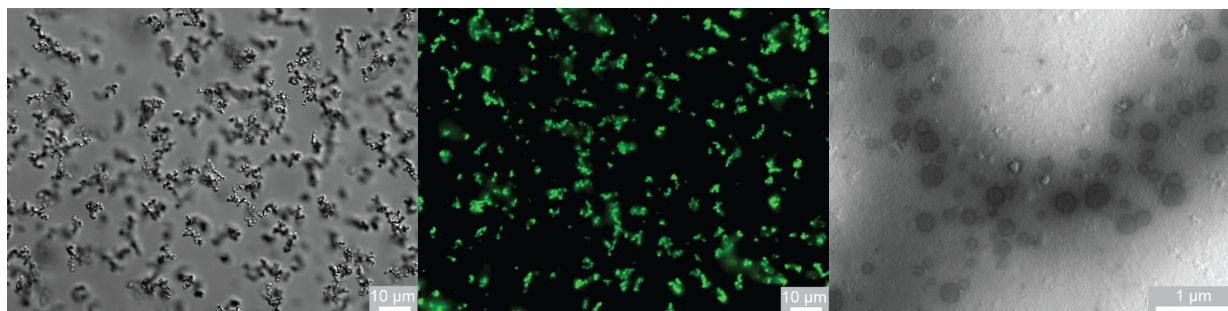
Figure 21: DIC image of Fluos-R3GI peptide(left), microscopic image in fluorescence mode (middle), TEM image of R3-GI peptide (right). The peptide has been imaged immediately after dissolution into buffer without filtration by using DIC normal and fluorescence mode.
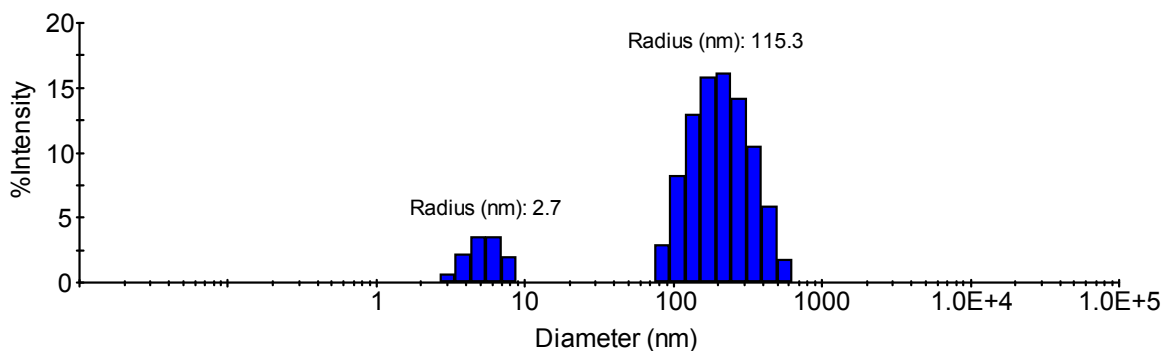
Figure 22: DLS size distribution of 50 μM R3-GI peptide in phosphate buffer with 1% (v/v) HFIP.
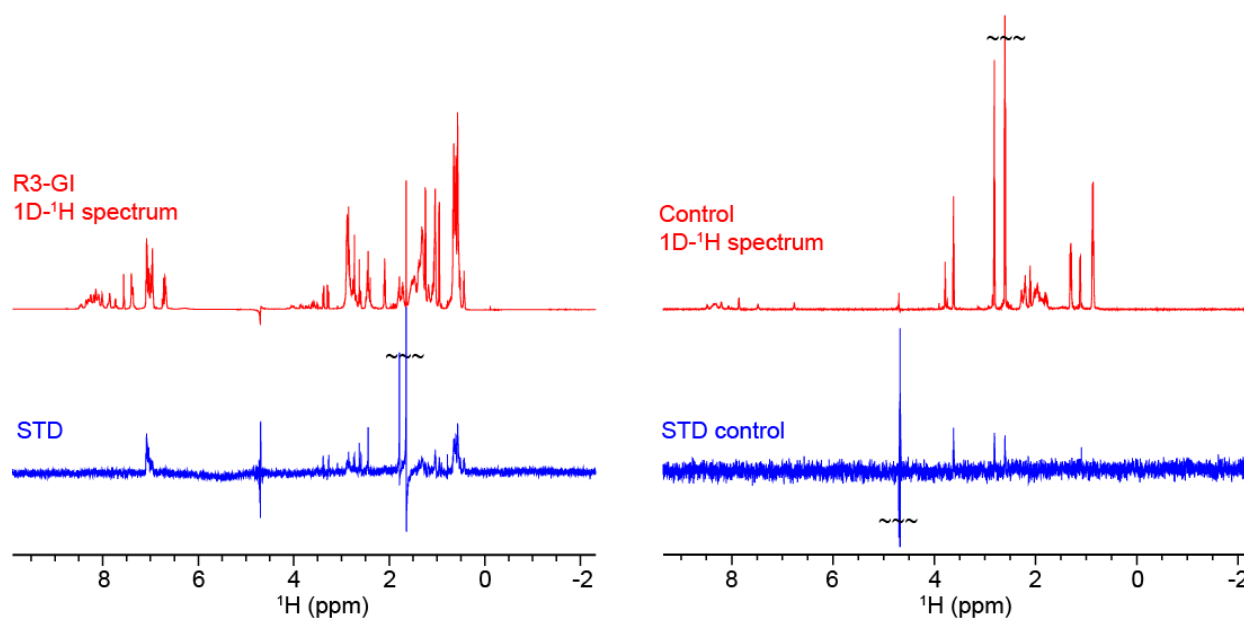
Figure 23: STD experiments for 1.25 mM R3-GI peptide (left) and 60 μM negative control peptide (right) with the sequence of GVAEPEQDCAVTSGE and 1.492 kDa molecular weight.

In contrast, the high-resolution and narrow dispersion solution-state NMR spectra are typical for random coil monomeric R3-GI peptide. In order to resolve this apparent discrepancy among different methods, saturation transfer difference (STD) experiments was carried out to detect the chemical exchange process for R3-GI peptide. High STD signal intensity was observed in this experiment, suggesting that the R3-GI peptide undergoes chemical exchange between a monomeric random-coil like conformation, and an aggregated state that was too large to be observable for solution-state NMR. As a negative control sample, STD spectrum of a small peptide was recorded with the identical acquisition parameters, which did not aggregate and yielded no STD signals. The weak STD signals were generated as the artifact from the organic solvent 2-mercaptoethanol in the negative control small peptide.

Further to confirm the chemical exchange process between monomeric state R3-GI and oligomeric state R3-GI, the diffusion ordered spectroscopy was conducted with an internal NMR standard, 4,4-dimethyl-4-silapentane-1-sulfonic acid (DSS). As a reference control, a 7.3 kDa globular protein, the α-spectrin SH3 domain was used to compare the diffusion data with the R3-GI peptide. The diffusion coefficient of the R3-GI peptide is slightly larger than expected for a 21-residue random coil peptide. At a temperature of 4 °C, the diffusion coefficient of R3-GI (listed in **Table 7**) is approximately 1.3 times smaller in comparison with α-SH3, even though the hydrodynamic radius of the globular protein is expected to be smaller. A smaller, apparent diffusion coefficient is expected if R3-GI undergoes exchange between a monomeric and an aggregated state.
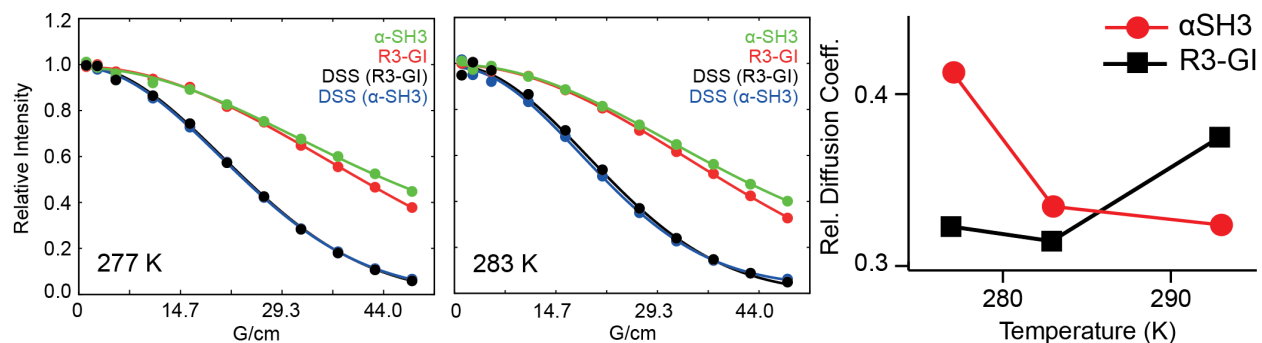
Figure 24: Temperature dependent DOSY experiments were performed for R3-GI peptide by using a Bruker Avance III 500 MHz spectrometer, including 277 K, 283 K and 293 K. The gradient strength was set up from 2% to 90% in 11 steps. α-spectrin SH3 domain has been measured for reference. DSS was used as internal NMR standard.

Table 7: Diffusion coefficients from DOSY experiments at different temperatures.

	273 K	283 K	293 K
R3-GI	$2.21\ e^{-10} \pm 7.19\ e^{-13}$	$2.50\ e^{-10} \pm 8.45\ e^{-13}$	$4.03\ e^{-10} \pm 8.87\ e^{-13}$
α-SH3	$2.88\ e^{-10} \pm 2.21\ e^{-12}$	$2.95\ e^{-10} \pm 2.37\ e^{-12}$	$3.92\ e^{-10} \pm 2.24\ e^{-12}$
DSS (R3-GI)	$6.78\ e^{-10} \pm 9.56\ e^{-12}$	$7.87\ e^{-10} \pm 4.23\ e^{-12}$	$1.07\ e^{-9} \pm 3.20\ e^{-12}$
DSS (α-SH3)	$6.97\ e^{-10} \pm 9.14\ e^{-12}$	$8.75\ e^{-10} \pm 3.58\ e^{-12}$	$1.20\ e^{-9} \pm 1.79\ e^{-11}$

Table 8: Estimation of the partitioning coefficient of R3-GI in solution. The figures on the bottom of the table are fluorescence microscopic images of 500 µM Flous-R3GI, with picked structures (left) and background (right) high-lighted with orange lines. The scale bar in the figure denotes a length of 25 µm. Fluorescence intensity value were generated from ImageJ software for Fluos-R3GI peptide.

No.	Area	Mean Intensity for R3-GI	Mean Intensity for Background
1	0.331	12.871	6.069
2	0.107	18.174	6.382
3	0.052	9.555	2.592
4	0.068	9.245	2.6
5	0.026	10.745	3.453
6	0.243	10.244	5.538
7	0.116	11.447	3.553
8	0.065	16.453	6.346
9	0.121	13.213	3.967
10	0.068	11.561	3.414
11	0.088	15.161	6.337
12	0.068	17.433	7.796
13	0.065	12.678	3.818
14	0.087	11.027	3.773
15	0.12	11.463	3.913
16	0.25	10.637	3.012
17	0.073	11.765	3.113
18	0.232	14.222	4.993
19	0.098	8.059	3.75
20	0.258	10.513	2.722
21	0.047	12.755	4.588
22	0.041	14.773	3.55
23	0.044	10.279	3.774
24	0.211	7.974	3.374
25	0.118	13.663	4.248

Structure selected   *Background selected*
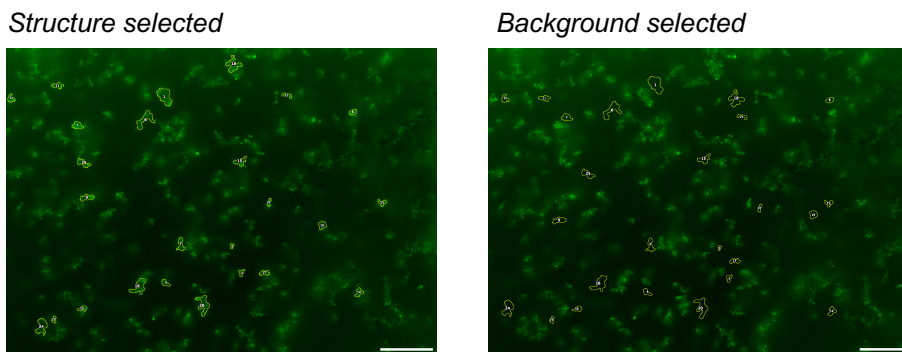
To quantify the population of the monomeric state R3-GI peptide remains in solution and the population for the oligomeric state R3-GI peptide forms the liquid droplet-like structures, fluorescence mode DIC images were captured to determine the partitioning coefficient of R3-GI. The intensities of the fluorescence mode DIC images of the aggregate structures were analyzed with the reference of the intensity for the background. The partitioning coefficient of R3-GI is on the order of 2.9. It suggests that an approximately three-fold higher concentration in the aggregates in comparison to free solution. The detailed information of the partitioning coefficient determination is shown in **Table 8**.

3.6 Inter-molecular Interactions

To confirm the presence of potential oligomers of R3-GI peptide, a mixed sample with 1:1 ratio of labeled R3-GI (R3-GI*, **Figure 25**) peptide and unlabeled R3-GI (R3-GI, **Figure 25**) peptide was prepared to obtain the information on the inter-molecular interactions. In the NOESY experiment, a filter was applied during the first evolution period t_1 to remove magnetization of protons that are directly bound to ^{13}C nuclei. After the NOESY mixing time, ^{13}C bound protons are selected for detection.

R3-GI* : R3-GI = 1:1 ^{13}C, ^{15}N labeled amino acids

$A^1T^2Q^3R^4\mathbf{L^5A^6}N^7\mathbf{F^8L^9V^{10}}H^{11}$-RRR-$N^{15}F^{16}G^{(Me)17}A^{18}I^{(Me)19}\mathbf{L^{20}S^{21}}$
+
$A^1T^2Q^3R^4L^5A^6N^7F^8L^9V^{10}H^{11}$-RRR-$N^{15}F^{16}G^{(Me)17}A^{18}I^{(Me)19}L^{20}S^{21}$
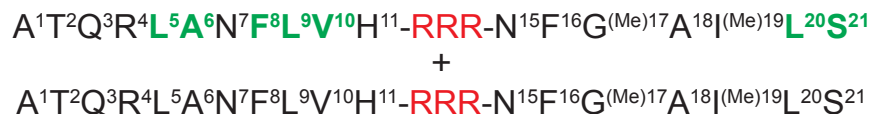
Figure 25: R3-GI peptide sequence and the labeling scheme for the filter NOESY experiment. Residues labeled in green color are uniformly enriched with ^{13}C and ^{15}N.
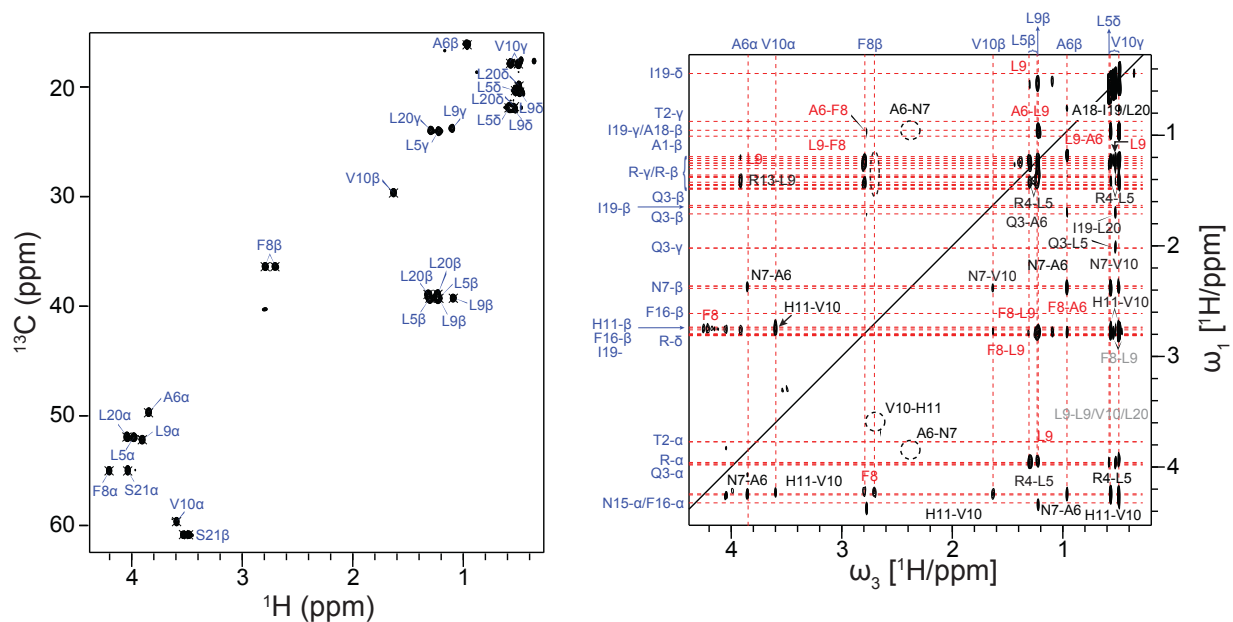
Figure 26: $^1H–^{13}C$ correlation spectrum (left) of labeled R3-GI and $^1H–^1H$ correlation spectrum (right) of the mixed R3-GI peptide sample extracted from the filtered NOESY experiment with 300 ms mixing time.

A number of sequential connectivities between labeled and non-labeled residues within one peptide were identified, like His11Hβ–Val10Hα and Asn7Hβ–Ala6Hα. These cross peaks occurred only either above or below the diagonal, indicating that filtering of magnetization works in the proposed way. In addition to these intra-molecular sequential connectivities, many correlations were observed to yield a symmetric cross peak both below and above the diagonal, such as Aal6Hβ–Leu9Hβ, Phe8Hβ–Leu9Hβ and Leu9Hβ–Leu9Hδ. These correlations must be due to the inter-molecular interactions, as they involve labeled amino acids. On the basis of the observation, the oligomer state R3-GI peptide was preliminarily identified by solution-state NMR.

3.7 Effects of *N*-methylation Modification

With *N*-methylation modification at residues Gly17 and Ile19 in the R3-GI peptide, *trans/cis* conformers were detected for both Gly17 and Ile19. To compare the effects of *N*-methylation modification on the peptide conformation, NOESY spectra were recorded for non-methylated and mono-methylated modified peptide, such as R3, R3-G and R3-I (sequential resonance assignments are shown in **Figure 27** and **Figure 28**).
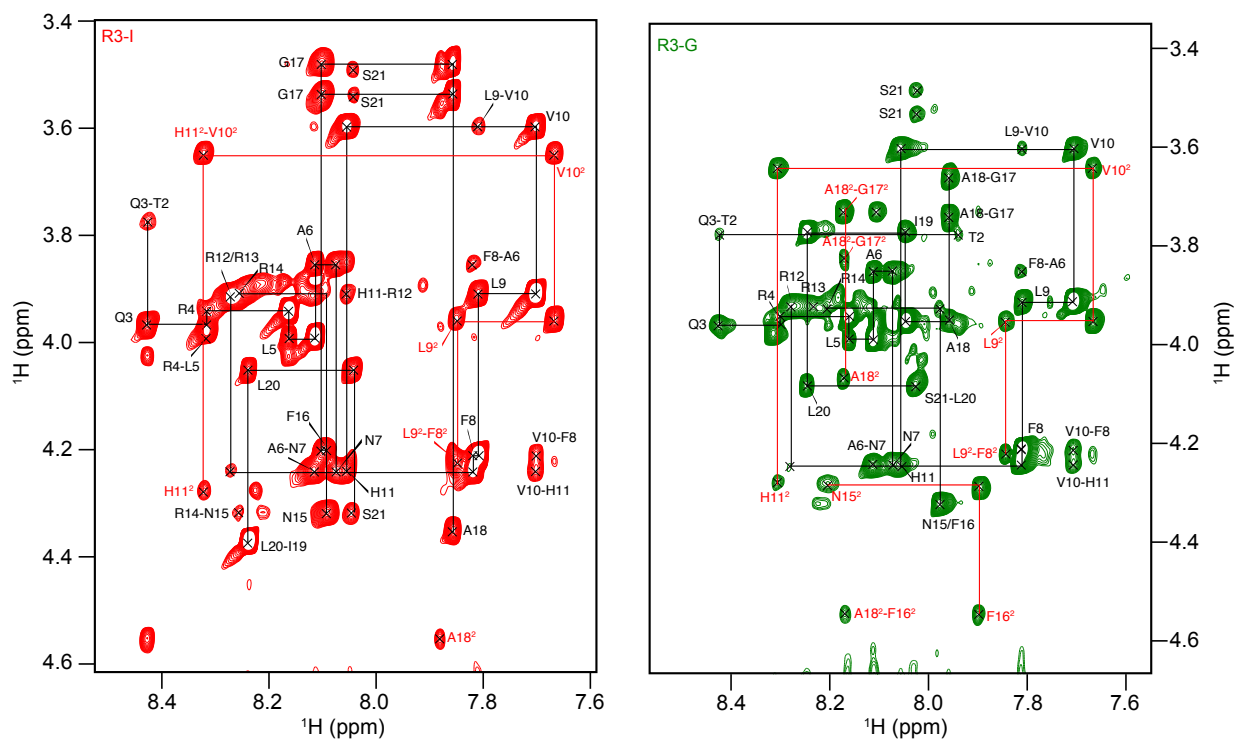
Figure 27: Sequential resonance assignment of 1.0 mM R3-I peptide (left, peaks are labeled with red color) and 1.0 mM R3-G peptide (right, peaks are labeled with green color).
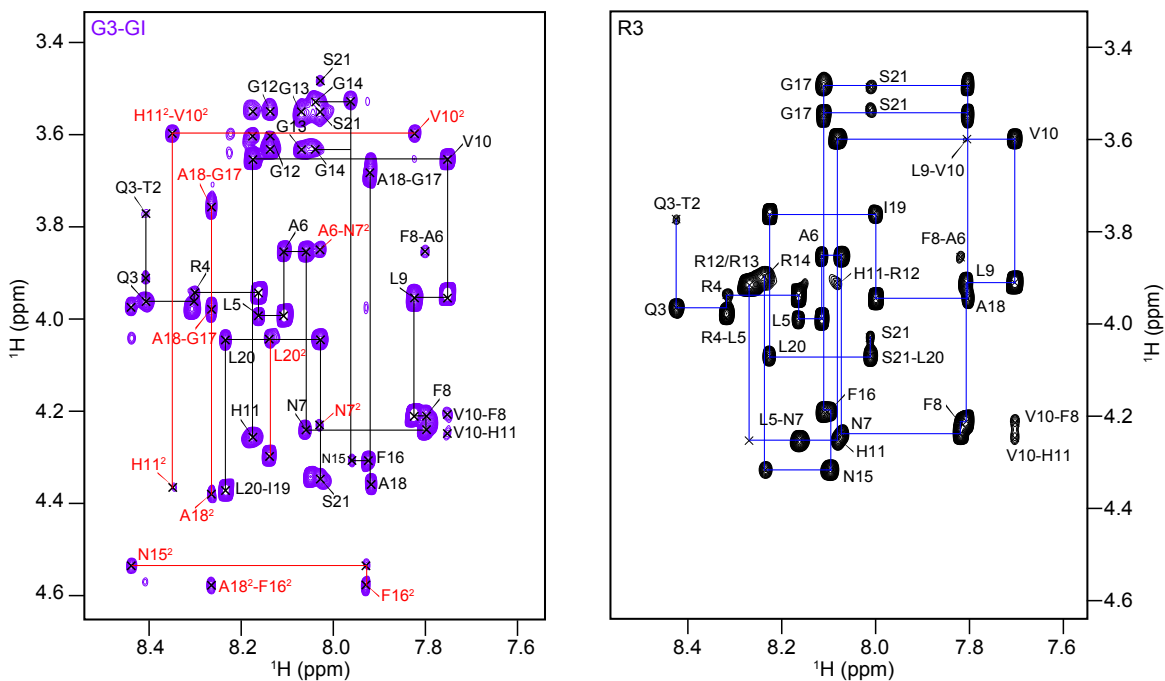
Figure 28: Sequential resonance assignment of 0.5 mM G3-GI peptide (left, peaks are labeled with purple color) and 1.0 mM R3 peptide (right, peaks are labeled with black color).
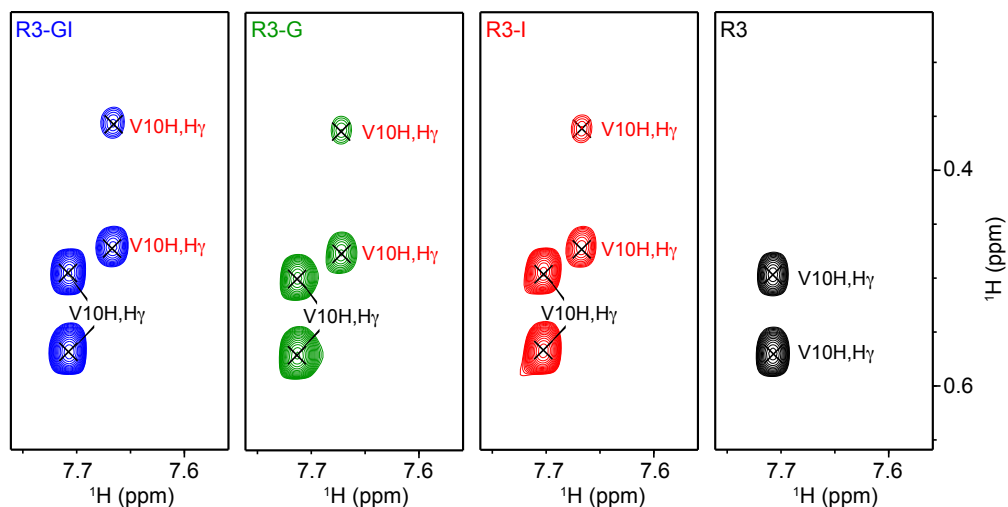
Figure 29: Downfield shifted resonance of Val10-Hγ from 1.5 mM R3-GI, 1.0 mM R3-G, 1.0 mM R3-I and 1.0 mM R3 peptide, respectively.

With mono-methylation modification, two sets of chemical shifts for residues Phe8-His11 and residues Asn15-Ser21 were observed in both R3-G peptide and R3-I peptide. The observation suggests that *N*-methylated modification at the C-terminal of the R3-GI peptide not only causes the *cis*/*trans* conformer in the C-terminus, but also induces the conformational change on the opposite site of the linker for the random coil peptide. In contrast, only one set of chemical shifts was observed from none *N*-methylated R3 peptide, which indicates that there is only one conformer in R3 peptide.

The interaction between side chain of Val10 and the imidazole ring of His11 induced the downfield shifting of resonance Val10Hγ. It is consistent with the molecular dynamic ensemble result which the imidazole ring of residue His11 is in close proximity to the side chain of Val10. The similarity of 2D ^{1}H–^{1}H correlation spectra of Val10 at different pH conditions (**Figure 30**) and different salt conditions (**Figure 31**) indicates that the pH and salt conditions have no influence on the peptide conformation. However, the peak intensity of His11–Val10 is higher at a relatively low pH condition, implying that tending to the protonation state of the imidazole ring not only leads to the local chemical shifts changes, but also has effects on the amide proton exchange rate, further to enhance the signal intensity of the amide proton.
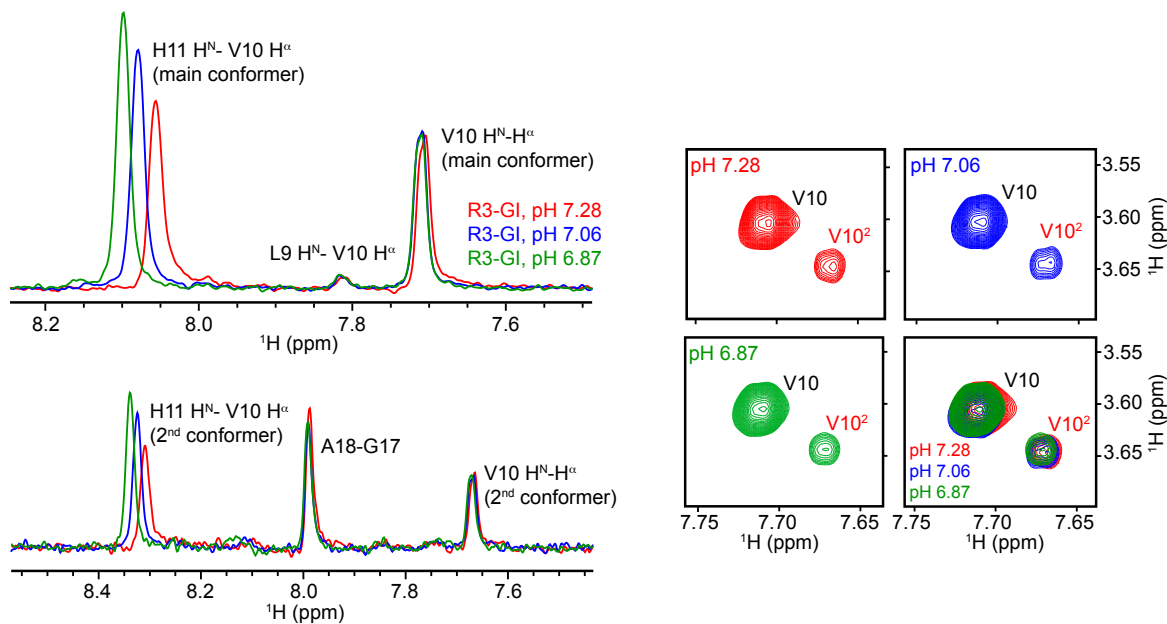
Figure 30: 1D Val10 comparison for 0.5 mM R3-GI peptide at different pH conditions. Different 1D slices were extracted from 2D NOESY experiment at the corresponding pH condition.
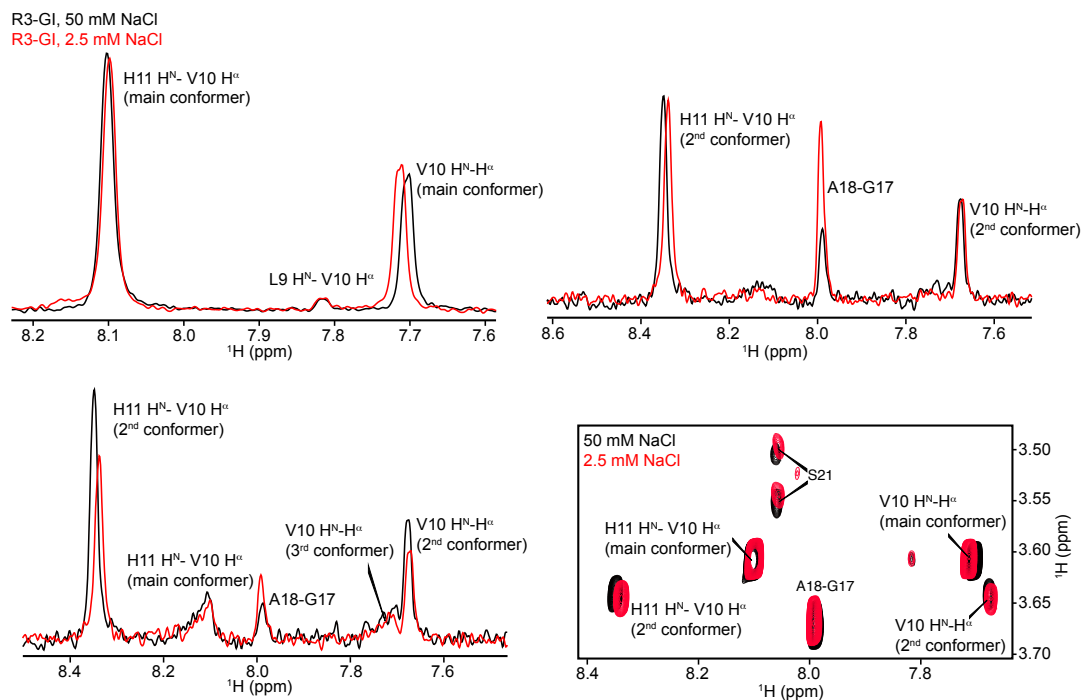
Figure 31: Val10 conformers comparison for 0.5 mM R3-GI peptide at different salt conditions. Different 1D slices were extracted from 2D NOESY experiment at the corresponding salt condition.

3.8 Substrate Interactions of ISMs with Aβ Peptide

ISMs peptides are designed to inhibit the aggregation process for both Aβ and IAPP. From the ThT binding assay and 3-[4,5 dimethylthiazol-2-yl]-2,5-diphenyltetrazolium bromide (MTT) assay, the linker containing three arginine in the R3-GI peptide can block Aβ fibrillation and toxicity.[85] In order to detect the substrate interactions of ISMs with $Aβ_{40}$ peptide, HSQC spectra and DIC images were recorded accordingly. For solution-state NMR, 1:1 and 1:5 molar ratios complexes of ^{15}N-labeled $Aβ_{40}$ peptide to unlabeled R3-GI peptide were prepared to analyze the chemical shifts and peak intensity differences. As a non-inhibitory peptide mimic, G3-GI was performed the same measurement as a negative control in comparison to R3-GI peptide. The protocol for $Aβ_{40}$ peptide expression and purification is described in Chapter 2. Concerning DIC measurement, Fluos-R3GI, Fluos-G3GI and Fluos-K3L3K3GI were labeled with green fluorescence. In contrast, $Aβ_{40}$ peptide was labeled with Fluor-647 dye which yields red fluorescence to distinguish from the green fluorescence of ISMs peptides.
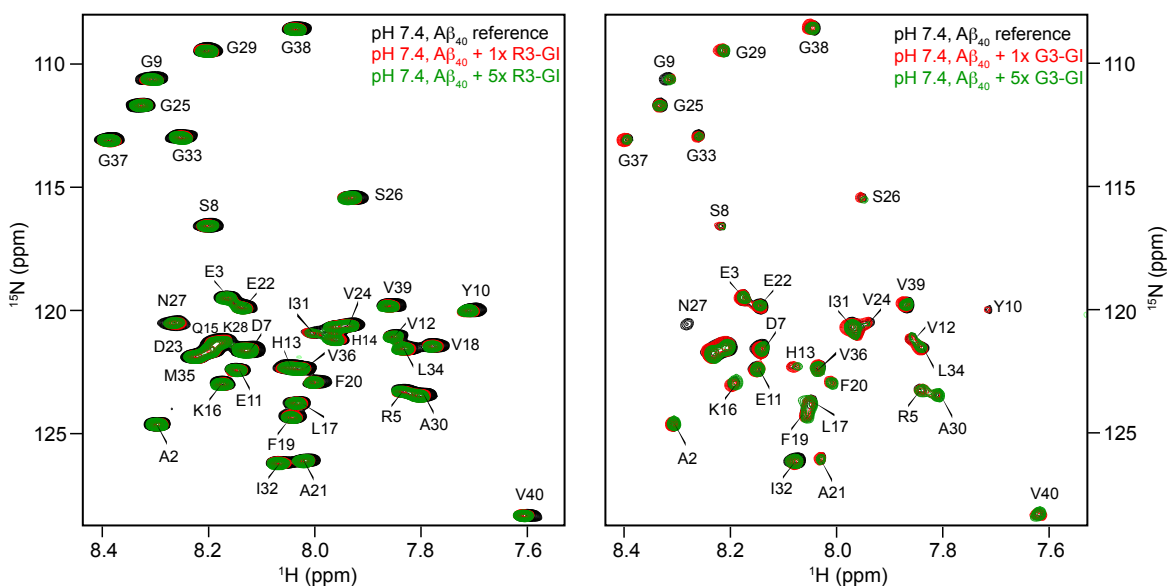
Figure 32: $^1H–^{15}N$ HSQC spectra superposition of 20 μM $Aβ_{40}$ peptide mixed up with 1-fold and 5-fold molar excess of R3-GI (left) and G3-GI peptide (right) at pH 7.4 condition. The spectra were recorded at 277 K using a Bruker Avance III 600 MHz spectrometer. The number of scans for HSQC was 16 in the left hand and 8 in the right hand.

In addition of five-fold molar ratio of ISMs peptides to $Aβ_{40}$ peptide, the peak intensity was still at the similar level, implying that R3-GI and G3-GI peptide did not affect the solubility of $Aβ_{40}$

monomeric peptide at five-fold excess molar of ISM peptide. However, the DIC fluorescence images demonstrated $A\beta_{40}$ and R3-GI co-localized in the droplet-like aggregates. At a pH 7.4 condition, there were slightly chemical shifts differences for several peaks in the mixture of R3-GI with $A\beta_{40}$ and G3-GI with $A\beta_{40}$ (**Figure 32**). Given the NOE intensity of R3-GI peptide was higher at low pH conditions, we adjusted the pH of the above samples to pH 6.0 and recorded the HSQC spectra to identify the chemical shifts and signal intensity differences. At a low pH condition, the chemical shifts differences were larger and easier to be observed (**Figure 33**).
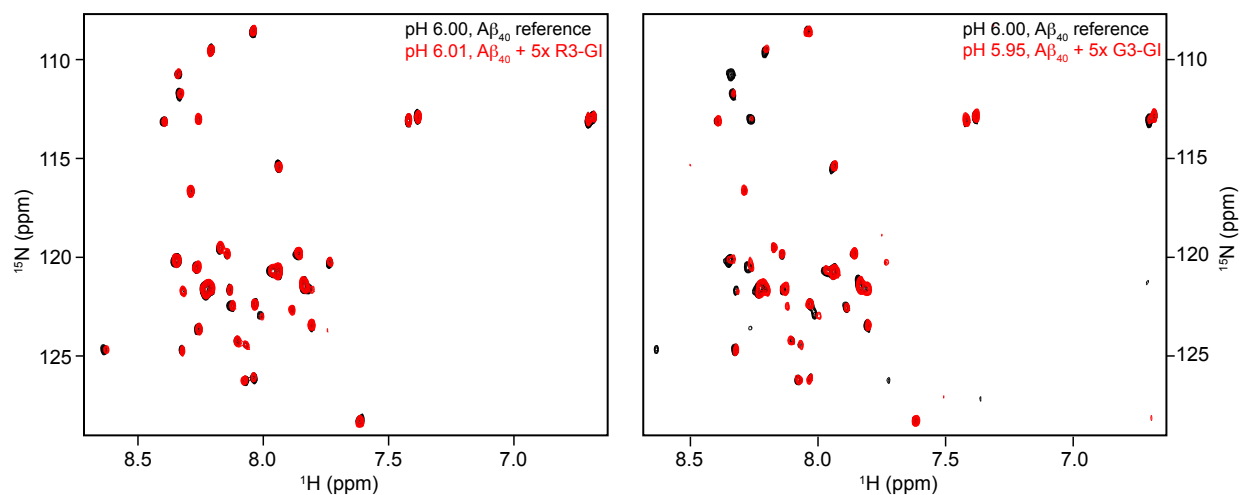
Figure 33: $^1H–^{15}N$ HSQC spectra superposition of 20 μM $A\beta_{40}$ peptide mixed up with 5-fold molar excess of R3-GI (left) and G3-GI peptide (right) at pH ~6.0 condition. The spectra were recorded at 277 K using a Bruker Avance III 600 MHz spectrometer. The number of scans for HSQC was 16 in the left hand and 8 in the right hand.

In order to visualize the interactions between ISMs and $A\beta_{40}$, DIC and fluorescence images were captured at room temperature. Fluos-labeled ISMs has been imaged immediately after dissolution into phosphate buffer containing 1% (v/v) HFIP without filtration. After incubation of Fluos-R3GI and Fluos-K3L3K3GI with Fluos-647-$A\beta_{40}$, the liquid droplet-like structures with a perfect merge of both red and green fluorescence were yielded. The finding demonstrated R3-GI and K3L3K3-GI peptide were co-localized with $A\beta_{40}$ peptide into the aggregates. Whereas Fluor-647-$A\beta_{40}$ incubated with Fluos-G3GI yielded a distinct spatial distribution of red and green fluorescent spots, suggesting that G3-GI did not co-localize or partly co-localized with $A\beta_{40}$. The channel merging images comparison of Fluos-R3GI, Fluos-K3L3K3GI and Fluos-G3GI with Fluor-647-$A\beta_{40}$ are shown in **Figure 35**. It is worth noting that G3-GI as a non-inhibitor for $A\beta$, cannot suppress the

fibrillogenesis and cytotoxicity of Aβ. [85] The nature of this phenomenon could be ascribed to the different strength of the binding interactions between ISMs and Aβ$_{40}$, which is consistent with the fluorescence titration studies that was applied to determine the apparent K$_d$ of ISMs with Aβ$_{40}$. The apparent K$_d$ value of G3-GI with Aβ$_{40}$ is around eight times larger in comparison to R3-GI and K3-GI,[85] suggesting a lower binding affinity and weaker interactions.
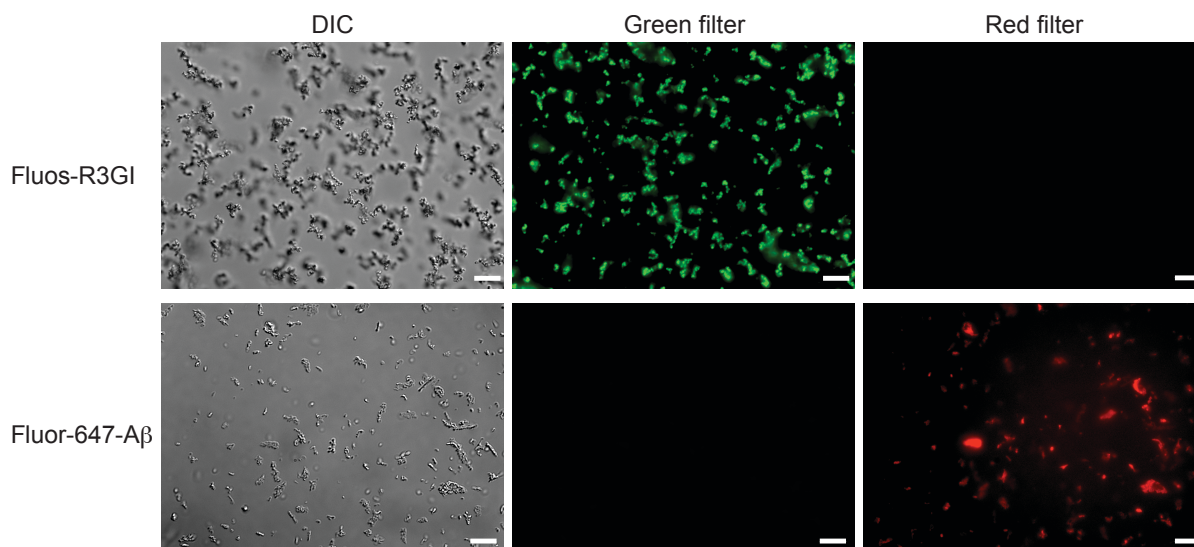
Figure 34: DIC images and fluorescence images of Fluos-R3GI peptide (top) and Fluor-647 labeled Aβ$_{40}$ peptide (bottom) with 10 μm scale bar. GFP filter cube (with excitation at 470 nm and emission at 525 nm) and Y5 filter cube (with excitation at 620 nm and emission at 700 nm) were used to capture the fluorescence images.

R3-GI : Aβ$_{40}$ = 1:1

| DIC | Green filter | Red filter | Merge channels |

K3L3K3-GI : Aβ$_{40}$ = 10:1

G3-GI : Aβ$_{40}$ = 1:1

G3-GI : Aβ$_{40}$ = 10:1
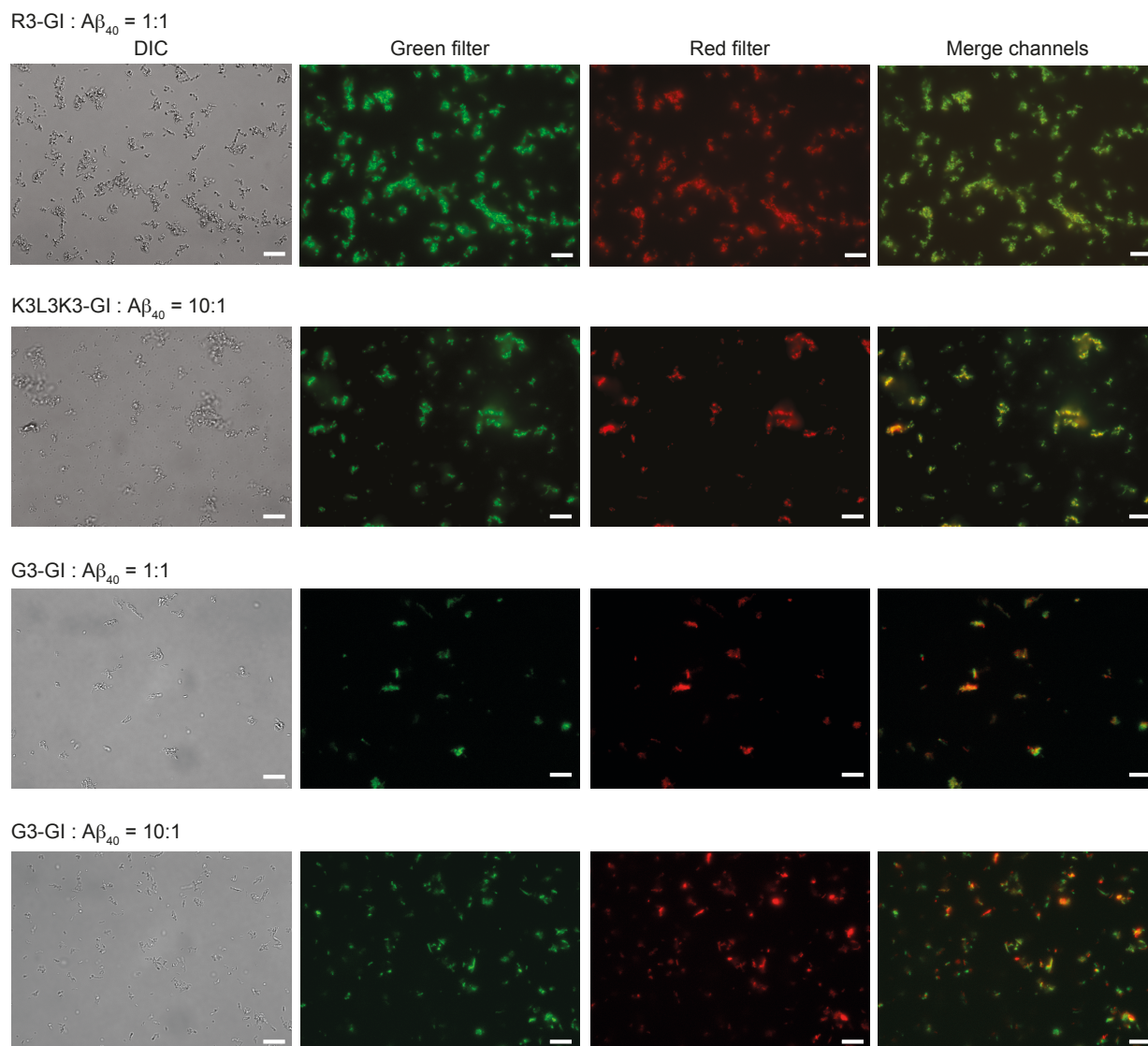
Figure 35: DIC images and fluorescence images of Fluos-labeled ISMs peptide and Fluor-647 labeled Aβ$_{40}$ peptide, scale bar is 10 μm. Setting up for the filter cubes were same as Figure 34. The green and red fluorescence labeled structures in the mixture of Fluos-R3GI with Fluor-647-Aβ$_{40}$ and Fluos-K3L3K3GI with Fluor-647-Aβ$_{40}$ were overlaid after merging the two channels. In contrast, in the mixture of Fluos-G3GI with Fluor-647-Aβ$_{40}$, some structures exhibited the separated green and red fluorescence.

Different properties and structures of ISMs peptides are induced by different amino acids in the linker region. Generally, arginine and lysine are charged amino acids and both are able to form a salt bridge with either aspartic acid or glutamic acid to stabilize the protein structure. These two amino acids prefer to locate on the surface of protein with their side chain partly buried. The similarity of these two amino acids leads to R3-GI and K3-GI peptides exhibit the similar binding

strength with Aβ peptide. However, glycine is a unique amino acid which contains a hydrogen as its side chain. The uniqueness makes glycine more flexibility and plays a distinct functional role from other amino acids. The differences in the amino acid structure and property can be attributed to explain why the different linker show different inhibitory functions. More flexible in the loop region of ISMs inhibitors, less inhibitory effects on the ISMs function. Either hydrophobic amino acids like phenylalanine and leucine or charged amino acids like arginine and lysine as a linker could yield a highly active anti-amyloidogenic inhibitor. The β-hairpin or β-sheet/β-turn population in ISM peptide could mediate a high affinity binding interaction with prefibrillar amyloid species to form amorphous and non-toxic species. Taken together, we speculate that the ISM peptide inhibitors are very dynamic in the oligomeric state and provide a hydrophobic binding surface similar to a micelle that recruits amyloidogenic peptides into the protein dense phase. This finally results in co-precipitation of the amyloid peptide and the ISMs peptide inhibitors.

3.9 Ensemble Modelling and Molecular Dynamic Simulation[2]

Ensemble modelling of R3-GI peptide were conducted in Metadynamic Metainference by using the experimental NOE distance restraints. Conformational ensembles for major conformer Gly17^{trans}/Ile19^{trans} R3-GI and minor conformer Gly17^{cis}/Ile19^{trans} R3-GI were obtained by using 221 and 35 inter-residues distance restraints for the first and the second conformer, respectively. Simulations were performed with GROMACS using PLUMED2 and the PLUMED-ISDB module that implements Metadynamic Metainference and multiple experimental restraints. In Metadynamics Metainfence multiple replicas of a system in the same experimental conditions are run in parallel. The replicas are coupled by a potential that is applied on the replica-averaged back calculated NOE-distances and restrains the calculated observables to their experimental values within an error that is estimated on-the-fly by Gibbs sampling. Furthermore, the sampling of the replicas is enhanced by multiple-walkers parallel-bias Metadynamics, where multiple collective variables are biased at the same time and the history-dependent bias is shared among the replicas.

The ensemble result for each conformer is highly heterogenous and extremely different with each other. More specifically, in the major conformer Gly17^{trans}/Ile19^{trans} R3-GI, the ensemble is characterized by an equilibrium between two populations. The first population is lack of the

---

[2] Ensemble modelling and MD simulation in Section 3.9 were collaborated with Prof. Dr. Carlo Camilloni.

secondary structure and with a large radius of gyration in the order of ~1.3 nm. In contrast, the second population is characterized by a β-like structure from residue Asn7 to residue Ser21. In the minor conformer Gly17^{cis}/Ile19^{trans} R3-GI, although there is no indication of β structure from the ensemble result, the structure is more compact and with an average radius of gyration of 0.9 nm.
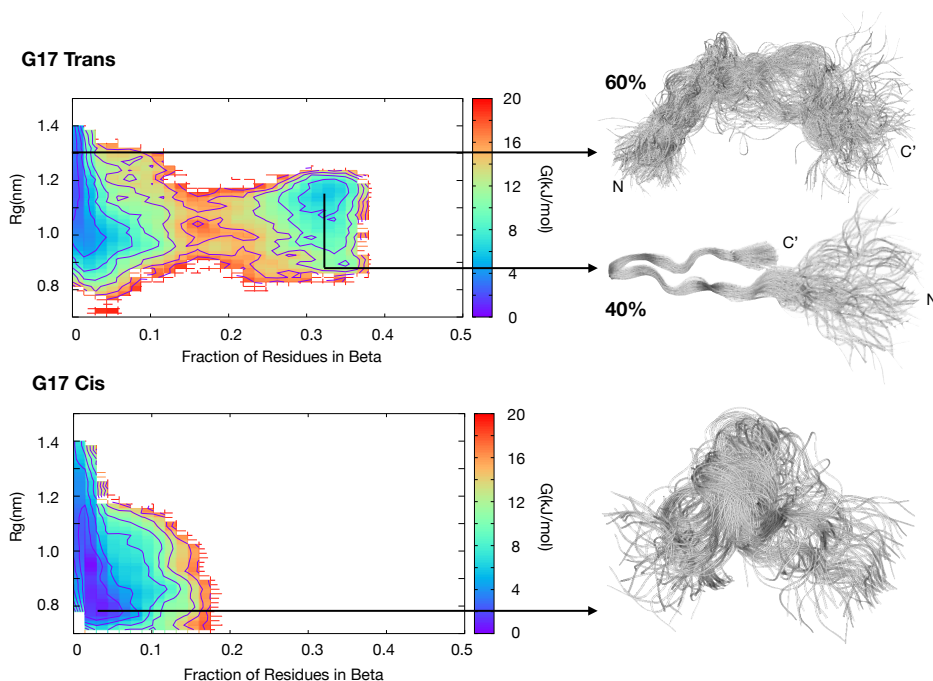
Figure 36: Free energy diagram and structural ensembles for R3-GI. Figures were plotted by Prof. Dr. Carlo Camilloni.

To investigate the interaction of the peptides with each other, over 100 μs of coarse grain simulations were performed using GROMACS. 27 or 54 monomers were solvated in a cubic box with the lateral length of 18 nm or 22.7 nm. The structure of the individual monomer was described employing an elastic network centered around a representative Gly17^{trans}/Ile19^{trans} β-turn like conformer. After 10 μs, the average oligomer size is stable and populates between 24 and 30 monomers. Although the molecules self-assemble quickly on the time scale of the simulation, the molecules are highly dynamic showing a broad size distribution between free monomers and oligomer fraction (**Figure 37A, B**). From a structural perspective, the monomer-monomer interface is well defined and characterized by several inter-molecular interactions (**Figure 37C**) and by solvent-exposed arginine side chains (**Figure 37D**) without regard to the oligomer size. To

test whether the model was sensitive enough to discriminate between different sequences and structures, two additional long simulations were performed of a (SG)₁₀S peptide with and without the elastic network containing the structural information of the R3-GI peptide. The results indicate that the oligomer dynamics disappears with monomers self-assembling into a full 54-mer oligomer. Furthermore, the specific inter-monomer interactions are not found any longer, implying that the important role of both sequence and structure in determining the properties for R3-GI as described above.
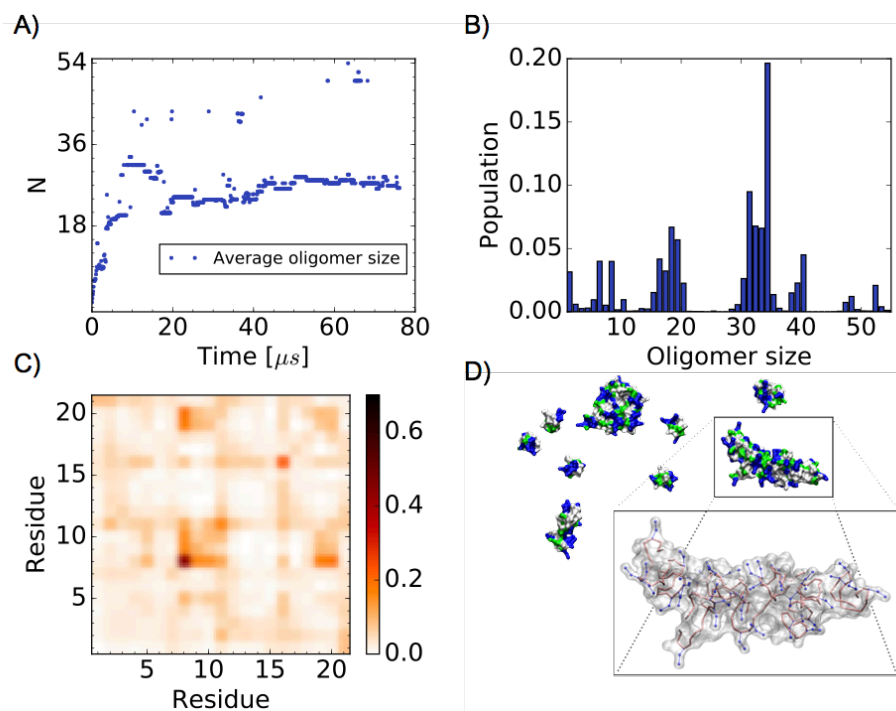
Figure 37: Coarse-grained modelling of R3-GI oligomers. Figures were plotted by Prof. Dr. Carlo Camilloni.

3.10   Summary and Outlook

The work discussed in this chapter mainly presented the structural information of ISM R3-GI peptide inhibitor. With the double *N*-methylation modification at the two residues Gly17 and Ile19 which are located at the same side of the β-strand in the amyloid core, a highly soluble and non-amyloidogenic inhibitor was designed and synthesized to inhibit amyloid fibrillation and reduce the inducing toxicity. The preliminary characterization on the R3-GI peptide was performed by TEM, DIC and DLS to capture the higher molecular weight species. The oligomers with higher

molecular weight adopt liquid droplet-like structures were observed from the DIC measurement in both normal mode and fluorescence mode.

However, the oligomeric state R3-GI is too large to be observed by solution-state NMR. In contrast, monomeric state R3-GI peptide yields high-resolution and high sensitivity solution-state NMR spectra. The monomeric state R3-GI peptide adopts random coil conformation with the loop structure in the arginine linker region. Meanwhile, the chemical exchange process between a monomeric state R3-GI peptide and an aggregated state R3-GI peptide was confirmed by STD experiment. The exchangeable properties explain that the high quality of the solution-state NMR spectra is attributed to the monomeric state R3-GI peptide. The observation based on the STD and transfer-NOEs implies that the structure of the R3-GI peptide in the aggregate state are very dynamic. The droplet-like state aggregates could provide a hydrophobic binding surface to recruit amyloidogenic peptides into the protein dense phase, further to result in co-precipitation of the amyloid peptide with an ISM peptide inhibitor. In combination with dynamic simulation, the structural information of the R3-GI peptide was gained. In the major conformer $Gly17^{trans}/Ile19^{trans}$ R3-GI, there is an equilibrium between two populations, the first population is lack of the secondary structure, whereas the second population is characterized by a β-like structure from residue Asn7 to Ser21. Although there is no indication of β structure in the minor conformer $Gly17^{cis}/Ile19^{trans}$ R3-GI, the structure is more compact in comparison to the major conformer.

Further studies regarding to this research could be divided into five aspects. Due to the property of the linker determines the structure of ISMs peptides, and the inconsistent structure of ISMs could induce different influences on the self-interaction, cross-amyloid interactions and the cellular toxicity of Aβ and hIAPP. The characterization and comparison of structural details of different ISMs peptides from diverse linkers should be considered as the first research target. Second, the effects of *N*-methylation modification on the substrate interactions with amyloid peptide like Aβ and hIAPP could be designed and analyzed to provide more insights into the cross-amyloid interactions, including none *N*-methylated, mono *N*-methylated and double *N*-methylated ISMs. Third, the structural investigation on the cyclic peptide mimics[142] based on IAPP sequence could be performed in order to provide a novel perspective on the anti-amyloid drugs design. Due to their nanomolar inhibitory functions on amyloid self-association and amyloid cross-interaction, the structure differences at the atomic level between the linear mimics and the cyclic mimics could

gain insights on the inhibitory mechanism of different peptide mimic inhibitors. Fourth, the amino acids in the hot-segment of ISMs could be substituted with Aβ sequence owing to the highly similarity between IAPP sequence and Aβ sequence. Therefore, Aβ peptide sequence-based either linear peptide mimics or cyclic peptide mimics could also be designed, synthesized and applied to inhibit the fibrillation process and block the cellular toxicity. Last but not least, a selective peptide mimic inhibitor for either Aβ or IAPP should be screened and compared to illuminate the mechanism of the inhibitory interactions, further to serve for the design of novel peptide-based drugs to target amyloid assembly in AD or Type 2 Diabetes.

Chapter 4

Interactions between Aβ$_{40}$ Fibrils

and PET Tracer Molecules

70

4 Interactions between Aβ$_{40}$ Fibrils and PET Tracer Molecules

4.1 Aim

The preclinical and clinical researches on AD diagnosis are focused on the development of PET staining agents for amyloid plaques that consist of Aβ aggregates. The bithiazole-like small molecules have been developed as novel PET tracers for Aβ deposits with strong affinity and high selectivity. However, the stoichiometry of the binding interactions and the binding mechanism at the atomic level are not yet fully understood. The aim of this project is to expand our understanding on the Aβ-PET tracer[3] binding mechanism at the atomic level and to provide insights on the development of the next generation of PET tracers for AD diagnosis. The method used to achieve such goal is to perform the study on the structural characterization of Aβ-PET tracer complexes by using MAS solid-state NMR.

The amyloid polymorphism is one of the big obstacles to prepare a uniformly homogenous fibrillar sample for MAS solid-state NMR. In this project, uniformly ^{13}C, ^{15}N-labeled Aβ$_{40}$ peptide were purified with ion-exchange chromatography (IEC) method and HPLC method, respectively. In order to evaluate the influences of the purification protocol on the morphology of amyloid fibrils, two solid-state NMR Aβ$_{40}$ fibrils samples were prepared by incubating the monomeric Aβ$_{40}$ peptide with the same seeds, in which the monomeric Aβ$_{40}$ peptide was produced from two different methods. On the other hand, fibrils are generally incubated in aqueous solution, whereas the bithiazole-like small molecule is only soluble in aqueous solution with the nanomolar range. Due to its hydrophobic nature, it has relatively high solubility in organic solvent like DMSO and ACN. To overcome the solubility issue, BSA carrier system has been established to titrate the highly hydrophobic small molecule to amyloid fibrillar aggregates in a manner that is compatible with physiological conditions. Seeding protocol is able to introduce an approach to prepare a highly homogenous fibrils sample for MAS solid-state NMR. Benefit from the BSA carrier system, PET tracer small molecule is able to be titrated to amyloid fibrils and yields well dispersed MAS solid-state NMR spectra that are amenable for structural characterizations. As chemical shifts are sensitive to the subtle changes of the physical and chemical environment, tracing chemical shifts differences with the respect of the reference fibrils could provide better understanding of the

---

[3] PET tracer small molecules used in the project discussed in Chapter 4 were provided by Dr. Behrooz H. Yousefi.

interactions between amyloid fibrils and PET tracer small molecules. In combination with a reported atomic resolution structural model of Aβ, the potential location of the binding sites and the binding mechanism could thus be proposed. It's worth to note that the chemical shift perturbation merely indicates that there is a change in the magnetic environment of a nucleus. The widespread CSPs could be induced by either the structural conformational rearrangement or direct interactions from a binding partner.

4.2 Amyloid Polymorphism

Amyloid polymorphism[143–147] at the molecular structure level can be observed by the appearance from the TEM images.[143] In addition, the mass-per-length values from dark-field EM[148,149] and more than one set of chemical shifts from solid-state NMR measurement[24,119,148,150,151] also demonstrated the presence of the molecular-level polymorphism. In general, molecular structures of amyloid fibrils which are prepared *in vitro* has no relationship with the protein sequence. They are determined by the details of fibrils incubation conditions. From the perspective of dynamics and kinetics, the precise fibrils growth conditions lead to the different nucleation rates and elongation rates during the fibrils formation process, which might be one of the reasons to explain a diversity of morphologies. However, seeding is one of the methods to prepare the homogeneous fibrils and passes all the morphological features, such as the width and twist period, from the parent generation to the subsequent generation.[148] In terms of the seeding protocol, the parent fibrils are used as the source of seeds and incubated with 10 to 50-fold excess of monomeric peptide to generate highly homogeneous fibrils.

Concerning Aβ40 fibrils, there are two different morphologies from TEM images, the striated ribbons morphology and twisted morphology. The main difference between these two morphologies is the overall symmetry of the fibrils. The striated ribbons fibrils adopt a two-fold rotational symmetry, whereas the twisted fibrils contain a three-fold symmetry. Furthermore, the salt-bridge formed by side chains of Asp23 and Lys28 which stabilizes the fibrils structure, is only presence in the striated ribbons fibril with two-fold symmetry. However, it is worth noting that the salt-bridge Asp23-Lys28 contact exists in the three-fold symmetric Aβ40 fibrils which are derived from the brain tissue of AD patient.

There are several distinct morphologies of Aβ40 fibrils being reported from solid-state NMR labs.[24,119–121,126,145,146,148,150–153] In most cases, the N-terminus of Aβ40 is disordered and too dynamic to be observed in solid-state NMR experiments except for two structural models.[120,121] Both of these two Aβ40 fibrils formed from the recombinant peptide which were purified by IEC method.[154] In order to get an insight either the seeding protocol or the purification protocol has a stronger impact on the molecular structure of Aβ40 fibrils, two Aβ40 fibrils with the same seeds were prepared, in which the monomeric peptide was purified by two different purification protocol (HPLC vs IEC). Subsequently, the Aβ40 fibrils were centrifuged and packed into a 3.2 mm MAS solid-state NMR rotor, respectively. The C−C and N−C correlation spectra were recorded and processed with the identical processing parameters to detect the chemical shifts differences of the two fibrils samples.
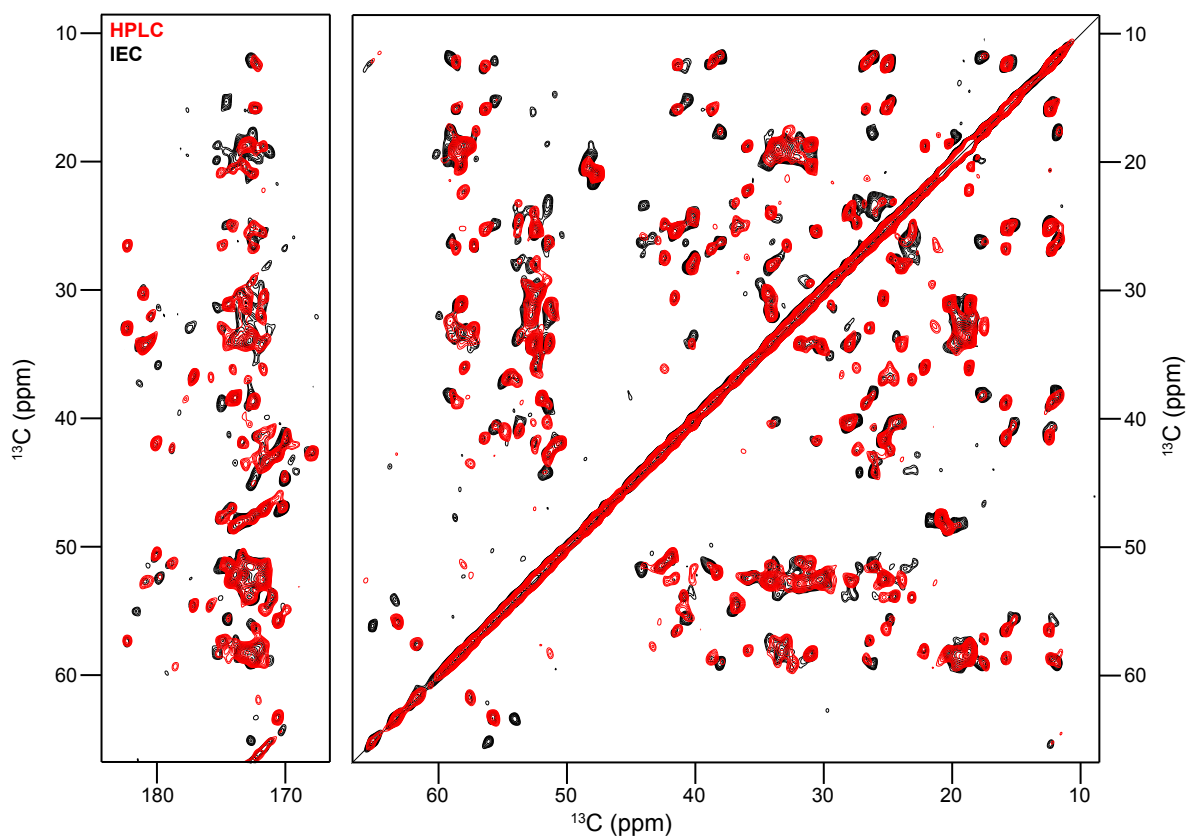
Figure 38: Superposition of 2D ^{13}C–^{13}C PDSD spectra of $^{13}C,^{15}N$-labeled Aβ40 fibrils purified by two different methods, red spectrum is from the HPLC method and black is from the IEC method. The spectra were acquired on a Bruker Avance III 750 MHz spectrometer at 273 K and 10 kHz MAS rate with a 50 ms mixing time.

Although Aβ$_{40}$ fibrils were incubated with the same seeds, several peaks with chemical shift perturbations in the C–C correlation spectra were observed. The main difference in the PDSD spectra of the two fibrils was displayed in the serine region. Only one single set of signals for residue Ser8 and residue Ser26 was detected when peptide was purified by the HPLC method, whereas two sets of CS were observed from the IEC method which suggested that there were polymorphisms in this case. The results indicate the purification methods for monomeric peptide production also has an impact on the amyloid conformation. Meanwhile, the N–C correlation TEDOR spectra were well overlaid and showing small CS differences compared with PDSD spectra. The result that only small CSPs of nitrogen could be detected may be explained by the fact that the chemical shifts for nitrogen on the amide group disperses in a smaller spectral region in comparison to aliphatic carbon. For the detailed influences of the two purification methods on the molecular structures of Aβ$_{40}$ fibrils, solid-state NMR assignment experiments need to be recorded to provide more information on the atomic resolution structures of both fibrils.
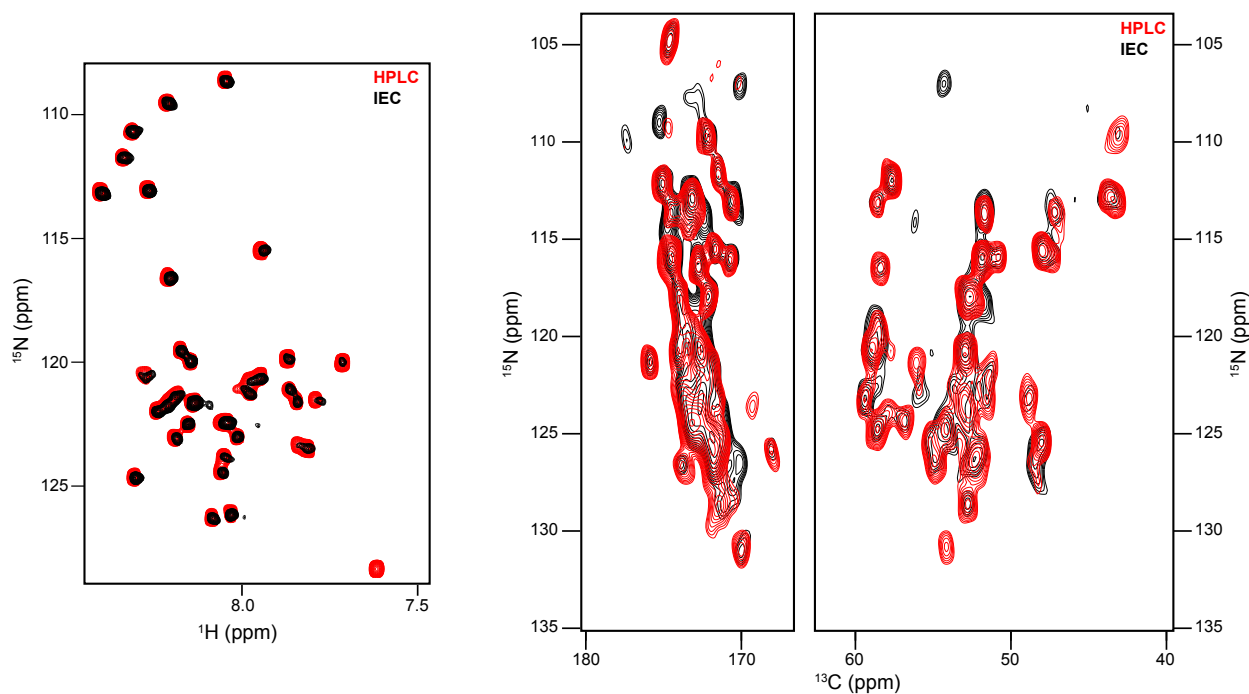
Figure 39: Left, superposition of 2D HSQC solution-state spectra of $^{13}C,^{15}N$-labeled monomeric Aβ$_{40}$ peptide purified by two different methods. Right, superposition of 2D ^{15}N–^{13}C TEDOR spectra of $^{13}C,^{15}N$-labeled Aβ$_{40}$ fibrils prepared by monomeric peptide from two different methods. The spectra were acquired on a Bruker Avance III 750 MHz spectrometer at 273 K and 16.5 kHz MAS rate with a 1.9 ms mixing time.

4.3 Solid-state NMR Titration

Solution-state NMR titration is one of the most powerful techniques to quantify protein-protein and protein-ligand binding interactions at the molecular level.[155–157] From the designed NMR titration experiments, binding sites and binding affinity are identified based on several parameters, which mainly include chemical shifts and resonance signal changes, relaxation time, diffusion constant changes, and NOE effects changes. However, it is difficult to titrate a ligand to protein aggregates in solid state. Here a protocol to titrate the hydrophobic molecule to amyloid fibrillar aggregates for further measurements with MAS solid-state NMR has been established. The small molecules involved in this project are highly hydrophobic, such as bithiazole-like molecule and Pittsburgh compound B. In particular, the bithiazole-like molecule is only solubilized in aqueous buffer in the nanomolar range. By using BSA as a carrier, the small molecules were successfully titrated from BSA carrier to the pre-formed amyloid fibrils at physiological condition.
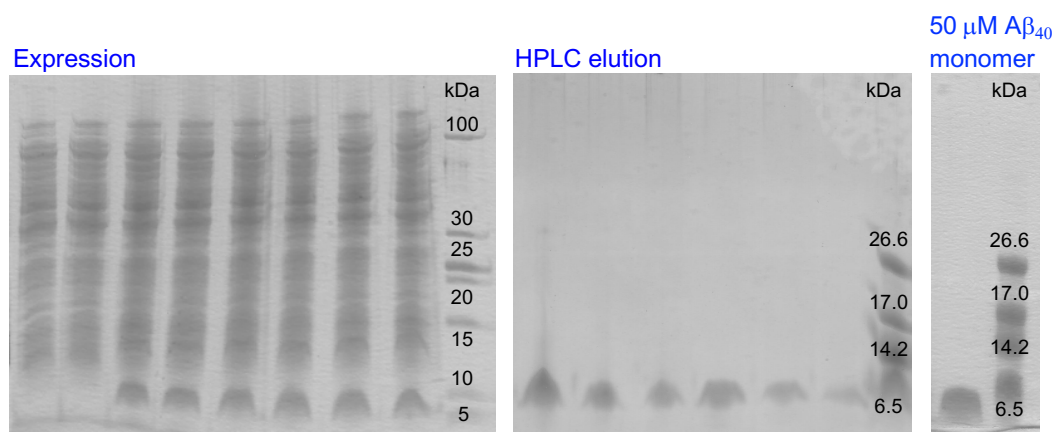
*Figure 40: Expression and purification procedures test by tricine SDS-PAGE. The righthand image is the 50 μM monomeric peptide for fibrils preparation. The details of the procedures are described in **2.1.1**.*
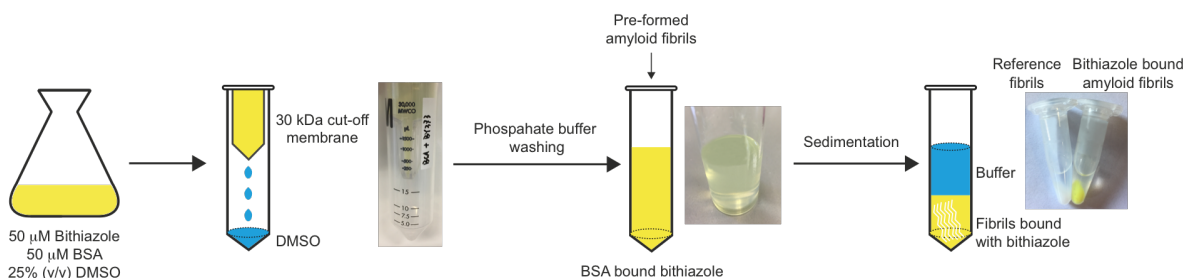
Figure 41: A diagram of the solid-state NMR titration protocol for transferring bithiazole-like molecule to pre-formed amyloid fibrils.

Bithiazole-like molecule is a yellow powder and found to specifically bind with Aβ fibrils. After titration of the above molecule to pre-formed $A\beta_{40}$ fibrillar aggregates, a clear color change from white to yellow of $A\beta_{40}$ fibrils was observed, suggesting the molecule bound to $A\beta_{40}$ fibrils (**Figure 41**). From the 1D ^{13}C and ^{15}N CP experiments in MAS solid-state NMR shown in **Figure 42**, the sensitivity and resolution of the 1-fold, 2-fold and 4-fold molar excess of bithiazole-like molecule to $A\beta_{40}$ fibrils were comparable with the $A\beta_{40}$ fibrils reference sample. It indicates that the titration protocol with BSA carrier system works in the proposed way.
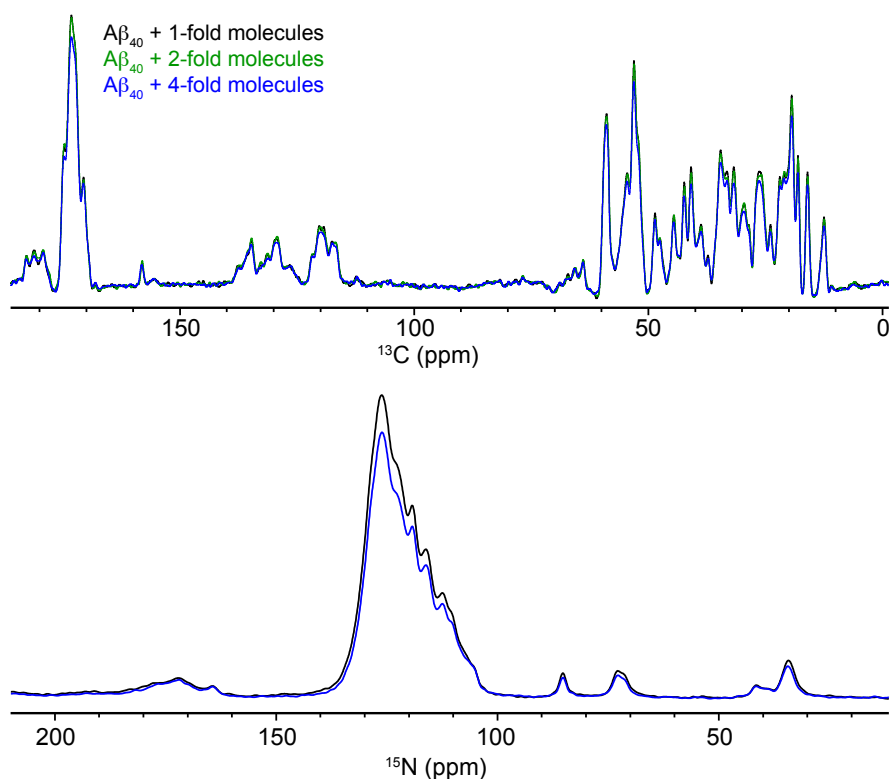
Figure 42: Superposition of 1D ^{13}C and ^{15}N CP spectra of the fibrils titrated with bithiazole-like molecule at different molar ratios.

In order to quantify the stoichiometric ratio of the interactions between Aβ and PET tracer molecules, UV-vis spectra were recorded to monitor the BSA carrier system. To obtain quantitative characterization information of the titration protocol, the molar extinction coefficient (ε) of bithiazole-like molecule was firstly calculated from the absorbance and concentration data. The parameter ε is used to measure how strongly of a molecule absorbs light at a specific wavelength. The extinction coefficient of bithiazole-like molecule was calculated by the linear

fitting of the UV absorption data at 415 nm wavelength. At two different buffer conditions, the coefficient is on the order of 6.88 mM^{-1} • cm^{-1} and 7.24 mM^{-1} • cm^{-1}, respectively.
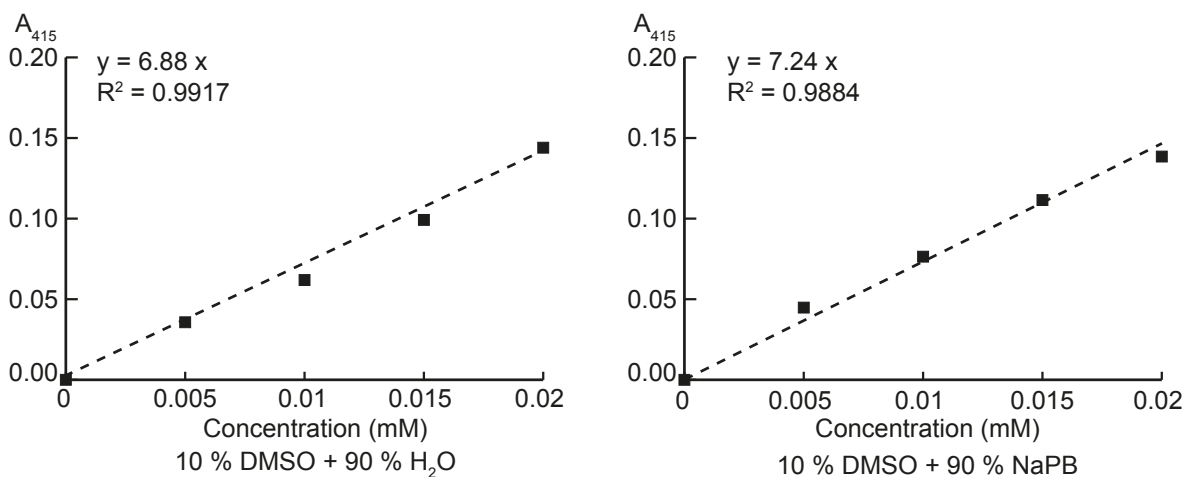
Figure 43: Molar absorbance coefficient (ε) of bithiazole-like molecule in different buffer conditions from absorbance and concentration data.
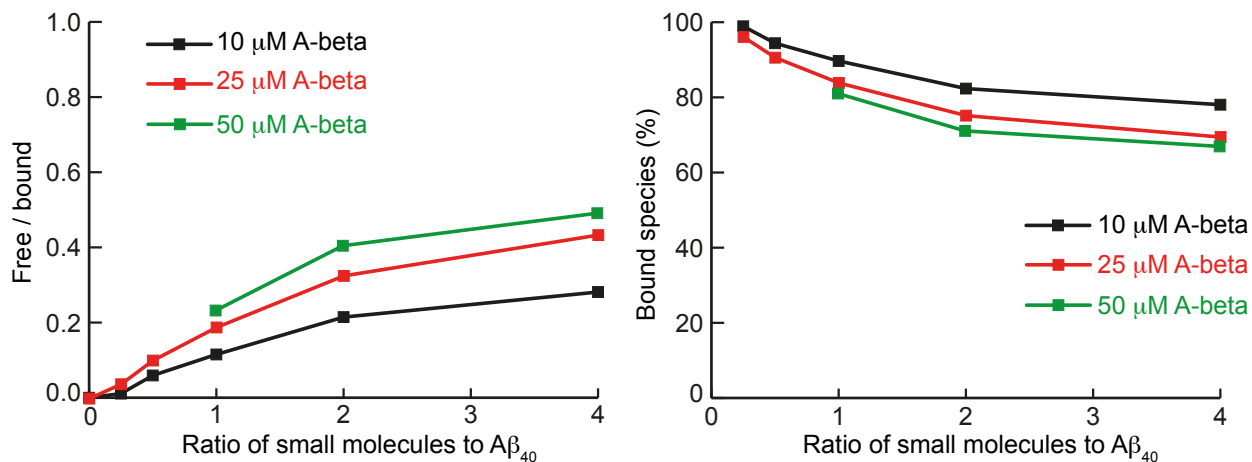
Figure 44: Left, the distributions of free bithiazole and bound bithiazole at different molar ratios of bithiazole-like molecule to Aβ$_{40}$ fibrils. Right, bound bithiazole-like molecule in percentage proportions at different molar ratios of small molecules to Aβ$_{40}$ fibrils. Figures were plotted by using UV-vis spectroscopy data.

Furthermore, to gain the stoichiometric information of the Aβ-bithiazole interactions, the UV$_{280}$ and UV$_{415}$ absorption were analyzed to quantify the transfer efficiency of bithiazole-like molecule from BSA carrier to the pre-formed Aβ$_{40}$ fibrils. The strength of the binding interactions to form non-covalent Aβ-bithiazole complex is determined by the molar mass of the free and bound species

at a chemical equilibrium. The UV absorbance at 415 nm A_{415} is plotted (**Figure 44**) to analyze the distributions of the free bithiazole from the supernatant and the bound bithiazole from the pellets. As the molar mass of bithiazole increasing, the population of bound bithiazole gradually decreasing, suggesting that the binding interactions is saturable and all the binding sites on $A\beta_{40}$ fibrils are occupied. Similarly, at a high protein fibrils concentration, not any significant increasing in the binding interactions reflects its saturable binding. There might be three small molecule binding with one protein molecule on the basis of the UV-vis data in **Figure 45** left. However, more data points are needed to be measured in the saturation figure in order to get an exact value of the stoichiometry. Additionally, the protein concentration has negligible effects on the fractional saturation θ. The binding affinity for this interaction is in micromolar range from the Scatchard plot (**Figure 45**, right). The non-linear fitting in Scatchard plot confirms the presence of the multiple binding interactions and these non-identical binding sites are interfering with each other in a negative cooperativity way.
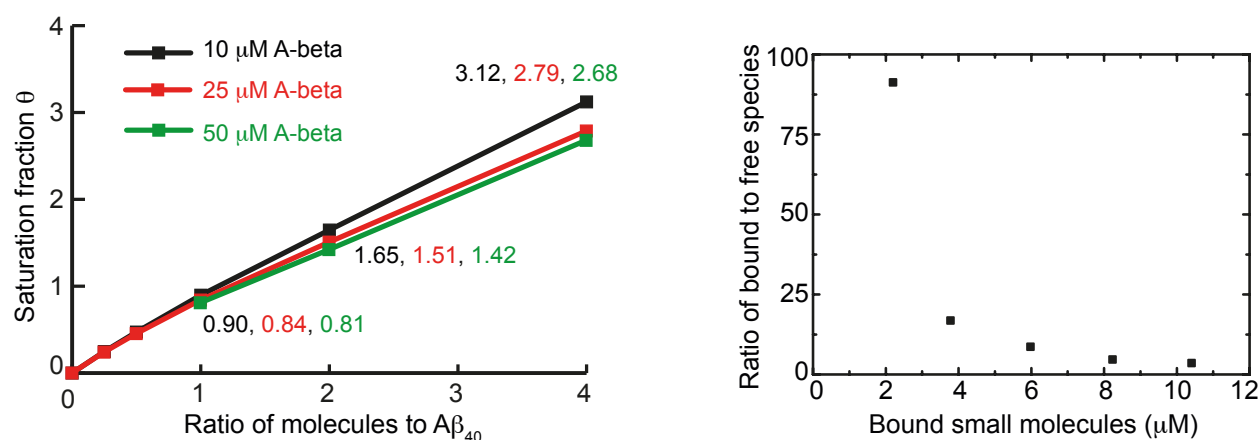
Figure 45: Left, titration of bithiazole-like molecule to the pre-formed $A\beta_{40}$ fibrils for determination of the fractional saturation θ. Right, Scatchard plot indicates the negative cooperativity. Figures were plotted with UV-vis spectroscopy data.

The partitioning coefficient (P) is applied to predict the distribution of a substance in different environment. By using a lipophilicity measurement, the predicted LogP of bithiazole-like molecule in octanol-phosphate saline solutions was determined in AD brain homogenates[4]. The bithiazole-like small molecule has the favorable combination with Aβ fibrillar aggregates of a nanomolar

---

[4] The nanomolar range binding affinity and LogP value prediction *in vivo* were done by Dr. Behrooz H. Yousefi.

range binding affinity from the *in vivo* data. In addition, a moderate lipophilicity of bithiazole-like molecule allows for high initial uptake and a fast clearance. Due to these properties, bithiazole-like molecule could be a suitable PET imaging marker for amyloid deposits. One question that needs to be figured out in the future research could mainly focus on the considerable inconsistence between the *in vivo* binding affinity and the *in vitro* binding affinity.

4.4 C-detected Experiments to Monitor Chemical Shifts Differences

Briefly, the recombinant Aβ40 peptide was produced by expression from *E. coli* system that were grown in M9 medium supplemented with ^{13}C-glucose and ^{15}NH$_4$Cl. Aβ40 fibrils were prepared in phosphate buffer at physiological condition, subsequently incubated at 37 °C shaker for 12-14 days. A series of two-dimensional and three-dimensional spectra were recorded with a Bruker Avance III 750 MHz spectrometer, equipped with a triple-resonance (^{1}H, ^{13}C, ^{15}N) MAS probe.

Figure 46: 2D ^{13}C–^{13}C PDSD spectrum with the resonance assignment for ^{13}C,^{15}N-labeled Aβ40 fibrils.

In the 2D ^{13}C–^{13}C PDSD spectrum of Aβ$_{40}$ fibrils sample, a single set of chemical shifts was observed and the aliphatic carbon with the linewidths of 120-165 Hz, suggesting that a high degree of conformational homogeneity of the fibrils sample. 3D NCACX and NCOCX experiments were conducted in order to obtain the resonance assignment. Residues at the N-terminus of Aβ$_{40}$ were too dynamic and flexible to be detected in MAS solid-state NMR experiments. However, the signal for the side chain like Nε of Arg5 and the backbone Cα and Cβ of Ser8 in N-terminus were able to be observed from the N–C and C–C correlation spectra. The resonance assignment of the 2D PDSD spectrum for Aβ$_{40}$ fibrils is shown in **Figure 46**.

On the basis of the CS assignment, random coil index (RCI) and secondary structure of Aβ$_{40}$ was predicted by TALOS+ inspection interface.[158] The RCI squared order parameter (RCI-S^2) values for all the assigned resonances range from 0.785 to 0.916 indicating that the C-terminal residues are highly rigid and well-ordered in the fibril structure. Additionally, the RCI-S^2 values decrease from residue Gly25 implying a loop structure formation with slightly higher conformational dynamics in comparison to residues Lys16-Val24 and residues Ala30-Val39. According to the secondary structure prediction of Aβ$_{40}$, residues Lys16-Val24 and residues Ala30-Val39 adopt β-strand conformation (β1 and β2) and residues Gly25-Gly29 form a loop structure that connects the two β-sheet strands through the side-chain interactions.
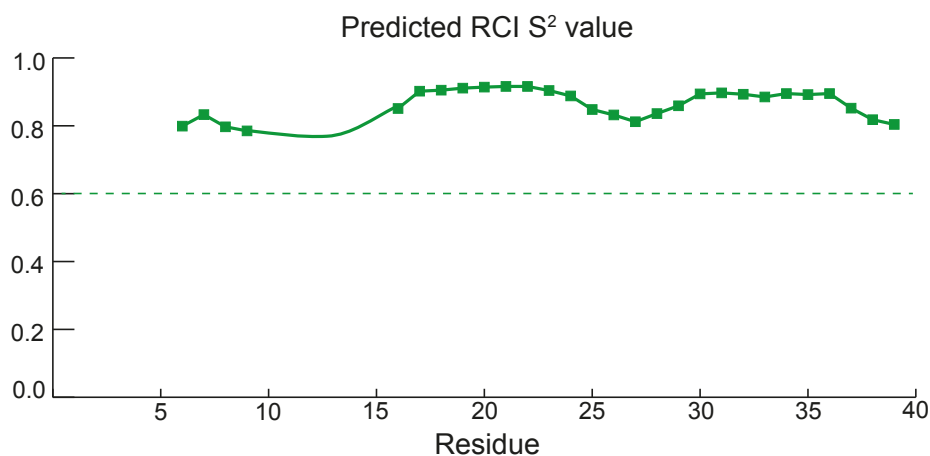
Figure 47: Random coil index prediction by TALOS+ database system, with squared order parameter values (RCI-S^2) prediction by the assignment of Aβ$_{40}$ fibrils. RCI-S^2 scales between 0 (total disorder) and 1 (fully rigid), in which residues below the threshold ≤0.6 are assigned as dynamic.
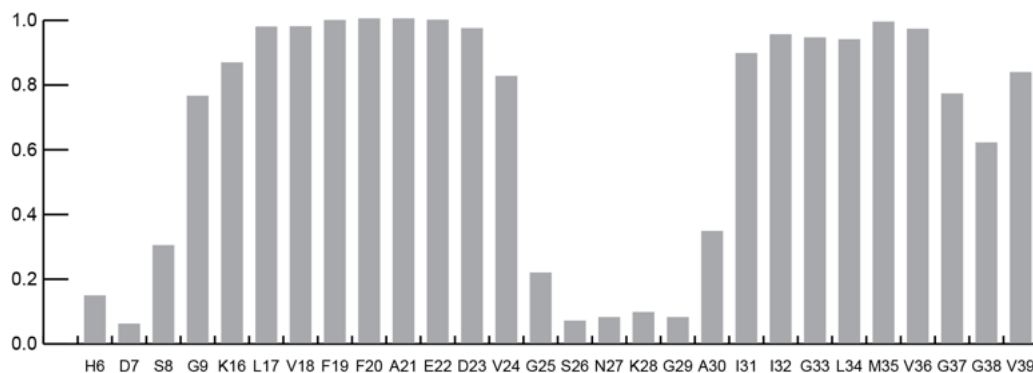
Figure 48: Secondary structure prediction for Aβ₄₀ fibrils by TALOS+ database system. The height of the bars indicates the probability assigned by β-sheet structure. For details of the TALOS+ interface, see reference 158 or see TALOS+ webpage https://spin.niddk.nih.gov/bax/nmrserver/talos/.
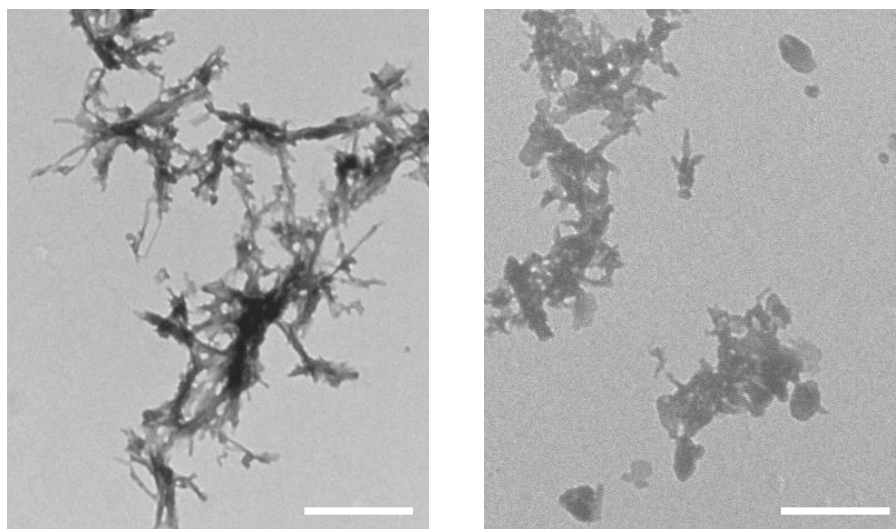
Figure 49: TEM images of Aβ₄₀ fibrils (left) and 4-fold molar excess of bithiazole-like molecule induced Aβ₄₀ fibrils (right). The scale bar is 500 nm.

To monitor the interactions between bithiazole-like molecule and the pre-formed Aβ₄₀ fibrils, 2D ^{13}C–^{13}C correlation PDSD spectra and ^{15}N–^{13}C correlation NCA spectra were recoded with one-fold, two-fold and four-fold molar excess of unlabeled bithiazole to uniformly ^{13}C, ^{15}N-labeled Aβ₄₀ fibrils, respectively. The C–C and N–C correlation spectra were quite overlaid and very similar, indicating that the addition of the small molecules had no dramatic impacts on the fibrils structure. Meanwhile, TEM images confirmed that no significant differences in the morphology of the bithiazole-induced fibrillar aggregates. There was no linewidth broadening and peak

splitting in the NMR spectra suggesting the binding interactions between bithiazole-like small molecule and Aβ40 fibrils was specific. According to the PDSD spectra, the tiny CSPs can be observed in residues Ile31, Ile32 and Val36. These hydrophobic residues could form hydrophobic clusters in the β2 strand and provide enough space for binding sites. Furthermore, the interactions between PiB small molecule and the pre-formed Aβ40 fibrils were investigated as well. Similarly, only small chemical shifts changes were observed. This observation that only tiny CSPs could be explained in two aspects. On one hand, several peaks showing CS differences or peak intensity decrease, are not possible to assign. On the other hand, although the PET tracer binding interactions induce the chemical environment changes for Aβ, ^{13}C and ^{15}N are not sensitive enough to show large chemical shifts differences in comparison with ^{1}H. However, it should be noted that the CSPs are larger in the experiments which sulindac sulfide has been added to Aβ40 fibrils.[159]
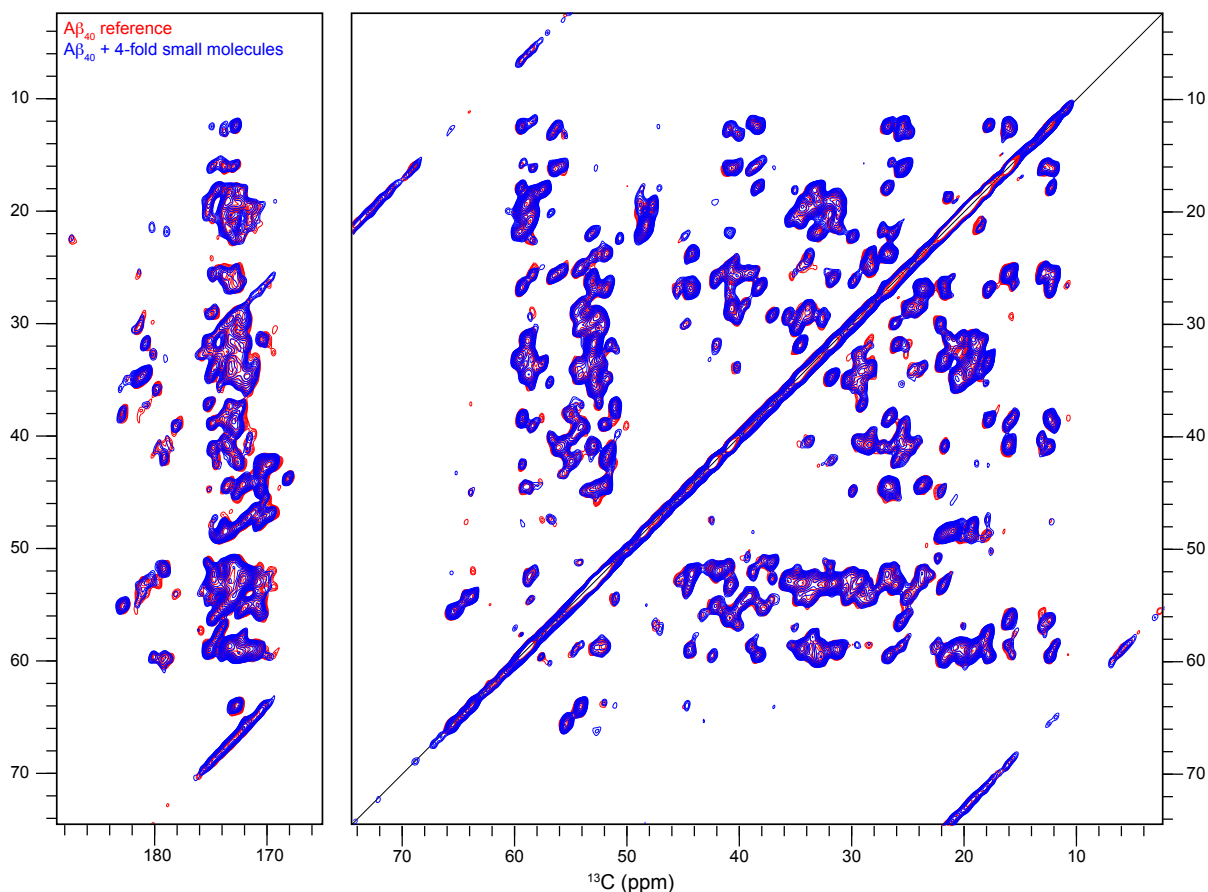
Figure 50: Superposition of 2D $^{13}C-^{13}C$ PDSD spectra of $^{13}C,^{15}N$-labeled Aβ40 fibrils and 4-fold molar excess of bithiazole-like molecule induced Aβ40 fibrils. The spectra were acquired on a Bruker Avance III 750 MHz spectrometer at 273 K and 10 kHz MAS rate with a 50 ms mixing time.
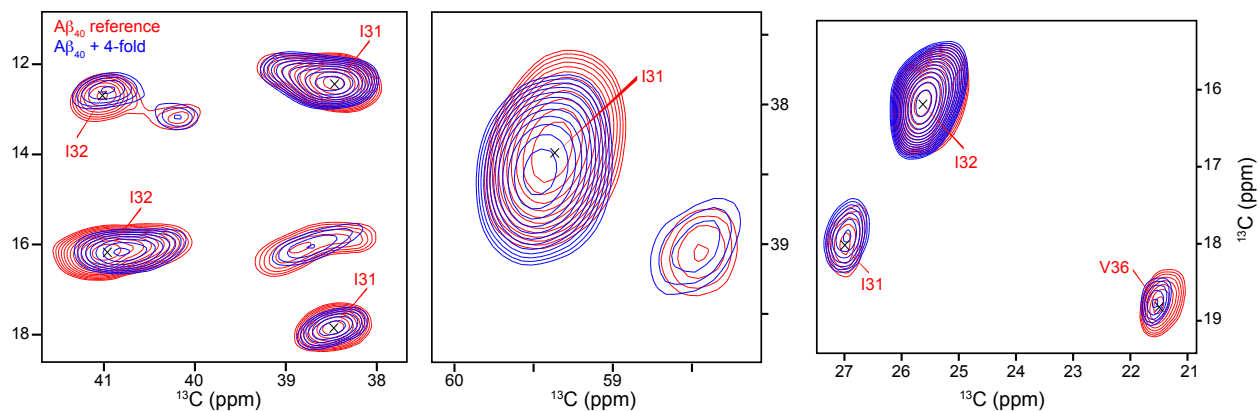
Figure 51: Zoom of the aliphatic region of $^{13}C,^{15}N$-labeled Aβ₄₀ fibrils in the absence and presence of 4-fold molar excess of bithiazole-like molecule. Small CSPs were observed for several residues.
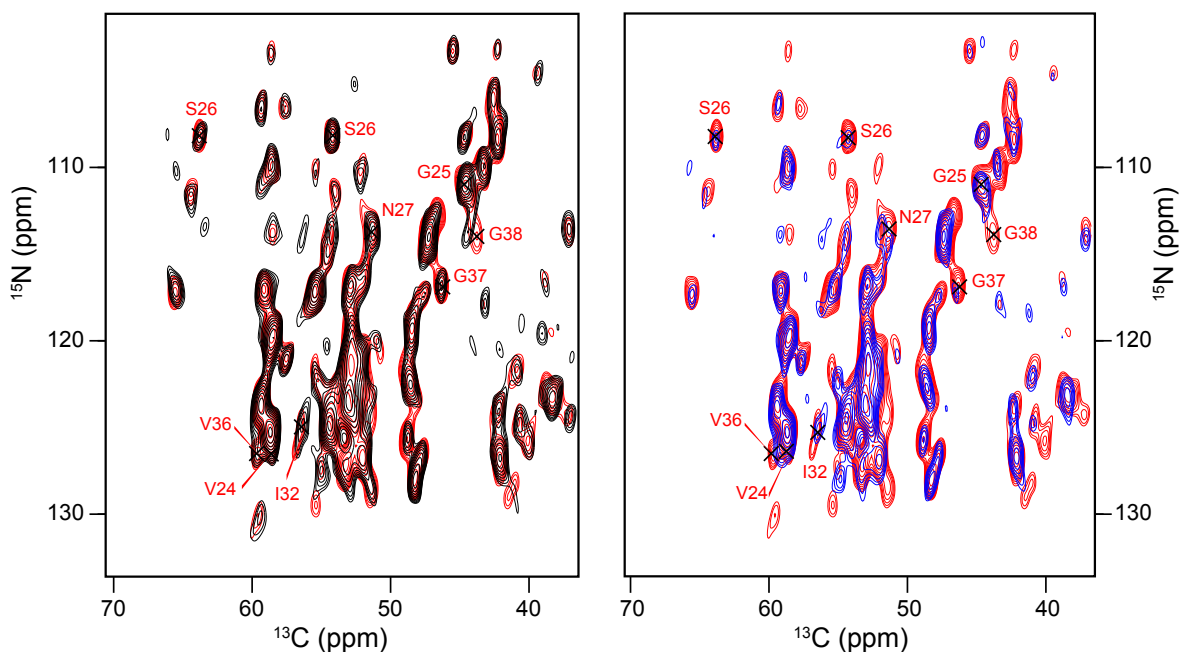
Figure 52: Superposition of 2D $^{15}N–^{13}C$ correlation spectra of $^{13}C,^{15}N$-labeled Aβ₄₀ fibrils, Aβ₄₀ fibrils mixed with 1-fold molar mass amount of bithiazole-like molecule (black) and Aβ₄₀ fibrils mixed with 4-fold molar mass amount of bithiazole-like molecule (blue) on a Bruker Avance III 750 MHz spectrometer at 273 K and 10 kHz MAS rate and processed with the identical parameters.
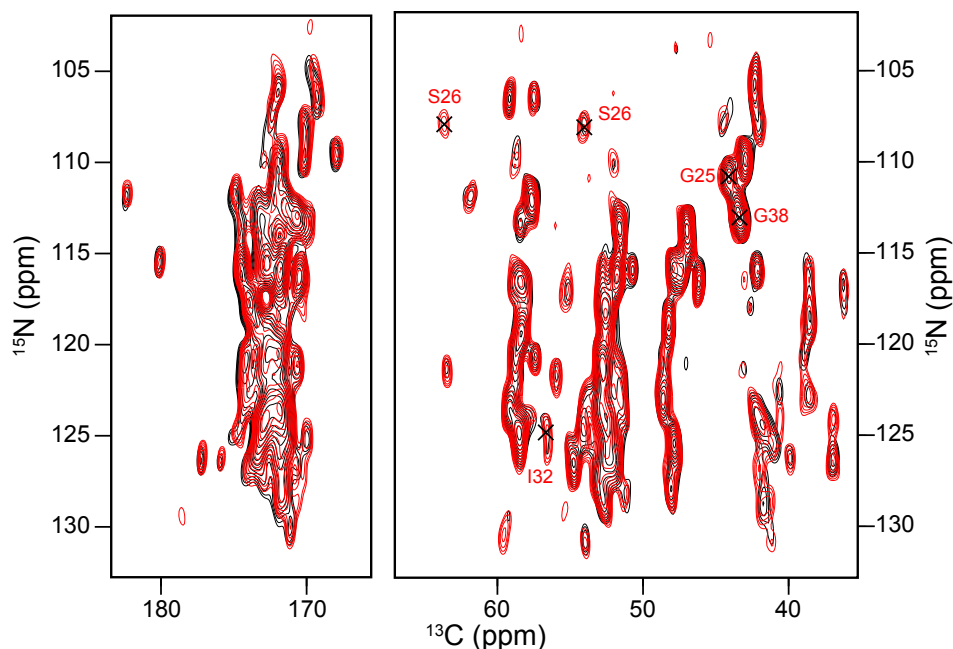
Figure 53: Superposition of 2D ^{15}N–^{13}C correlation spectra of $^{13}C,^{15}N$-labeled Aβ$_{40}$ fibrils and equimolar amount of PiB induced Aβ$_{40}$ fibrils.

In the superposition of the 2D N–C correlation spectra, CS differences in residues Asn27, Ile32, Val36, Gly37 and Gly38 and peak intensity decrease in residues Ser26, Asn27 and Gly38 can be detected. The hydrophobic cluster in segment Val36-Gly38 is able to present enough space for the binding sites, whereas the loop region is unbelievable to present the location for the binding. On one hand, there is no proper location for the occurrence of the binding interactions inside the loop region due to the repulsion interaction between the hydrophilic residues in the loop region and the hydrophobic small molecules. On the other hand, the environment outside the loop region is surrounded by water molecules, and it is also impossible for the binding interactions. Therefore, we speculate that the clear CSPs in the loop region could be attributed to the structural conformational rearrangement in fibrils owing to the chemical exchange process. Upon addition of small molecules to the pre-formed fibrillar aggregates, the protein undergoes a conformational change due to the binding interactions with several specific residues or segment further to lead to CS and signal intensity changes in the loop region. We assume that the PET tracer molecules might be able to induce subtle structural differences or conformational changes of the loop region. To support the speculation, the corresponding TEDOR spectra were recorded to check if the salt-bridge is still present in the bithiazole-induced fibrils. The salt-bridge is formed by the charged sidechains in the loop region and functioned to stabilize the structures.
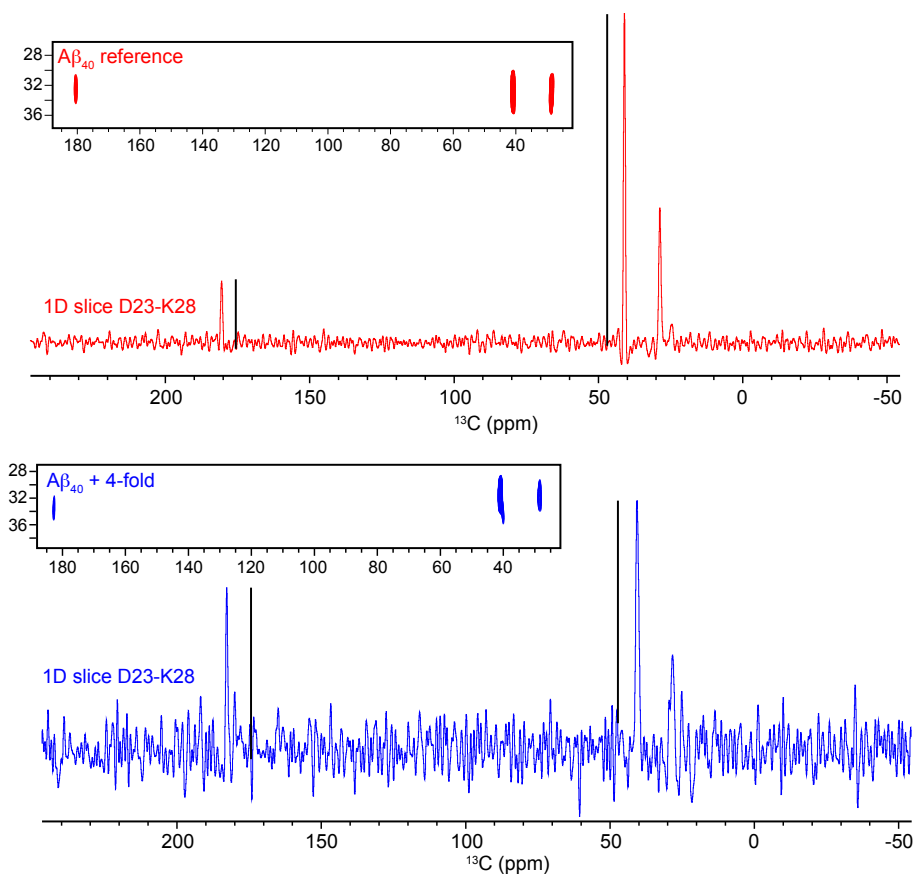
Figure 54: 2D ^{15}N–^{13}C TEDOR spectra with a 15 ms mixing time for reference fibrils (top) and bithiazole-like molecule induced Aβ aggregates (bottom).

A long-range correlation contact between Nζ of Lys28 and the carboxylic carbon of Asp23 were detected in both Aβ₄₀ fibrils reference sample and small molecule induced Aβ₄₀ aggregates, indicating that the salt bridge was still present in the bithiazole-like molecule induced Aβ aggregates. The relative intensities of the long range NH₃–COO⁻ cross peak appeared to be even larger in the Aβ-bithiazole complex, implying that this structure was even more compact. This provides evidence of the structural changes in the loop region, which is consistent with the observation of CSPs in this segment.

4.5 H-detected Experiments to Monitor Chemical Shifts Differences

Proton (^1H) is a sensitive nucleus and usually yields sharp NMR signals in comparison with carbon (^{13}C) and nitrogen (^{15}N). Triple labeled ^2H, ^{13}C, ^{15}N-Aβ₄₀ fibrils with and without equimolar amount of unlabeled bithiazole were packed into a 1.3 mm MAS rotor, respectively. CSPs were

observed for several specific residues from HSQC spectra, which confirms the presence of the specific binding interactions. Hitherto, all the C-detected and H-detected MAS solid-state NMR experiments were discussed above in order to observe the nuclei belong to Aβ40 peptide. Conversely, ligand-based NMR experiment can be envisioned to monitor the interactions from the perspective of the PET tracer molecules. As such, ^{13}C-labeled methyl group of PiB was synthesized to probe the interactions between Aβ40 fibrils and PET-tracer molecule.
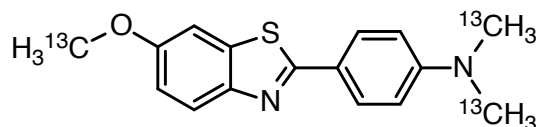
Figure 55: Structure of ^{13}C-labeled PiB, the dimethylamine as well as the methoxy group were ^{13}C labeled.
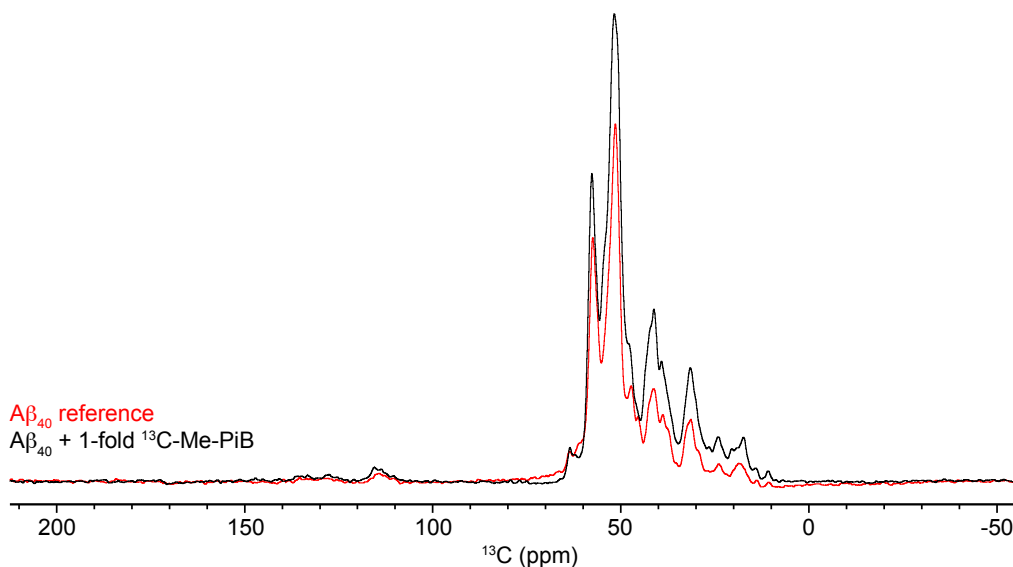
Figure 56: Superposition of 1D ^{13}C SPECIFIC CP spectra of ^{2}H, ^{13}C, ^{15}N-labeled Aβ40 reference fibrils and equimolar amount of ^{13}C-Me-PiB induced Aβ40 fibrils.

From the perspective of the small molecule, either CSP or the linewidth broadening could be applied to provide the evidence of the molecular level binding interactions. To identify the CS of the small molecule, 1D ^{1}H and ^{13}C solution-state NMR spectra of ^{13}C-Me-PiB were acquired firstly. The ^{13}C and ^{1}H signal of methoxy group is with the CS of ~56 ppm and ~3 ppm, respectively. Concerning the *N*-methyl group, the CS of carbon and hydrogen disperse at ~40 ppm and ~4 ppm, respectively. To evaluate the sample quality, 1D MAS solid-state NMR spectra (**Figure 56**) were

recorded for deuterated Aβ₄₀ fibrils in the absence and presence of ¹³C-Me-PiB. The high resolution and sensitivity spectra were allowed to do the further analysis. A set of 3D experiments were conducted on a Bruker Avance III 800 MHz spectrometer at 52 kHz MAS rate to perform the sequential resonances assignment of deuterated Aβ₄₀ fibrils with and without equimolar amount of ¹³C-Me-PiB, including hCANH, hCONH, hcoCAcoNH and hcaCBcaNH experiments.
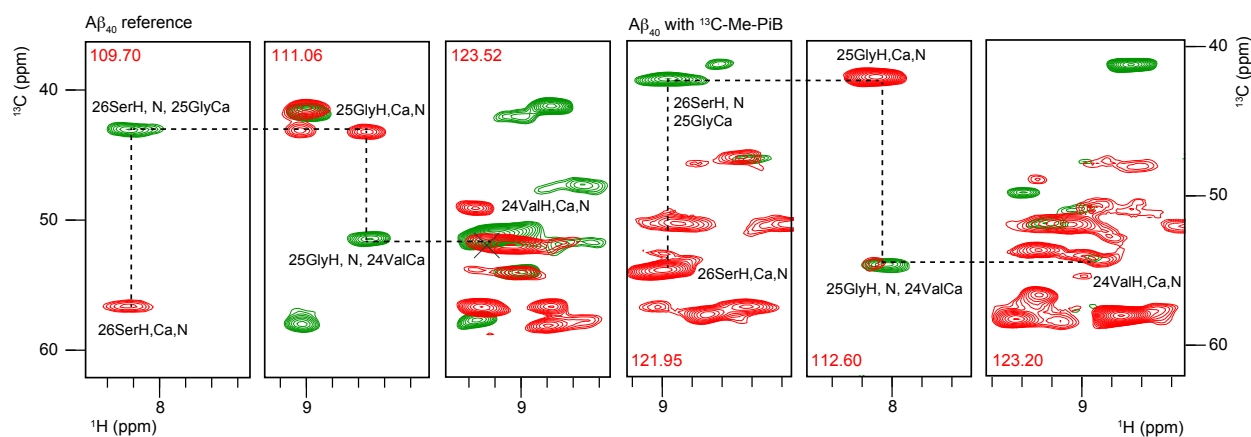
Figure 57: Strip plots of both inter- and intra-residue Cα resonances of Aβ₄₀ fibrils and equimolar amount of ¹³C-Me-PiB induced Aβ₄₀ fibrils. Red spectrum indicates hCANH and green indicates hcoCAcoNH.
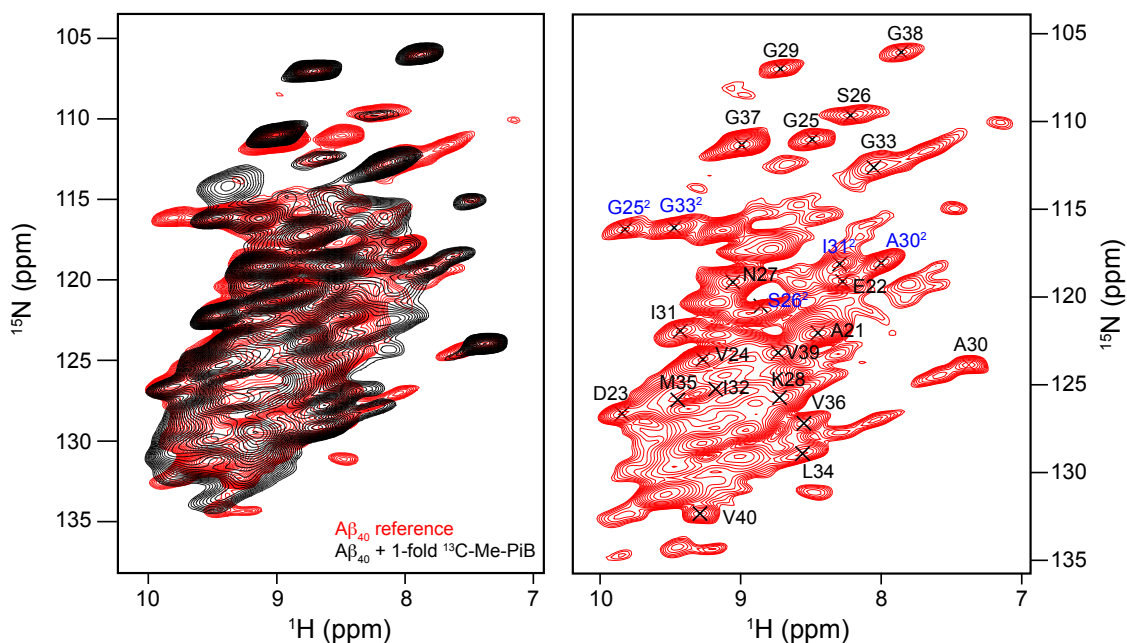
Figure 58: Left, superposition of 2D ¹H–¹⁵N correlation spectra of ²H, ¹³C, ¹⁵N-labeled Aβ₄₀ reference fibrils and equimolar amount of ¹³C-Me-PiB induced Aβ₄₀ fibrils. Right, the residue assignment of Aβ₄₀ reference fibrils.
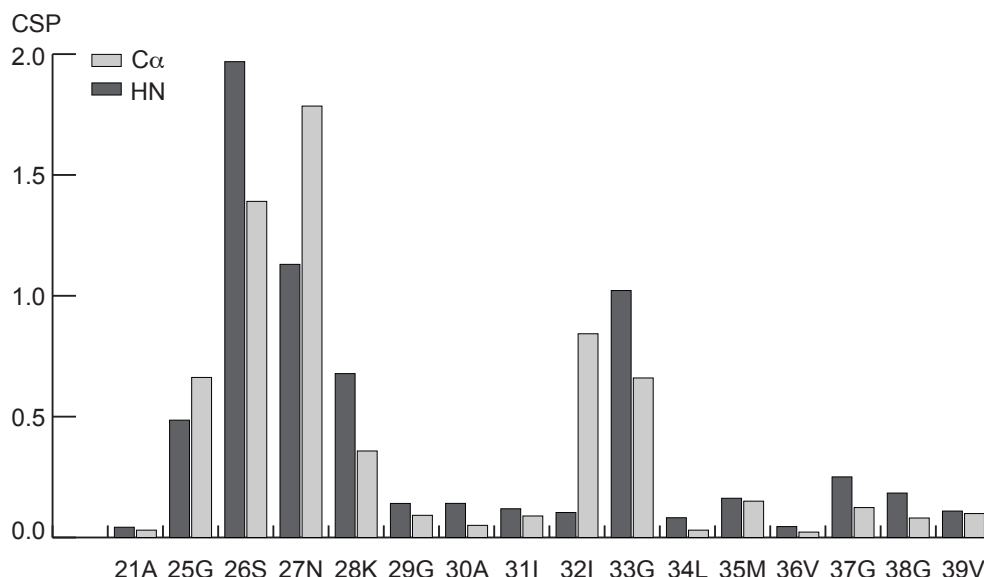
Figure 59: Chemical shifts differences (Δδ) for ^1H, ^{15}N and ^{13}C resonances of ^2H, ^{13}C, ^{15}N-labeled Aβ$_{40}$ fibrils in the absence and presence of equimolar amount of ^{13}C-Me-PiB, according to $\Delta\delta_{C\alpha} = \sqrt{(\delta H^N_{A\beta-PiB} - \delta H^N_{A\beta})^2 + \frac{(\delta C\alpha_{A\beta-PiB} - \delta C\alpha_{A\beta})^2}{4}}$ and $\Delta\delta_{NH} = \sqrt{(\delta H^N_{A\beta-PiB} - \delta H^N_{A\beta})^2 + \frac{(\delta N_{A\beta-PiB} - \delta N_{A\beta})^2}{25}}$.

After the treatment of PiB to Aβ$_{40}$ fibrils, clear CSPs were presented at residues Gly25, Ser26, Asn27 that are located in loop region and residues Val36 and Gly37 that are located in the β2 strand, which is consistent with the C-detected experiments. From the perspective of PiB, the chemical shifts changes, linewidth broadening or peak splitting for itself was supposed to be observed from the H−C correlation spectrum. Although, the sensitivity and resolution are higher in H−C correlation spectra in comparison to H−N correlation spectra, we cannot detect any proton signals of the methyl groups from PiB. 2D H−C spectra with the 1D projection of solution-state NMR spectra for the small molecules are shown in **Figure 62**, in which the blue circles are marked the region of *N*-methyl and methoxy group for PiB. Similarly, the proton signals of the methyl-group for a protonated microcrystalline sample only can be observed and assigned when the MAS rotation frequency is beyond 90 kHz.[160] Therefore, a 52 kHz of MAS rotation frequency in the H−C correlation experiment maybe not high enough to detect the signals of the methyl-group protons in the fully protonated ^{13}C-Me-PiB. Apart from the MAS rotation frequency, the not very well-defined bindings sites induced the exchangeable binding sites for free PiB, further to lead to the proton linewidth broadening in NMR spectra. The suppression of the free PiB resonance caused the invisible signals of proton on the methoxy group. **Figure 60** illustrated the exchanging process

of free PiB with two groove binding sites on the basis of the molar ratio of 1:1 for PiB to Aβ$_{40}$ fibrils.
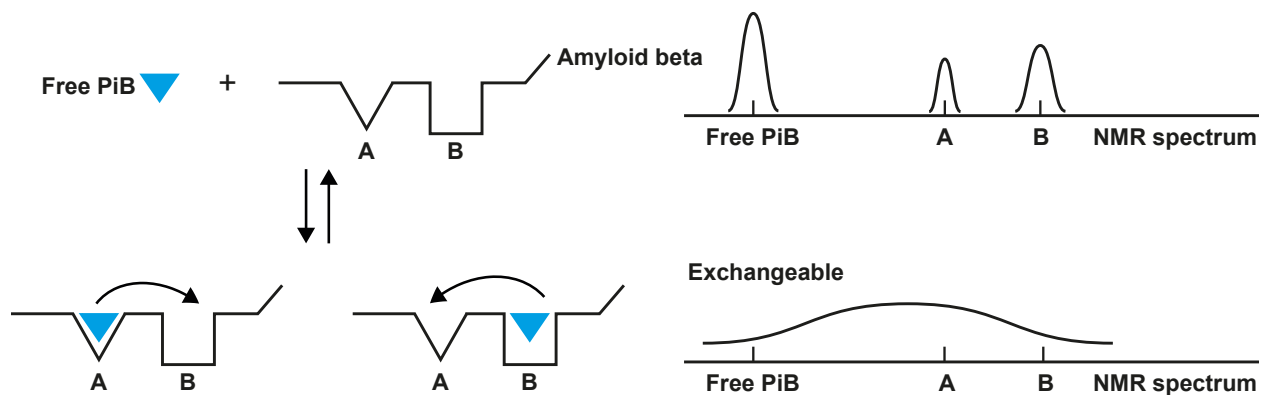
Figure 60: The schematic diagram of the binding interaction of Aβ$_{40}$ with equimolar amount of PiB. A and B represents the two potential groove structures in Aβ$_{40}$ hydrophobic region that could be able to provide enough spaces for binding interactions.
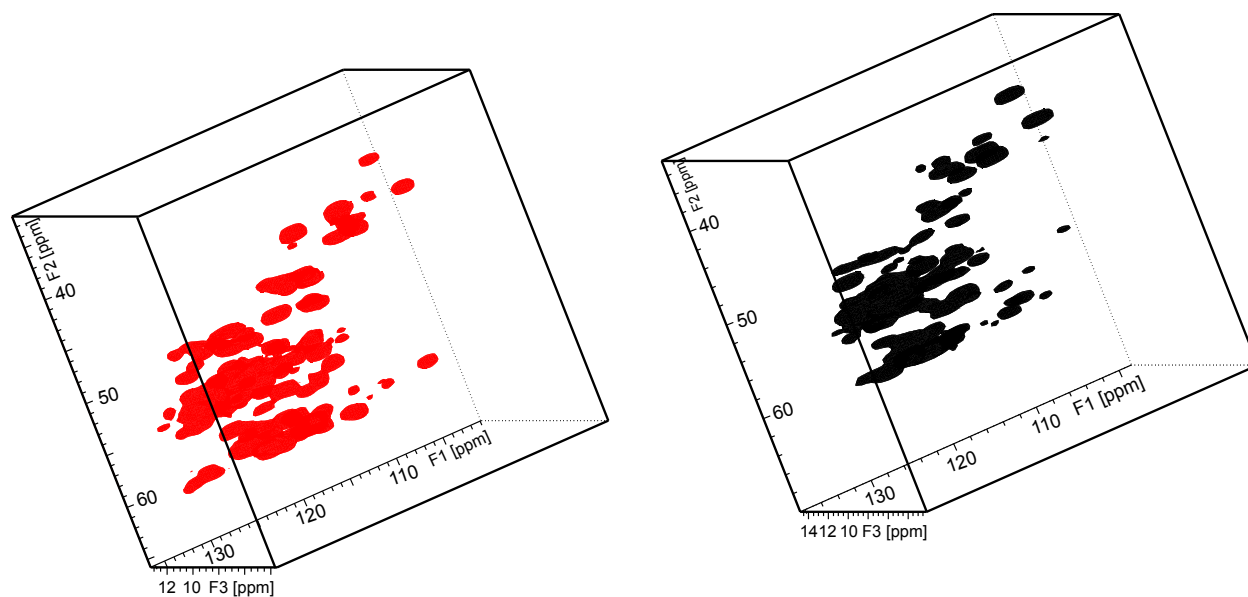
Figure 61: 3D cube of hCANH experiments for reference fibrils (left) and equimolar amount of ^{13}C-Me-PiB induced Aβ$_{40}$ aggregates (right).
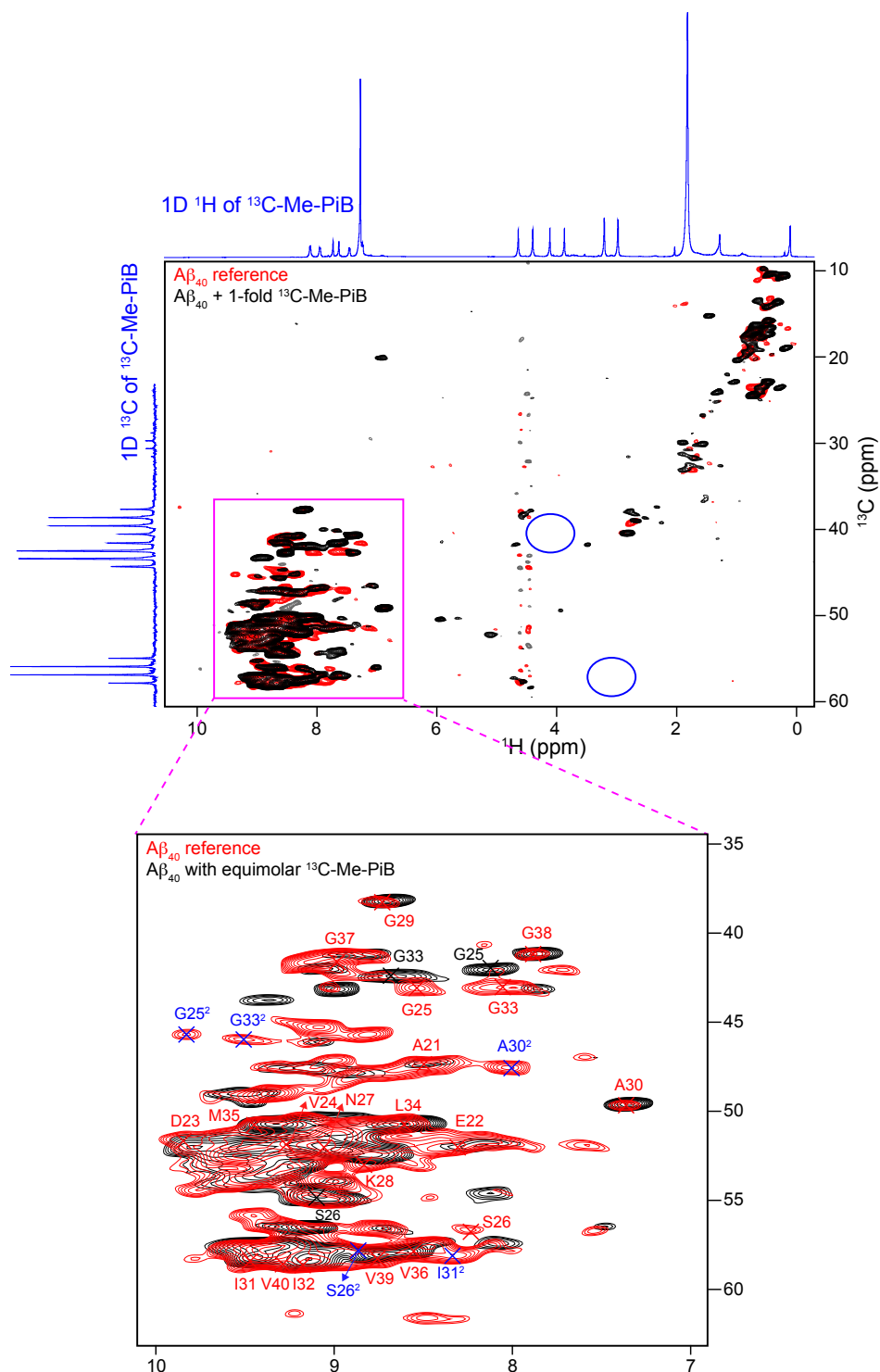
Figure 62: Superposition of 2D $^1H-^{13}C$ correlation spectra of ^2H, ^{13}C, ^{15}N-labeled Aβ40 reference fibrils and equimolar amount of ^{13}C-Me-PiB induced Aβ40 fibrils. The 1D projection spectra were for ^{13}C-Me-PiB small molecule in deuterated chloroform solvent. The blue color circles mark the cross peak of H−C contacts in methoxy and N-Me groups for ^{13}C-Me-PiB.

To our surprise, the CSPs in the loop region of the deuterated fibrils sample (backbone was substituted with 99% deuterium at exchangeable sites) is larger in comparison to a fully protonated fibrils sample. In order to resolve the discrepancy, the deuterium isotope effects on the structural differences of Aβ₄₀ fibrils before and after the treatment of PiB were identified (**Figure 63**). There is no correlation between protonated fibrils and deuterated fibrils in secondary structure of Cα and N for the nuclei assigned in both isotopic labeling fibrils. Hence, we conclude that the PiB small molecule induced the structure and dynamics changes of the deuterated fibrils. It seems that the backbone deuteration exchange increases the flexibility of the fibrils structure in comparison with the protonated fibrils. Upon addition of PiB, the structure of the deuterated fibrils is stabilized due to the binding interactions of PiB and shows less dynamic which indicates a stronger binding affinity.
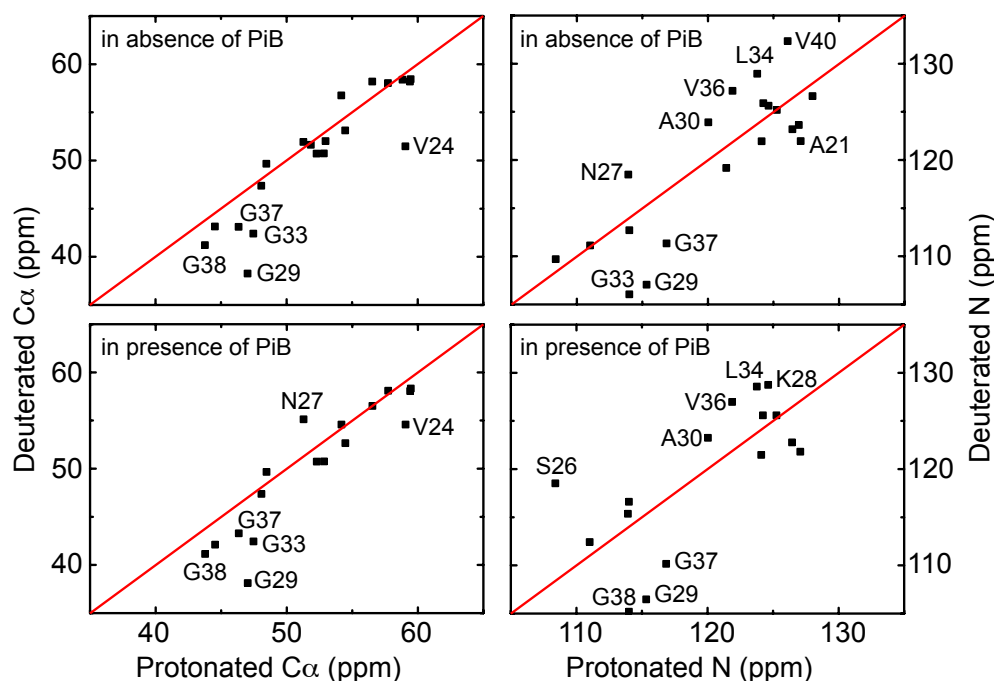
Figure 63: Secondary chemical shift correlation for Cα and N chemical shifts for protonated Aβ₄₀ fibrils and deuterated Aβ₄₀ fibrils in the absence and presence of equimolar amount of PiB.

The atomic level structural models for Aβ fibrils[119] are illustrated in **Figure 64** to present the potential binding sites for small molecules. In the two-fold symmetric Aβ₄₀ fibril structural model (**Figure 64**, left), three hydrophobic cavities formed in the rigid region could be able to bury a small molecule, including the groove structure at residue Gly33, hydrophobic core at residues

Gly37-Gly38 and the C-terminal region. A small molecule could either locate onto the groove structure formed by residue Gly33 facing to the residues Phe19, Leu34, and Val36, or orientate in a way that contacts with residues Val36 and Val40. Apart from these hydrophobic clusters, a polar cavity formed by the residues in the flexible loop or turn region might be another suitable binding site. However, due to its hydrophilic nature, this polar cavity is unlikely to bind with a hydrophobic small molecule.

In a similar way, Aβ$_{42}$ fibrils structure derived from solid-state NMR restraints[122] could be applied as another model to provide information on the binding interactions. Several cavities in this structural model (**Figure 64**, right) could also be proposed as the potential binding sites for small molecule binding interactions. In the hydrophobic clusters, a small molecule could either locate onto the surface of Gly33 groove structure so that the molecule may orientate itself facing to the residues Leu17, Ile32, and Leu34, or locate to the opposite side of the groove structure contacting with residues Ile31, Val36 and Val39. Inside the flexible turn region formed by residues Glu22-Ser26 could provide an option to bury a hydrophilic small molecule. Based on the two PDB structural models discussed above, we propose that the possibilities for the locations of PET tracer small molecules onto the fibrillar aggregates. The location of the binding sites and the orientation of the small molecule onto the fibrils need to be further confirmed by a molecular docking experiment.

Figure 64: PDB structural models with residues for Aβ$_{40}$ (left, adapted from PDB-2LMN) and Aβ$_{42}$ (right, adapted from PDB-5KK3).

4.6 Summary and Outlook

The work discussed in this chapter is mainly designed to characterize the interactions between Aβ₄₀ fibrils and PET tracer molecules and to obtain the structural information of Aβ-PET tracer complexes at the atomic level by using MAS solid-state NMR. In this project, highly pure monomeric Aβ₄₀ peptide was expressed in *E. coli* system and purified with HPLC methods. In order to monitor the CS differences by MAS solid-state NMR, the small molecule needs to be dissolved in the physiological aqueous environment and bound with fibrils. Considering the hydrophobic nature of the small molecules used in this chapter, a solid-state NMR titration system was established through BSA carrier to transfer the small molecules to fibrillar aggregates. Through the preliminary characterization, the titration protocol works in the proposed way. However, the C-detected spectra are quite overlaid, and the CSPs are not large as what we expect after treatment of PET small molecules. Apart from the C-detected spectra, CSPs from the loop region and the hydrophobic cluster of Aβ₄₀ fibrils are observed by H-detected experiments. The hydrophobic cluster, especially the groove at residue Gly33 and the hydrophobic core at residues Gly37-Gly38,[24,121] could provide enough space for the binding interactions. In addition, the CSPs are observed as well as in the loop region. Since the small molecules used are quite hydrophobic and it is difficult to locate or bind to the segment in which the residues are hydrophilic and exposed to the solvent environment. As the PET small molecules could introduce either subtle structural changes or conformational rearrangement, that it the reason why the CSPs can be detected in the flexible loop region. Furthermore, on the basis of secondary chemical shift correlation, PiB small molecule causes the structure and dynamics changes of the deuterated fibrils, particularly in the C-terminus. More specifically, the backbone deuteration exchange increases the flexibility of the fibrils structure. Upon addition of PiB, the binding interaction with a stronger binding affinity is induced to stabilize the structure of the deuterated fibrils.

Further studies regarding to this research could be divided into two aspects. First, to deeply study how the purification methods and seeds impact on the amyloid polymorphism, the sequential assignment and distance restraints need to be collected by using MAS solid-state NMR. More detailed information at the atomic level of fibrils structure and better understanding about the amyloid morphism should be integrated into the future research targets. Second, we speculate the potential binding sites for PET tracer molecules on the basis of two PDB structural models. Docking experiment could be a good supplementary method to support the speculation and provide

insights into the binding mechanism. To fulfill docking experiment, Aβ₄₀ fibrils structure with atomic resolution is needed. Preliminary experiments like proton assisted recoupling (PAR) and CHHC (**Figure 65**) with different mixing time were recorded to obtain distance restraints. Furthermore, a uniformly labeled fibrils sample which is diluted by natural abundance fibrils needs to be prepared to provide more information on distance contacts, further to determine the fibrils structure at the atomic level.
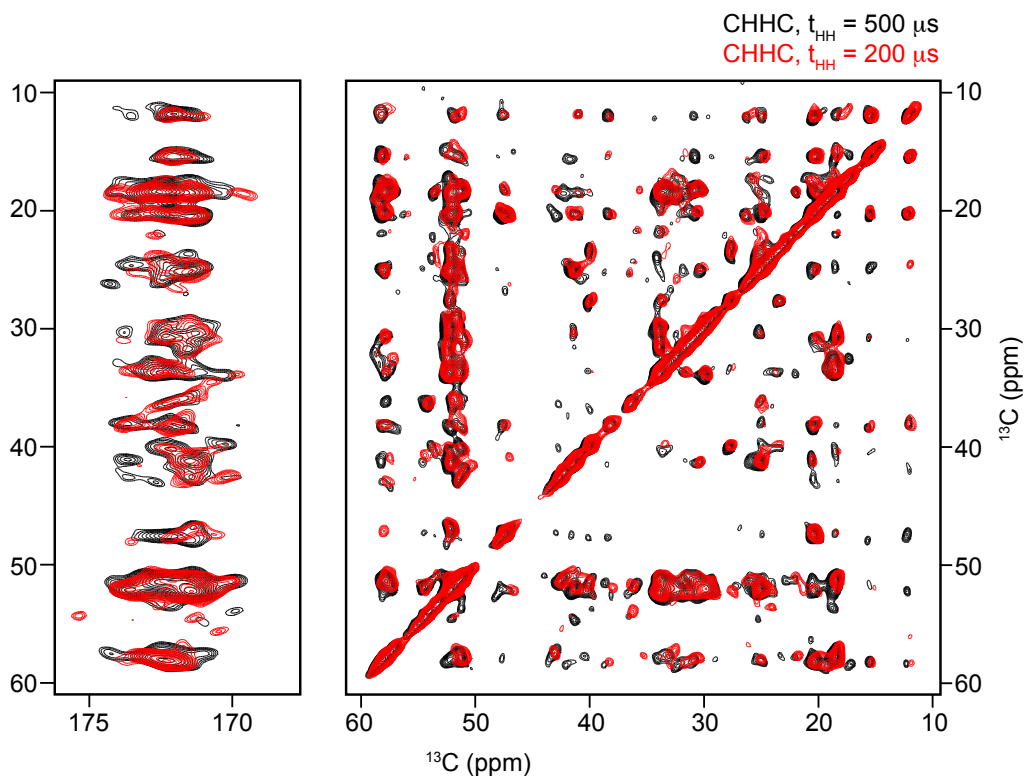
Figure 65: Superposition of 2D CHHC spectra of ¹³C, ¹⁵N-labeled Aβ₄₀ fibrils with different homonuclear contact time on a Bruker Avance III 750 MHz spectrometer at 273 K and 10 kHz MAS rate.

Abbreviations

Abbreviation	Full name description
Aβ	Amyloid-β peptide
Ach	acetylcholine
ACN	acetonitrile
AD	Alzheimer's disease
AFM	atomic force microscope
APP	amyloid precursor protein
BSA	bovine serum albumin
CP	cross polarization
CSA	chemical shift anisotropy
CSP	chemical shift perturbation
CV	column volume
Da	Dalton
DIC	differential interference contrast
DLS	dynamic light scattering
DMSO	dimethyl sulfoxide
DOSY	diffusion ordered spectroscopy
EDTA	ethylenediaminetetraacetic acid
EGCG	epigallocatechin-3-gallate
FDA	Food and Drug Administration
Fluos-ISMs	N$^{\alpha}$-amino-terminal fluorescein-labeled ISMs
HFIP	hexafluoroisopropanol
HPLC	high-performance liquid chromatography
HSQC	heteronuclear single quantum coherence
IAPP	islet amyloid polypeptide
IPTG	isopropyl β-D-1- thiogalactopyranoside
ISMs	Interaction surface mimics
LB	Luria broth
mAbs	monoclonal antibodies
MAS	magic angle spinning

Continued:

Abbreviation	Full name description
MCI	mild cognitive impairment
MPL	Mass per length
NFT	neurofibrillary tangles
NMDA	N-methyl-D-aspartate
NP	neuritic plaques
NOESY	nuclear overhauser effect spectroscopy
NSAIDs	nonsteroidal anti-inflammatory drugs
NUS	non-uniform sampling
OD	optical density
PAGE	polyacrylamide gel electrophoresis
PAR	proton assisted recoupling
PDSD	proton-driven spin diffusion
PET	positron emission tomography
PiB	Pittsburgh compound B
RAR	Retinoid A receptor
RCI	Random coil index
RFDR	radio frequency-driven recoupling
ROS	reactive oxygen species
RPC	reverse phase chromatography
RT	room temperature
RXR	Retinoid X receptor
SEC	size exclusion chromatography
SDS	sodium dodecyl sulfate
STD	saturation transfer difference spectroscopy
TEM	transmission electron microscopy
TFA	trifluoroacetic acid
ThT	thioflavin-T
UV-vis	Ultraviolet-visible

Chemical shifts assignment for R3-GI peptide, major conformer

aa	H	Hα	Hβ	Hγ	Hδ	additional H	Cα	Cβ	Cγ	Cδ
A1	-	3.963	1.007	-	-	-	-	-	-	-
T2	7.979	3.772	-	0.873	-	-	-	-	-	-
Q3	8.423	3.966	1.637 1.720	2.016	-	7.326 6.650	-	-	-	-
R4	8.317	3.939	1.393 1.446	1.228 1.267	2.793	-	-	-	-	-
L5	8.163	3.991	1.228 1.299	-	0.523 0.583	-	51.956	39.268	24.051	20.338 21.906
A6	8.114	3.853	0.961	-	-	-	49.721	16.154	-	-
N7	8.073	4.239	2.380	-	7.359 6.622	-	-	-	-	-
F8	7.815	4.212	2.706 2.794	-	-	6.995 6.880	55.018	36.398	-	-
L9	7.808	3.913	1.095 1.232	-	0.487 0.545	-	52.181	39.276	23.792	20.468 21.979
V10	7.705	3.600	1.631	0.494 0.566	-	-	59.650	29.675	17.900	-
H11	8.080	4.255	2.679 2.752	-	6.653	7.517	-	-	-	-
R12	8.273	3.918	1.378 1.461	1.307	2.800	6.949	-	-	-	-
R13	8.273	3.920	1.430 1.491	1.207 1.253	2.810	6.910	-	-	-	-
R14	8.220	3.923	1.477 1.401	-	2.809	6.911	-	-	-	-
N15	7.967	4.319	2.340 2.388	-	6.644 7.356	-	-	-	-	-
F16	7.968	4.319	2.616 2.735	-	7.358	6.910	-	-	-	-
G17	2.647	3.664 3.737	-	-	-	-	-	-	-	-
A18	7.986	4.371	0.954	-	-	-	-	-	-	-
I19	2.773	4.370	1.710	0.531 0.644 1.029	0.481	-	-	-	-	-
L20	8.233	4.052	1.227 1.316	-	0.485 0.531	-	51.917	38.927	23.989	19.915 21.800
S21	8.045	4.051	3.491 3.539	-	-	-	55.031	60.835	-	-

Chemical shifts assignment for R3-GI peptide, minor conformer

aa	H	Hα	Hβ	Hγ	Hδ	additional H
N7	8.054	-	-	-	-	-
F8	-	4.222	-	-	-	-
L9	7.841	3.952	1.101 1.233	-	0.463 0.521	-
V10	7.665	3.642	1.551	0.354 0.468	-	-
H11	8.324	4.291	2.661 2.795	-	6.679	7.491
N15	8.201	4.290	2.302 2.357	-	7.347	-
F16	7.856	4.584	2.540 2.661	-	-	6.994 6.861
G17	2.544	3.751 3.938	-	-	-	-
A18	8.274	4.384	0.969	-	-	-
I19	2.756	4.384	1.651	0.439	0.355	-
L20	8.130	4.296	-	-	0.499 0.565	-
S21	8.129	4.050	3.456 3.503	-	-	-

Chemical shifts assignment for G3-GI peptide, major conformer

aa	H	Hα	Hβ	Hγ	Hδ	additional H
A1	-	3.959	1.005	-	-	-
T2	7.926	3.772	-	0.872	-	-
Q3	8.408	3.962	1.636 1.717	2.011	-	7.320 6.647
R4	8.306	3.943	1.387 1.442	1.225 1.262	-	-
L5	8.162	3.993	1.225 1.295	-	0.524 0.583	-
A6	8.108	3.854	0.957	-	-	-
N7	8.059	4.240	2.363	-	7.341 6.607	-
F8	7.801	4.209	2.692 2.780	-	-	6.987 6.870
L9	7.824	3.954	1.104 1.231	-	0.478 0.540	-
V10	7.752	3.654	1.624	0.481 0.547	-	-
H11	8.176	4.256	2.708 2.763	-	6.652	7.448
G12	8.137	3.550 3.603	-	-	-	-
G13	8.069	3.554 3.632	-	-	-	-
G14	8.039	3.529 3.632	-	-	-	-
N15	7.961	3.526	2.208 2.307	-	6.612 7.264	-
F16	7.924	4.307	2.531 2.675	-	-	6.994 6.856
G17	2.640	3.680	-	-	-	-
A18	7.919	4.358	0.948	-	-	-
I19	2.763	4.366	1.703	0.529 0.642 1.026	0.477	-
L20	8.234	4.045	1.224 1.314	-	0.482 0.527	-
S21	8.029	4.348	3.483 3.551	-	-	-

Chemical shifts assignment for G3-GI peptide, minor conformer

aa	H	Hα	Hβ	Hγ	Hδ	additional H
A6	-	3.850	-	-	-	-
N7	8.028	4.230	2.340	-	7.317	-
V10	7.823	3.598	1.520	0.304	-	-
H11	8.349	4.365	2.648 2.863	-	6.660	7.444
N15	8.439	4.535	-	-	-	-
F16	7.929	4.577	-	-	-	6.993 6.858
G17	2.545	3.757 3.979	-	-	-	-
A18	8.265	4.380	0.965	-	-	-
I19	2.750	4.381	1.639	0.427	0.340	-
L20	8.138	4.044	1.219 1.310	-	0.487 0.560	-

Chemical shifts assignment for R3 peptide

aa	H	Hα	Hβ	Hγ	Hδ	additional H
A1	8.230	3.954	1.008	-	-	-
T2	8.001	3.771	-	0.877	-	-
Q3	8.430	3.975	1.636 1.724	2.021	-	7.331 6.656
R4	8.322	3.940	1.391 1.451	1.232 1.276	2.790	-
L5	8.169	3.992	1.233 1.301	-	0.528 0.587	-
A6	8.120	3.858	0.967	-	-	-
N7	8.078	4.245	2.382	-	6.627 7.365	-
F8	7.823	4.216	2.713 2.794	-	-	6.888
L9	7.813	3.915	1.096 1.234	-	0.490 0.547	-
V10	7.708	3.602	1.634	0.497 0.571	-	-
H11	8.086	4.256	2.683 2.761	-	6.660	7.530
R12	8.273	3.920	1.315 1.369	-	-	-
R13	8.240	3.921	1.431 1.496	1.248	-	-
R14	8.242	3.902	-	-	-	-
N15	8.102	4.321	2.356 2.434	-	6.651 7.379	-
F16	8.108	4.195	2.680 2.821	-	7.333	6.907
G17	8.115	3.488 3.549	-	-	-	-
A18	7.809	3.949	1.015	-	-	-
I19	8.004	3.949	1.504	1.015 1.166	0.849	-
L20	8.230	4.077	1.246 1.321	-	0.512 0.552	-
S21	8.015	4.034	3.491 3.545	-	-	-

Chemical shifts assignment for deuterated Aβ$_{40}$ and ^{13}C-Me-PiB induced Aβ$_{40}$ fibrils

aa	H^N	N	Cα	Cβ	CO
A21	8.50	121.96	47.39	18.74	170.02
	8.47	121.81	47.38	-	-
E22	8.30	119.17	52.02	-	171.96
	-	-	-	-	-
D23	9.86	126.64	51.63	35.16	173.22
	-	-	-	-	-
V24	9.27	123.63	51.47	-	171.85
	-	-	54.58	-	171.10
G25	8.52	111.13	43.15	-	173.00
	8.11	112.43	42.11	-	173.45
S26	8.21	109.70	56.76	58.07	170.56
	9.08	118.53	54.59	-	171.80
N27	9.01	118.49	51.94	-	170.49
	8.21	115.37	55.13	-	172.85
K28	8.83	125.63	53.12	30.69	172.44
	9.10	128.74	52.65	-	171.61
G29	8.73	107.06	38.26	-	172.75
	8.65	106.48	38.17	-	171.44
A30	7.38	123.91	49.67	20.48	172.48
	7.33	123.25	49.68	-	171.67
I31	9.46	121.95	58.44	36.09	171.29
	9.39	121.47	58.33	-	-
I32	9.18	125.20	58.21	36.58	171.79
	9.11	125.58	56.53	-	172.76
G33	8.07	112.71	42.42	-	177.20
	8.73	116.61	42.44	-	166.93
L34	8.58	128.95	50.72	43.41	171.91
	8.61	128.57	50.73	-	171.25
M35	9.45	125.90	50.73	32.84	172.19
	9.30	125.59	50.75	-	171.86
V36	8.57	127.19	58.05	29.73	175.48
	8.56	126.97	58.09	-	173.73
G37	9.02	111.34	43.12	-	174.63
	8.93	110.17	43.29	-	169.28
G38	7.88	106.05	41.22	-	175.43
	7.81	105.20	41.14	-	167.79
V39	8.76	123.19	58.21	31.62	174.04
	8.69	122.77	58.07	-	-
V40	9.29	132.34	58.40	-	-
	-	-	-	-	-

Reference

1.   Association, A. 2017 Alzheimer's disease facts and figures. *Alzheimers Dement.* **13**, 325–373 (2017).

2.   Chiti, F. & Dobson, C. M. Protein Misfolding, Amyloid Formation, and Human Disease: A Summary of Progress Over the Last Decade. *Annu. Rev. Biochem.* (2017).

3.   Selkoe, D. J. Alzheimer's Disease: Genes, Proteins, and Therapy. *Physiol. Rev.* **81**, 741–766 (2001).

4.   Mattson, M. P. Pathways towards and away from Alzheimer's disease. *Nature* **430**, 631 (2004).

5.   Chiti, F. & Dobson, C. M. Protein misfolding, functional amyloid, and human disease. *Annu Rev Biochem* **75**, 333–366 (2006).

6.   Blennow, K., de Leon, M. J. & Zetterberg, H. Alzheimer's disease. *The Lancet* **368**, 387–403 (2006).

7.   Goedert, M. & Spillantini, M. G. A Century of Alzheimer's Disease. *Science* **314**, 777–781 (2006).

8.   Selkoe, D. J. Alzheimer's disease is a synaptic failure. *Science* **298**, 789–791 (2002).

9.   Alzheimer's Disease. Available at: https://stanfordhealthcare.org/medical-conditions/brain-and-nerves/alzheimers-disease.html.

10.   Strittmatter, W. J. *et al.* Apolipoprotein E: high-avidity binding to beta-amyloid and increased frequency of type 4 allele in late-onset familial Alzheimer disease. *Proc. Natl. Acad. Sci.* **90**, 1977–1981 (1993).

11.   Gatz, M. *et al.* Role of Genes and Environments for Explaining Alzheimer Disease. *Arch. Gen. Psychiatry* **63**, 168 (2006).

12.   Francis, P. T., Palmer, A. M., Snape, M. & Wilcock, G. K. The cholinergic hypothesis of Alzheimer's disease: a review of progress. 11

13.   Hardy, J. & Allsop, D. Amyloid deposition as the central event in the aetiology of Alzheimer's disease. 6

14.   Mudher, A. & Lovestone, S. Alzheimer's disease – do tauists and baptists finally shake hands? *Trends Neurosci.* **25**, 22–26 (2002).

15.   Cummings, J. L., Morstorf, T. & Zhong, K. Alzheimer's disease drug-development pipeline: few candidates, frequent failures. *Alzheimers Res. Ther.* **6**, 37 (2014).

16.   FDA-Approved Treatments for Alzheimer's. 5

17.   Kennedy, M. E. *et al.* The BACE1 inhibitor verubecestat (MK-8931) reduces CNS β-amyloid in animal models and in Alzheimers disease patients. *Sci. Transl. Med.* **8**, 363ra150-363ra150 (2016).

18.   Crump, C. J., Johnson, D. S. & Li, Y.-M. Development and Mechanism of γ-Secretase Modulators for Alzheimer's Disease. *Biochemistry* **52**, 3197–3216 (2013).

19.   Kounnas, M. Z., Lane-Donovan, C., Nowakowski, D. W., Herz, J. & Comer, W. T. NGP 555, a γ-secretase modulator, lowers the amyloid biomarker, Aβ42, in cerebrospinal fluid while preventing Alzheimer's disease cognitive decline in rodents. *Alzheimers Dement. Transl. Res. Clin. Interv.* **3**, 65–73 (2017).

20.   Gold, M. Phase II clinical trials of anti–amyloid β antibodies: When is enough, enough? *Alzheimers Dement. Transl. Res. Clin. Interv.* **3**, 402–409 (2017).

21.   Sevigny, J. *et al.* The antibody aducanumab reduces Aβ plaques in Alzheimer's disease. *Nature* **537**, 50–56 (2016).

22.   Egan, M. F. *et al.* Randomized Trial of Verubecestat for Mild-to-Moderate Alzheimer's Disease. *N. Engl. J. Med.* **378**, 1691–1703 (2018).

23.   van Dyck, C. H. Anti-Amyloid-β Monoclonal Antibodies for Alzheimer's Disease: Pitfalls and Promise. *Biol. Psychiatry* **83**, 311–319 (2018).

24.   Lu, J.-X. *et al.* Molecular Structure of β-Amyloid Fibrils in Alzheimer's Disease Brain Tissue. *Cell* **154**, 1257–1268 (2013).

25.   Bapineuzumab | ALZFORUM. Available at: https://www.alzforum.org/therapeutics/bapineuzumab.

26.   Solanezumab | ALZFORUM. Available at: https://www.alzforum.org/therapeutics/solanezumab.

27.   Gantenerumab | ALZFORUM. Available at: https://www.alzforum.org/therapeutics/gantenerumab.

28.   Crenezumab | ALZFORUM. Available at: https://www.alzforum.org/therapeutics/crenezumab.

29.   Ponezumab | ALZFORUM. Available at: https://www.alzforum.org/therapeutics/ponezumab.

30.   BAN2401 | ALZFORUM. Available at: https://www.alzforum.org/therapeutics/ban2401.

31.   Aducanumab | ALZFORUM. Available at: https://www.alzforum.org/therapeutics/aducanumab.

32.   C2N 8E12 | ALZFORUM. Available at: https://www.alzforum.org/therapeutics/c2n-8e12.

33.   BIIB076 | ALZFORUM. Available at: https://www.alzforum.org/therapeutics/biib076.

34.   ABBOTT, A. & DOLGIN, E. Leading Alzheimer's theory survives drug failure. 2

35.   Maruyama, M. *et al.* Imaging of Tau Pathology in a Tauopathy Mouse Model and in Alzheimer Patients Compared to Normal Controls. *Neuron* **79**, 1094–1108 (2013).

36.   Johnson, K. A., Fox, N. C., Sperling, R. A. & Klunk, W. E. Brain Imaging in Alzheimer Disease. *Cold Spring Harb. Perspect. Med.* **2**, a006213–a006213 (2012).

37.   Rowe, C. C. & Villemagne, V. L. Brain Amyloid Imaging. *J. Nucl. Med. Technol.* **41**, 11–18 (2013).

38.   Ossenkoppele, R. *et al.* Tau PET patterns mirror clinical and neuroanatomical variability in Alzheimer's disease. *Brain* **139**, 1551–1567 (2016).

39.   Johnson, K. A. *et al.* Tau positron emission tomographic imaging in aging and early Alzheimer disease: Tau PET in Aging and Early AD. *Ann. Neurol.* **79**, 110–119 (2016).

40.   Garber, K. First FDA-approved beta-amyloid diagnostic hits the market. *Nat. Biotechnol.* **30**, 575–575 (2012).

41.   Flutemetamol (^{18}F). *Wikipedia* (2018).

42.   Florbetaben (^{18}F). *Wikipedia* (2018).

43.   Hamley, I. W. The Amyloid Beta Peptide: A Chemist's Perspective. Role in Alzheimer's and Fibrillization. *Chem. Rev.* **112**, 5147–5192 (2012).

44.   Murphy, M. P. & LeVine, H. Alzheimer's Disease and the Amyloid-β Peptide. *J. Alzheimers Dis.* **19**, 311–323 (2010).

45.   Masters, C. L. & Selkoe, D. J. Biochemistry of Amyloid β-Protein and Amyloid Deposits in Alzheimer Disease. *Cold Spring Harb. Perspect. Med.* **2**, a006262–a006262 (2012).

46.   Pauwels, K. *et al.* Structural Basis for Increased Toxicity of Pathological $A\beta_{42}$: $A\beta_{40}$ Ratios in Alzheimer Disease. *J. Biol. Chem.* **287**, 5650–5660 (2012).

47.   Dumurgier, J. *et al.* Cerebrospinal fluid amyloid-β 42/40 ratio in clinical setting of memory centers: a multicentric study. *Alzheimers Res. Ther.* **7**, (2015).

48.   Fandos, N. *et al.* Plasma amyloid β 42/40 ratios as biomarkers for amyloid β cerebral deposition in cognitively normal individuals. *Alzheimers Dement. Diagn. Assess. Dis. Monit.* **8**, 179–187 (2017).

49.   Bitan, G. *et al.* Amyloid β-protein (Aβ) assembly: Aβ40 and Aβ42 oligomerize through distinct pathways. *Proc. Natl. Acad. Sci.* **100**, 330–335 (2003).

50.   Dobson, C. M. Protein folding and misfolding. **426**, 7 (2003).

51.   Kumar, S. & Walter, J. Phosphorylation of amyloid beta (Aβ) peptides – A trigger for formation of toxic aggregates in Alzheimer's disease. *Aging* **3**, 803–812 (2011).

52. Sabaté, R. & Estelrich, J. Evidence of the Existence of Micelles in the Fibrillogenesis of β-Amyloid Peptide. *J. Phys. Chem. B* **109**, 11027–11032 (2005).

53. Cohen, S. I. A. *et al.* Distinct thermodynamic signatures of oligomer generation in the aggregation of the amyloid-β peptide. *Nat. Chem.* **10**, 523–531 (2018).

54. Cohen, S. I. A. *et al.* Proliferation of amyloid-β 42 aggregates occurs through a secondary nucleation mechanism. *Proc. Natl. Acad. Sci.* **110**, 9758–9763 (2013).

55. Meisl, G. *et al.* Differences in nucleation behavior underlie the contrasting aggregation kinetics of the Aβ40 and Aβ42 peptides. *Proc. Natl. Acad. Sci.* **111**, 9384–9389 (2014).

56. Habchi, J. *et al.* Systematic development of small molecules to inhibit specific microscopic steps of Aβ42 aggregation in Alzheimer's disease. *Proc. Natl. Acad. Sci.* **114**, E200–E208 (2017).

57. Xue, C., Lin, T. Y., Chang, D. & Guo, Z. Thioflavin T as an amyloid dye: fibril quantification, optimal concentration and effect on aggregation. *R. Soc. Open Sci.* **4**, 160696 (2017).

58. Wolfe, L. S. *et al.* Protein-induced photophysical changes to the amyloid indicator dye thioflavin T. *Proc. Natl. Acad. Sci.* **107**, 16863–16868 (2010).

59. Ban, T., Hamada, D., Hasegawa, K., Naiki, H. & Goto, Y. Direct Observation of Amyloid Fibril Growth Monitored by Thioflavin T Fluorescence. *J. Biol. Chem.* **278**, 16462–16465 (2003).

60. Freire, S., de Araujo, M. H., Al-Soufi, W. & Novo, M. Photophysical study of Thioflavin T as fluorescence marker of amyloid fibrils. *Dyes Pigments* **110**, 97–105 (2014).

61. Kuznetsova, I. M., Sulatskaya, A. I., Uversky, V. N. & Turoverov, K. K. Analyzing Thioflavin T Binding to Amyloid Fibrils by an Equilibrium Microdialysis-Based Technique. *PLoS ONE* **7**, e30724 (2012).

62. Khurana, R. *et al.* Mechanism of thioflavin T binding to amyloid fibrils. *J. Struct. Biol.* **151**, 229–238 (2005).

63. Groenning, M. Binding mode of Thioflavin T and other molecular probes in the context of amyloid fibrils—current status. *J. Chem. Biol.* **3**, 1–18 (2010).

64. Biancalana, M. & Koide, S. Molecular mechanism of Thioflavin-T binding to amyloid fibrils. *Biochim. Biophys. Acta BBA - Proteins Proteomics* **1804**, 1405–1412 (2010).

65. Amdursky, N., Erez, Y. & Huppert, D. Molecular Rotors: What Lies Behind the High Sensitivity of the Thioflavin-T Fluorescent Marker. *Acc. Chem. Res.* **45**, 1548–1557 (2012).

66. Sulatskaya, A. I., Kuznetsova, I. M. & Turoverov, K. K. Interaction of Thioflavin T with Amyloid Fibrils: Stoichiometry and Affinity of Dye Binding, Absorption Spectra of Bound Dye. *J. Phys. Chem. B* **115**, 11519–11524 (2011).

67. Biancalana, M., Makabe, K., Koide, A. & Koide, S. Molecular Mechanism of Thioflavin-T Binding to the Surface of β-Rich Peptide Self-Assemblies. *J. Mol. Biol.* **385**, 1052–1063 (2009).

68. Wu, C., Biancalana, M., Koide, S. & Shea, J.-E. Binding Modes of Thioflavin-T to the Single-Layer β-Sheet of the Peptide Self-Assembly Mimics. *J. Mol. Biol.* **394**, 627–633 (2009).

69. Mathis, C. A. *et al.* A lipophilic thioflavin-T derivative for positron emission tomography (PET) imaging of amyloid in brain. *Bioorg. Med. Chem. Lett.* **12**, 295–298 (2002).

70. Klunk, W. E. *et al.* The Binding of 2-(4′-Methylaminophenyl)Benzothiazole to Postmortem Brain Homogenates Is Dominated by the Amyloid Component. *J. Neurosci.* **23**, 2086–2092 (2003).

71. Klunk, W. E. *et al.* Imaging brain amyloid in Alzheimer's disease with Pittsburgh Compound-B. *Ann. Neurol.* **55**, 306–319 (2004).

72. Mathis, C. A. *et al.* Synthesis and Evaluation of ^{11}C-Labeled 6-Substituted 2-Arylbenzothiazoles as Amyloid Imaging Agents. *J. Med. Chem.* **46**, 2740–2754 (2003).

73. Cohen, A. D. *et al.* Using Pittsburgh Compound B for In Vivo PET Imaging of Fibrillar Amyloid-Beta. in *Advances in Pharmacology* **64**, 27–81 (Elsevier, 2012).

74. Okello, A. *et al.* Conversion of amyloid positive and negative MCI to AD over 3 years: An ^{11}C-PIB PET study. *Neurology* **73**, 754–760 (2009).

75. Yamin, G. & Teplow, D. B. Pittsburgh Compound-B (PiB) binds amyloid β-protein protofibrils. *J. Neurochem.* **140**, 210–215 (2017).

76. Wu, C., Bowers, M. T. & Shea, J.-E. On the Origin of the Stronger Binding of PIB over Thioflavin T to Protofibrils of the Alzheimer Amyloid-β Peptide: A Molecular Dynamics Study. *Biophys. J.* **100**, 1316–1324 (2011).

77. Lockhart, A. *et al.* PIB is a non-specific imaging marker of amyloid-beta (Aβ) peptide-related cerebral amyloidosis. *Brain* **130**, 2607–2615 (2007).

78.   Ehrnhoefer, D. E. *et al.* EGCG redirects amyloidogenic polypeptides into unstructured, off-pathway oligomers. *Nat. Struct. Mol. Biol.* **15**, 558–566 (2008).

79.   Bieschke, J. *et al.* EGCG remodels mature α-synuclein and amyloid-β fibrils and reduces cellular toxicity. *Proc. Natl. Acad. Sci.* **107**, 7710–7715 (2010).

80.   Lopez del Amo, J. M. *et al.* Structural Properties of EGCG-Induced, Nontoxic Alzheimer's Disease Aβ Oligomers. *J. Mol. Biol.* **421**, 517–524 (2012).

81.   Cheng, P.-N., Liu, C., Zhao, M., Eisenberg, D. & Nowick, J. S. Amyloid β-sheet mimics that antagonize protein aggregation and reduce amyloid toxicity. *Nat. Chem.* **4**, 927–933 (2012).

82.   Sciarretta, K. L., Gordon, D. J. & Meredith, S. C. Peptide-Based Inhibitors of Amyloid Assembly. in *Methods in Enzymology* **413**, 273–312 (Elsevier, 2006).

83.   Sato, T. *et al.* Inhibitors of Amyloid Toxicity Based on β-sheet Packing of Aβ40 and Aβ42[†]. *Biochemistry* **45**, 5503–5516 (2006).

84.   Neddenriep, B. Short Peptides as Inhibitors of Amyloid Aggregation. *Open Biotechnol. J.* **5**, 39–46 (2011).

85.   Andreetto, E. *et al.* A Hot-Segment-Based Approach for the Design of Cross-Amyloid Interaction Surface Mimics as Inhibitors of Amyloid Self-Assembly. *Angew. Chem. Int. Ed.* **54**, 13095–13100 (2015).

86.   Kokkoni, N., Stott, K., Amijee, H., Mason, J. M. & Doig, A. J. *N*-Methylated Peptide Inhibitors of β-Amyloid Aggregation and Toxicity. Optimization of the Inhibitor Structure[†]. *Biochemistry* **45**, 9906–9918 (2006).

87.   Cho, P. Y., Joshi, G., Boersma, M. D., Johnson, J. A. & Murphy, R. M. A Cyclic Peptide Mimic of the β-Amyloid Binding Domain on Transthyretin. *ACS Chem. Neurosci.* **6**, 778–789 (2015).

88.   Craik, D. J., Fairlie, D. P., Liras, S. & Price, D. The Future of Peptide-based Drugs: Peptides in Drug Development. *Chem. Biol. Drug Des.* **81**, 136–147 (2013).

89.   Fosgerau, K. & Hoffmann, T. Peptide therapeutics: current status and future directions. *Drug Discov. Today* **20**, 122–128 (2015).

90.   Yan, L.-M., Tatarek-Nossol, M., Velkova, A., Kazantzis, A. & Kapurniotu, A. Design of a mimic of nonamyloidogenic and bioactive human islet amyloid polypeptide (IAPP) as nanomolar affinity inhibitor of IAPP cytotoxic fibrillogenesis. *Proc. Natl. Acad. Sci.* **103**, 2046–2051 (2006).

91.   Rezaei-Ghaleh, N., Andreetto, E., Yan, L.-M., Kapurniotu, A. & Zweckstetter, M. Interaction between Amyloid Beta Peptide and an Aggregation Blocker Peptide Mimicking Islet Amyloid Polypeptide. *PLoS ONE* **6**, e20289 (2011).

92.   Andreetto, E. *et al.* Identification of Hot Regions of the Aβ-IAPP Interaction Interface as High-Affinity Binding Sites in both Cross- and Self-Association. *Angew. Chem. Int. Ed.* **49**, 3081–3085 (2010).

93.   Kapurniotu, A., Schmauder, A. & Tenidis, K. Structure-based design and study of non-amyloidogenic, double *N*-methylated IAPP amyloid core sequences as inhibitors of IAPP amyloid formation and cytotoxicity. *J. Mol. Biol.* **315**, 339–350 (2002).

94.   Du, J., Cho, P. Y., Yang, D. T. & Murphy, R. M. Identification of beta-amyloid-binding sites on transthyretin. *Protein Eng. Des. Sel.* **25**, 337–345 (2012).

95.   Tycko, R. Molecular structure of amyloid fibrils: insights from solid-state NMR. *Q. Rev. Biophys.* **39**, 1 (2006).

96.   Tycko, R. Molecular Structure of Aggregated Amyloid-β: Insights from Solid-State Nuclear Magnetic Resonance. *Cold Spring Harb. Perspect. Med.* **6**, a024083 (2016).

97.   Solid-State NMR Spectroscopy Principles and Applications: Duer/Solid-State. (Blackwell Science Ltd, 2001). doi:10.1002/9780470999394

98.   Keeler, J. Understanding NMR Spectroscopy. (2016). doi:10.17863/CAM.968

99.   Hennel, J. W. & Klinowski, J. Magic-Angle Spinning: a Historical Perspective. in *New Techniques in Solid-State NMR* (ed. Klinowski, J.) **246**, 1–14 (Springer Berlin Heidelberg, 2005).

100.   Andrew, E. R., Bradbury, A. & Eades, R. G. Nuclear Magnetic Resonance Spectra from a Crystal rotated at High Speed. *Nature* **182**, 1659–1659 (1958).

101.   Lowe, I. J. Free Induction Decays of Rotating Solids. *Phys. Rev. Lett.* **2**, 285–287 (1959).

102.   Pines, A., Gibby, M. G. & Waugh, J. S. Proton-enhanced NMR of dilute spins in solids. *J. Chem. Phys.* **59**, 569–590 (1973).

103.   Schaefer, J. & Stejskal, E. O. Carbon-13 nuclear magnetic resonance of polymers spinning at the magic angle. *J. Am. Chem. Soc.* **98**, 1031–1032 (1976).

104.   Petkova, A. T. *et al.* A structural model for Alzheimer's β-amyloid fibrils based on experimental constraints from solid state NMR. *Proc. Natl. Acad. Sci.* **99**, 16742–16747 (2002).

105.   Igumenova, T. I., Wand, A. J. & McDermott, A. E. Assignment of the Backbone Resonances for Microcrystalline Ubiquitin. *J. Am. Chem. Soc.* **126**, 5323–5331 (2004).

106.   Franks, W. T. *et al.* Magic-Angle Spinning Solid-State NMR Spectroscopy of the β1 Immunoglobulin Binding Domain of Protein G (GB1): [15]N and [13]C Chemical Shift Assignments and Conformational Analysis. *J. Am. Chem. Soc.* **127**, 12291–12305 (2005).

107.   Pauli, J., Baldus, M., van Rossum, B., de Groot, H. & Oschkinat, H. Backbone and Side-Chain ^{13}C and [15]N Signal Assignments of the α-Spectrin SH3 Domain by Magic Angle Spinning Solid-State NMR at 17.6 Tesla. *ChemBioChem* **2**, 272–281 (2001).

108.   Tycko, R. On the problem of resonance assignments in solid state NMR of uniformly ^{15}N, ^{13}C-labeled proteins. *J. Magn. Reson.* **253**, 166–172 (2015).

109.   Linser, R. *et al.* Proton-Detected Solid-State NMR Spectroscopy of Fibrillar and Membrane Proteins. *Angew. Chem. Int. Ed.* **50**, 4508–4512 (2011).

110.   Zhou, D. H. *et al.* Proton-Detected Solid-State NMR Spectroscopy of Fully Protonated Proteins at 40 kHz Magic-Angle Spinning. *J. Am. Chem. Soc.* **129**, 11791–11801 (2007).

111.   Knight, M. J. *et al.* Fast Resonance Assignment and Fold Determination of Human Superoxide Dismutase by High-Resolution Proton-Detected Solid-State MAS NMR Spectroscopy. *Angew. Chem. Int. Ed.* **50**, 11697–11701 (2011).

112.   Chevelkov, V., Rehbein, K., Diehl, A. & Reif, B. Ultrahigh Resolution in Proton Solid-State NMR Spectroscopy at High Levels of Deuteration. *Angew. Chem. Int. Ed.* **45**, 3878–3881 (2006).

113.   Barbet-Massin, E. *et al.* Rapid Proton-Detected NMR Assignment for Proteins with Fast Magic Angle Spinning. *J. Am. Chem. Soc.* **136**, 12489–12497 (2014).

114.   Daebel, V. Introduction to Proton Detection in Biological Samples under Ultra-Fast Magic Angle Spinning. 6

115.   Chimon, S. & Ishii, Y. Capturing Intermediate Structures of Alzheimer's β-Amyloid, Aβ (1−40), by Solid-State NMR Spectroscopy. *J. Am. Chem. Soc.* **127**, 13472–13473 (2005).

116.   Chimon, S. *et al.* Evidence of fibril-like β-sheet structures in a neurotoxic amyloid intermediate of Alzheimer's β-amyloid. *Nat. Struct. Mol. Biol.* **14**, 1157–1164 (2007).

117.   Ahmed, M. *et al.* Structural conversion of neurotoxic amyloid-β 1–42 oligomers to fibrils. *Nat. Struct. Mol. Biol.* **17**, 561–567 (2010).

118.   Petkova, A. T., Yau, W.-M. & Tycko, R. Experimental Constraints on Quaternary Structure in Alzheimer's β-Amyloid Fibrils[†]. *Biochemistry* **45**, 498–512 (2006).

119.   Paravastu, A. K., Leapman, R. D., Yau, W.-M. & Tycko, R. Molecular structural basis for polymorphism in Alzheimer's β-amyloid fibrils. *Proc. Natl. Acad. Sci.* **105**, 18349–18354 (2008).

120.   Bertini, I., Gonnelli, L., Luchinat, C., Mao, J. & Nesi, A. A New Structural Model of Aβ$_{40}$ Fibrils. *J. Am. Chem. Soc.* **133**, 16013–16022 (2011).

121.   Niu, Z. *et al.* The Molecular Structure of Alzheimer β-Amyloid Fibrils Formed in the Presence of Phospholipid Vesicles. *Angew. Chem. Int. Ed.* **53**, 9294–9297 (2014).

122.   Colvin, M. T. *et al.* Atomic Resolution Structure of Monomorphic Aβ$_{42}$ Amyloid Fibrils. *J. Am. Chem. Soc.* **138**, 9663–9674 (2016).

123.   Wälti, M. A. *et al.* Atomic-resolution structure of a disease-relevant Aβ (1–42) amyloid fibril. *Proc. Natl. Acad. Sci.* **113**, E4976–E4984 (2016).

124.   Xiao, Y. *et al.* Aβ (1–42) fibril structure illuminates self-recognition and replication of amyloid in Alzheimer's disease. *Nat. Struct. Mol. Biol.* **22**, 499–505 (2015).

125.   Gremer, L. *et al.* Fibril structure of amyloid-β (1–42) by cryo–electron microscopy. *Science* **358**, 116–119 (2017).

126.   Lopez del Amo, J. M. *et al.* An Asymmetric Dimer as the Basic Subunit in Alzheimer's Disease Amyloid β Fibrils. *Angew. Chem. Int. Ed.* **51**, 6136–6139 (2012).

127.   Stevens, T. J. *et al.* A software framework for analysing solid-state MAS NMR data. *J. Biomol. NMR* **51**, 437–447 (2011).

128.   Vranken, W. F. *et al.* The CCPN data model for NMR spectroscopy: Development of a software pipeline. *Proteins Struct. Funct. Bioinforma.* **59**, 687–696 (2005).

129. Jerschow, A. & Müller, N. Suppression of Convection Artifacts in Stimulated-Echo Diffusion Experiments. Double-Stimulated-Echo Experiments. *J. Magn. Reson.* **125**, 372–375 (1997).

130. Jerschow, A. & Müller, N. Convection Compensation in Gradient Enhanced Nuclear Magnetic Resonance Spectroscopy. *J. Magn. Reson.* **132**, 13–18 (1998).

131. Ahuja, P., Sarkar, R., Vasos, P. R. & Bodenhausen, G. Diffusion Coefficients of Biomolecules Using Long-Lived Spin States. *J. Am. Chem. Soc.* **131**, 7498–7499 (2009).

132. Mayer, M. & Meyer, B. Characterization of Ligand Binding by Saturation Transfer Difference NMR Spectroscopy. *Angew. Chem. Int. Ed.* **38**, 1784–1788 (1999).

133. Mayer, M. & Meyer, B. Group Epitope Mapping by Saturation Transfer Difference NMR To Identify Segments of a Ligand in Direct Contact with a Protein Receptor. *J. Am. Chem. Soc.* **123**, 6108–6117 (2001).

134. Meyer, B. & Peters, T. NMR Spectroscopy Techniques for Screening and Identifying Ligand Binding to Protein Receptors. *Angew. Chem. Int. Ed.* **42**, 864–890 (2003).

135. Viegas, A., Manso, J., Nobrega, F. L. & Cabrita, E. J. Saturation-Transfer Difference (STD) NMR: A Simple and Fast Method for Ligand Screening and Characterization of Protein Binding. *J. Chem. Educ.* **88**, 990–994 (2011).

136. AG, L. I. Dynamic Light Scattering. Available at: https://lsinstruments.ch/en/technology/dynamic-light-scattering-dls.

137. Chatterjee, J., Gilon, C., Hoffman, A. & Kessler, H. *N*-Methylation of Peptides: A New Perspective in Medicinal Chemistry. *Acc. Chem. Res.* **41**, 1331–1342 (2008).

138. Chatterjee, J., Rechenmacher, F. & Kessler, H. *N*-Methylation of Peptides and Proteins: An Important Element for Modulating Biological Functions. *Angew. Chem. Int. Ed.* **52**, 254–269 (2013).

139. Vitoux, B., Aubry, A., Cung, M. T. & Marraud, M. *N*-Methyl peptides: VII. Conformational perturbations induced by *N*-methylation of model dipeptides. *Int. J. Pept. Protein Res.* **27**, 617–632 (2009).

140. Stewart, W. E. & Siddall, T. H. Nuclear magnetic resonance studies of amides. *Chem. Rev.* **70**, 517–551 (1970).

141. Platzer, G., Okon, M. & McIntosh, L. P. pH-dependent random coil ^{1}H, ^{13}C, and ^{15}N chemical shifts of the ionizable amino acids: a guide for protein pK a measurements. *J. Biomol. NMR* **60**, 109–129 (2014).

142. Spanopoulou, A. *et al.* Designed Macrocyclic Peptides as Nanomolar Amyloid Inhibitors Based on Minimal Recognition Elements. *Angew. Chem. Int. Ed.* **57**, 14503–14508 (2018).

143. Tycko, R. Physical and structural basis for polymorphism in amyloid fibrils: Amyloid Polymorphism. *Protein Sci.* **23**, 1528–1539 (2014).

144. Tycko, R. Amyloid Polymorphism: Structural Basis and Neurobiological Relevance. *Neuron* **86**, 632–645 (2015).

145. Elkins, M. R. *et al.* Structural Polymorphism of Alzheimer's β-Amyloid Fibrils as Controlled by an E22 Switch: A Solid-State NMR Study. *J. Am. Chem. Soc.* **138**, 9840–9852 (2016).

146. Fändrich, M. *et al.* Amyloid fibril polymorphism: a challenge for molecular imaging and therapy. *J. Intern. Med.* **283**, 218–237 (2018).

147. Qiang, W., Yau, W.-M., Lu, J.-X., Collinge, J. & Tycko, R. Structural variation in amyloid-β fibrils from Alzheimer's disease clinical subtypes. *Nature* **541**, 217–221 (2017).

148. Petkova, A. T. Self-Propagating, Molecular-Level Polymorphism in Alzheimer's β-Amyloid Fibrils. *Science* **307**, 262–265 (2005).

149. Chen, B., Thurber, K. R., Shewmaker, F., Wickner, R. B. & Tycko, R. Measurement of amyloid fibril mass-per-length by tilted-beam transmission electron microscopy. *Proc. Natl. Acad. Sci.* **106**, 14339–14344 (2009).

150. Paravastu, A. K., Petkova, A. T. & Tycko, R. Polymorphic Fibril Formation by Residues 10–40 of the Alzheimer's β-Amyloid Peptide. *Biophys. J.* **90**, 4618–4629 (2006).

151. Paravastu, A. K., Qahwash, I., Leapman, R. D., Meredith, S. C. & Tycko, R. Seeded growth of β-amyloid fibrils from Alzheimer's brain-derived fibrils produces a distinct fibril structure. *Proc. Natl. Acad. Sci.* **106**, 7443–7448 (2009).

152. Meinhardt, J., Sachse, C., Hortschansky, P., Grigorieff, N. & Fändrich, M. Aβ (1-40) Fibril Polymorphism Implies Diverse Interaction Patterns in Amyloid Fibrils. *J. Mol. Biol.* **386**, 869–877 (2009).

153. Kodali, R., Williams, A. D., Chemuru, S. & Wetzel, R. Aβ (1–40) Forms Five Distinct Amyloid Structures whose β-Sheet Contents and Fibril Stabilities Are Correlated. *J. Mol. Biol.* **401**, 503–517 (2010).

154. Walsh, D. M. *et al.* A facile method for expression and purification of the Alzheimer's disease-associated amyloid β-peptide: Expression and purification of the amyloid β-peptide. *FEBS J.* **276**, 1266–1281 (2009).

155. Meyer, B. & Peters, T. NMR Spectroscopy Techniques for Screening and Identifying Ligand Binding to Protein Receptors. *Angew. Chem. Int. Ed.* **42**, 864–890 (2003).

156. Fielding, L. NMR methods for the determination of protein–ligand dissociation constants. *Prog. Nucl. Magn. Reson. Spectrosc.* **51**, 219–242 (2007).

157. Williamson, M. P. Using chemical shift perturbation to characterise ligand binding. *Prog. Nucl. Magn. Reson. Spectrosc.* **73**, 1–16 (2013).

158. Shen, Y., Delaglio, F., Cornilescu, G. & Bax, A. TALOS+: a hybrid method for predicting protein backbone torsion angles from NMR chemical shifts. *J. Biomol. NMR* **44**, 213–223 (2009).

159. Prade, E. *et al.* Structural Mechanism of the Interaction of Alzheimer Disease Aβ Fibrils with the Non-steroidal Anti-inflammatory Drug (NSAID) Sulindac Sulfide. *J. Biol. Chem.* **290**, 28737–28745 (2015).

160. Xue, K. *et al.* Magic-Angle Spinning Frequencies beyond 300 kHz Are Necessary To Yield Maximum Sensitivity in Selectively Methyl Protonated Protein Samples in Solid-State NMR. *J. Phys. Chem. C* **122**, 16437–16442 (2018).

List of Publications

1. The Cross-Amyloid Interactions Surface Mimic R3-GI Exerts Their Inhibitory Effect by Undergoing Liquid-Liquid Phase Separation. (In preparation)
   Zheng Niu, Elke Prade, Eleni Malideli, Riddhiman Sarkar, Alexander Jussupow, Yonatan Mideksa, Ana Messias, Matthias Feige, Carlo Camilloni, Aphrodite Kapurniotu*, Bernd Reif*

2. Interactions between Amyloid Fibrils and PET Tracer Molecules. (In preparation)
   Zheng Niu, Riddhiman Sarkar, Behrooz H. Yousefi, Bernd Reif*

3. Interactions between Amyloid β Peptide and Lipid Membranes. (Review)
   Zheng Niu, Zhengfeng Zhang, Weijing Zhao, Jun Yang*
   Biochim. Biophys. Acta BBA-Biomembr. **2018**, *1860*, 1663-1669.